UNIVERSITY OF CALIFORNIA
SANTA CRUZ

PALEO-BIOGEOCHEMISTRY OF THE SUBPOLAR PACIFIC: HOW NUTRIENT SUPPLY RESPONDS TO CLIMATE CHANGE

A Dissertation submitted in partial satisfaction of the requirements
for the degree of

DOCTOR OF PHILOSOPHY

in

OCEAN SCIENCES

by

Kimberly Anne DeLong

September 2024

The Dissertation of Kimberly DeLong is approved:

_____
Professor Ana Christina Ravelo, Co-Chair

_____
Professor Matthew McCarthy, Co-Chair

_____
Professor Phoebe Lam

_____
Peter Biehl
Vice Provost and Dean of Graduate Studies

TABLE OF CONTENTS

LIST OF FIGURES

LIST OF TABLES

ACKNOWLEDGEMENTS

I would like to acknowledge and thank my advisor for her valuable guidance and support as the chair of my committee. I would also like to thank each of my committee members for their advice and advocacy throughout my time at UC Santa Cruz.

Chapter 1, in full, is a preprint of the material as it will likely appear in Geophysical Research Letters, where it is currently in review. K. A. deLong, T. Blackburn, B. Caissie, J. Addison, Z. Stroynowski, M. R. Sipala, F. Marcantonio, and A. C. Ravelo, Geophysical Research Letters, 2024. The dissertation author was the primary investigator and author of this paper.

Chapter 2, in part, is currently being prepared for submission for publication of the material with coauthors K. A. deLong, E. Pugsley, A. C. Ravelo, and M. McCarthy. The dissertation author was the primary researcher and author of this material.

Chapter 3 contains unpublished material coauthored with A. C. Ravelo. The dissertation author was the primary author of this chapter.

VITA

2012 Bachelor of Science in Environmental Geology, University of North Carolina Chapel Hill

2015 Master of Science in Oceanography, University of New Hampshire Durham

2024 Doctor of Philosophy in Ocean Sciences, University of California Santa Cruz

ABSTRACT OF THE DISSERTATION

Paleo-Biogeochemistry of the Subpolar Pacific:

How Nutrient Supply Responds to Climate Change

by

Kimberly DeLong

Climate dynamics are primarily forced by physical parameters such as insolation and ocean circulation; however, purely physical models fail to replicate the abrupt changes seen in climate records, implicating biogeochemical internal feedback mechanisms as important factors in the global climate system. Marine nutrient supply is a primary avenue that can potentially propagate climate signals to disparate parts of the globe; for example, a rapid response of the biological pump can both amplify signals and force further climate changes. Our current knowledge of paleo-biogeochemistry is limited by scant evidence and, often, low temporal resolution. This dissertation uses high-resolution marine sediments from the Subarctic and Subantarctic Pacific to reconstruct relationships between climate change, nutrient supply, and the biological pump.

The Subarctic Pacific experienced a brief interval of extremely high primary productivity during the global transition from the glacial to the interglacial climate regimes. The cause of this high productivity has been debated, with both iron fertilization and reorganizations in Pacific circulation proposed: iron fertilization would suggest a strengthened biological pump, while circulation changes may

indicate a weakened biological pump. Here, I reconstruct the diatom community response in terms of silicic acid utilization (single-genus silicon isotopes) and species composition, finding that silicic acid utilization was not enhanced, and that low-iron-adapted species were the primary responders to the high-productivity. These results suggest iron was the limiting nutrient during the high-productivity interval, consistent with the major reorganizations in Pacific circulation causing increased macronutrient supply and briefly releasing large amounts of CO_2 to the atmosphere.

Nutrient supply during the deglaciation is further explored via amino-acid-bound nitrogen isotopes from the same sediments from the Subarctic Pacific. This investigation finds that the high-productivity intervals carry an elevated signal of source $\delta^{15}N$ (i.e., the $\delta^{15}N$ of primary producers), corroborating a change in circulation. We also find high-productivity intervals have the lowest community Trophic Positions, indicative of shorter and more direct trophic chains, consistent with high macronutrient supply.

Finally, I examine changes in sediment color in the Subantarctic Pacific across the glacial-interglacial transitions of marine isotope stages 7/8 and 17/18 and find that sediment color is strongly related to sediment composition. Interglacial intervals contain high weight percent calcium carbonate and glacial periods contain high weight percent nitrogen. This suggests the position of the Subantarctic Front was strongly linked to changes in climate, with cold periods characterized by northward expansion of high-silicate waters, favoring diatom production over coccolithophores, and strengthening the local biological pump.

Chapter 1 BOLLING-ALLEROD PRODUCTIVITY IN THE SUBARCTIC PACIFIC DRIVEN BY SEASONAL UPWELLING

1 Introduction

The partitioning of carbon between the ocean and atmosphere is mediated by the ocean's chemistry, physical circulation, and biological processes. Phytoplankton productivity influences CO_2 exchange by removing carbon from the surface ocean via the biological pump, strongly linking the carbon cycle to nutrient supply including nitrogen, silicic acid and iron (Buesseler, 1998). Lower atmospheric CO_2 during the Last Glacial Maximum (LGM) is generally explained by strong stratification of the deep ocean and more complete utilization of nutrients in the Southern Ocean, forced by winds and iron supply (Ai et al., 2020; Martínez-García et al., 2014; Daniel M. Sigman et al., 2021; Toggweiler, 2009). The termination of this glacial regime was caused in part by the release of marine-sequestered CO_2 to the atmosphere, contributing to deglacial warming (Bauska et al., 2016). Changes in the Southern Ocean, the only region in the modern ocean where abyssal waters directly ventilate to the surface, can account for certain intervals of CO_2 release to the atmosphere (17.6-15.5 ka and 13.0-11.5 ka), but additional CO_2 releases occur at 14.8 ka and 11.7 ka from unknown marine sources (Anderson et al., 2009; Bauska et al., 2016). It is possible the Subarctic Pacific, including its marginal seas such as the Bering Sea, played a similar role to the Southern Ocean during abrupt deglacial events, releasing sequestered marine CO_2 via enhanced vertical exchange between deep waters and the surface ocean (Du et al., 2018; Galbraith et al., 2007).

Three deglacial high-productivity events, occurring during the Bølling (14.6-14.2 ka), Allerød (13.9-12.9 ka), and PreBoreal (11.7-10.3 ka), are marked by the synchronous deposition of opal across the Subarctic Pacific (Kuehn et al., 2014). These events may be akin to Southern Ocean opal-deposition events, which are interpreted as evidence for deep water upwelling and enhanced release of marine CO_2 (Anderson et al., 2009; Horn et al., 2011; Toggweiler, 2009). Marine CO_2 release can be enhanced by winter wind mixing homogenizing the upper water column, outcropping of deep waters where a large amount of carbon is stored, and a rate of total CO_2 (TCO_2) supply that outcompetes the rate of carbon drawdown by phytoplankton export (i.e. a weak biological pump). It is plausible these mechanisms occurred in the Subarctic Pacific during the deglaciation: stronger Westerly Winds are hypothesized to have occurred during glacial boundary conditions and may have persisted through much of the deglaciation, creating stronger Ekman suction and deeper winter wind mixing (Gray et al., 2018). Furthermore, a foraminifera-bound boron isotope reconstruction shows surface pH decreased in the open Subarctic North Pacific (SNP) during the times of highest productivity, suggesting the regional biological pump was weak despite the high productivity (Gray et al., 2018).

These high-productivity events in the SNP have not been widely accepted to represent periods with a weak biological pump. Instead, a range of potential explanations for the increased productivity, including iron fertilization and "transient stratification," frame the Bølling-Allerød (B-A) productivity as a C-sequestration event, making use of pre-existing underutilized nutrients (Du et al., 2022; Lam et al.,

2013; Praetorius et al., 2015). This may be because vertical exchange between surface and deep waters can be moderated by sea ice presence and strongly stratified intermediate water, requiring additional changes in physical circulation in order for deep waters to outcrop at the surface (Gray et al., 2018; Max et al., 2014; Sarnthein et al., 2004). Recent work has found increasing evidence for extreme reorganizations in physical circulation, providing a long-sought for mechanism to explain decades of puzzling findings, which could not be discerned from a single proxy in this complex region (Keigwin, 1998; Rafter et al., 2022; Walczak et al., 2020). The use of nitrogen isotopes to track utilization, for example, is hampered by the influence of water-column denitrification in the region (Brunelle et al., 2007). Furthermore, nutrient isotopes (Si, N) can indicate utilization changes, but cannot distinguish between nutrient limitation stemming from water geochemistry versus physical stratification of the water column, and thus should be interpreted in conjunction with proxies for physical dynamics.

Here, we take a new approach to determine the degree of vertical exchange that occurred in the SNP by quantifying the supply of silicic acid to the surface ocean at IODP Site U1340 in the Bering Sea (53°24N, 179°31W, 1295 m, **Figure 1d**). The supply of silicic acid and TCO_2 to the surface ocean are closely linked via their vertical concentrations, which arise from the biological pump, i.e., biological uptake at the surface and remineralization at depth as biogenic particles sink and dissolve in deeper waters (**Figure 1**). This signal is amplified in TCO_2 in the SNP, because deep waters carry respiration products accumulated from global overturning circulation. In

contrast, Si concentrations primarily reflect Si export from the overlying water column, because opal tends to sink faster and remineralize deeper than organic carbon. This creates a nonlinear relationship between TCO_2 and Si concentrations (**Figure 1**), which likely varied through time. To a first-order, however, the supply of silicic acid to surface phytoplankton reflects the degree of vertical exchange in the region and acts as a tracer for TCO_2. We quantify changes in silicic acid supply by measuring biogenic opal flux in combination with Si isotopes of *Coscinodiscus* frustules, a genus of diatom, which record the relative utilization of silicic acid (e.g., Horn et al., 2011). Our newly generated $\delta^{30}Si_{Coscinodiscus}$ record suggests the B-A was characterized by high Si availability despite high Si use and burial. Diatom indicators show a coincident shift from a stratified water column to seasonal upwelling dynamics and summer iron limitation. We therefore propose the high-productivity events were intervals of enhanced vertical mixing and excess macronutrient supply, with the regional biological pump limited by iron. This supports the hypothesis that the deglacial productivity events are the manifestation of major circulation changes that injected old, nutrient-rich, CO_2-rich waters into the surface Subarctic Pacific and released CO_2 to the atmosphere (Galbraith et al., 2007; Gray et al., 2018).

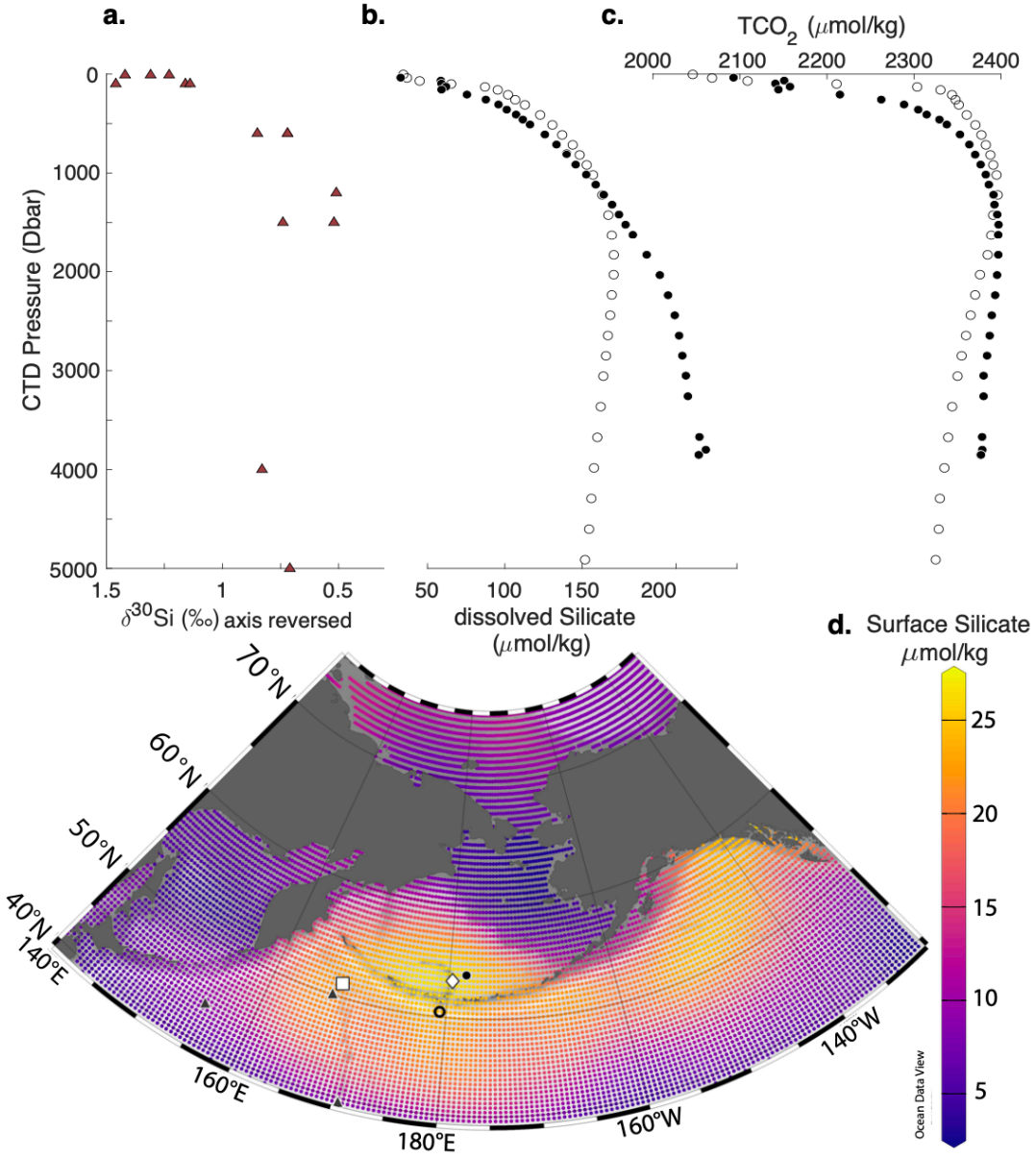

Figure 1.1: Profiles and surface concentrations of silica and carbon in the modern ocean, and a map of the region showing the location of relevant sites and stations; high concentrations of surface silicate indicate an HNLC region. (a) $\delta^{30}Si$ (‰) from the SNP (hydrocast locations are triangles on the map) (Reynolds, 2009). (b) Dissolved silicate and (c) TCO_2 concentrations (μmol/kg) from two nearby hydrocasts; black circles are from the Bering Sea and open circles are from the open SNP (Roden, 1995). (d) Map of the subarctic Pacific with near-surface silicic acid concentrations (Gouretski & Koltermann, 2004); gray shading shows seafloor bathymetry. Site U1340 is marked by a white diamond and site MD01-2416 is marked by a white square.

2 Methods

We created a new age model for U1340 (Text S1) using previously published radiocarbon data and the presence of regionally synchronous laminated intervals. Biogenic opal was measured in the US Geological Survey Pacific Ocean Paleoclimate Lab following the modified procedure of (Mortlock & Froelich, 1989), digesting 7.5 mg of sample in sodium carbonate (Figure S3). Uranium-Thorium analysis was conducted via isotope dilution analysis in the Marcantonio lab at Texas A&M University. 0.3-0.4 g of sediment were spiked with ^{229}Th and ^{236}U, acid digested, separated and purified via anion exchange chromatography as outlined in Loveley et al. (2017), and measured on an Element XR magnetic sector ICPMS (Fleisher & Anderson, 2003). Diatom slides were made at the Instituto Português do Mar e da Amosfera using the M2 cleaning and slide preparation methods described in Abrantes et al. (2005), treated in glass jars with no centrifugation. Species were counted via visual identification of >300 specimens when possible at 1050x. Diatom silicon isotope values were generated in the Keck Laboratory at the University of California, Santa Cruz using the following methods. Freeze-dried samples were washed on a 63μm sieve to remove clays and dried in a 55ºC oven. Samples were then cleaned with the M2 method, without the Calgon step, in non-glass containers and again oven-dried. To isolate a single diatom genus, samples were dry-sieved and ice rafted debris, radiolarians, spicules, and other genera were removed from the 63-125 μm portion by picking under a microscope and visually confirmed to be >99% *Coscinodiscus* specimens. *Coscinodiscus* species present were >95% *Coscinodiscus*

marginatus with occasional *Coscinodiscus oculus-iridis* and *Coscinodiscus radiatus*. To dissolve samples, ≤0.002 g was transferred to 100 µL of 10 M NaOH in screw-top Teflon vials and reacted in Parr vessels at 200°C for three days. Samples were transferred to BioRad 50W X8 cation exchange columns previously cleaned with HCl and Milli-Q water (after Georg et al., 2006), and eluted in Milli-Q water. Intensities of ^{28}Si, ^{29}Si and ^{30}Si were measured using standard-sample bracketing on a Neptune MC ICP-MS at high resolution equipped with an Apex Omega desolvating nebulizer. All values are reported vs. NBS 28. Expanded methods are in Text S2.

3 Interpretive Framework: $\delta^{30}Si$ and Diatom Indicators

Diatoms, single-celled algae that build siliceous (opal) frustules, preferentially uptake ^{28}Si, fractionating diatom $\delta^{30}Si$ ($\delta^{30}Si_{diatom}$) from seawater $\delta^{30}Si$ ($\delta^{30}Si_{sw}$) by a fractionation factor (ε). Surface $\delta^{30}Si_{sw}$ values are thus higher than subsurface waters, where remineralization occurs (**Figure 1a**) (Reynolds, 2009; Reynolds et al., 2006). If the initial signature of supplied silicic acid is known ($\delta^{30}Si_{initial}$), utilization can be calculated from $\delta^{30}Si_{diatom}$. We use an open-system model because *Coscinodiscus* is a deep-dwelling fall-bloom genus, and modern observations suggest fall blooms are fueled by nutricline entrainment, creating Si availability outside of summer near-surface Raleigh fraction (Giesbrecht et al., 2022; Reynolds et al., 2006), and use a typical ε of -1.1‰ (de la Rocha et al., 1997) because ε has not been measured in *Coscinodiscus*. In this model, the fraction of silicic acid used, termed utilization (*f*), = $1 - ((\delta^{30}Si_{initial} - \delta^{30}Si_{diatom})/\varepsilon)$ (e.g., Farmer et al., 2021 and refs therein; Text S4). Utilization is also a ratio between uptake and supply. Relative changes in Si supply

can be therefore be quantified by dividing an uptake estimate (here, we use opal flux) by utilization (Horn et al. 2011). Utilization and uptake values are first normalized to their respective LGM (19.4 ka) value, defining the LGM supply as 1.

Modern $\delta^{30}Si_{initial}$ has not been measured at our site but waters are a mix between Bering Shelf Winter Water (δ^{30}Si 1.94-2.12‰, Giesbrecht et al., 2022) and SNP waters (δ^{30}Si 1.16-1.23‰, Reynolds et al., 2006). This is consistent with the North Pacific value of 1.70‰ from a global model (Pichevin et al., 2020), which predicts a higher $\delta^{30}Si_{initial}$ of 1.87‰ during the LGM. Assuming a constant $\delta^{30}Si_{initial}$ of 1.70‰, our record suggests Si supply peaked in the late Bølling at ~11.5x the LGM, with Holocene supply ~4x the LGM (**cyan line, Figure 2e**). However, it is more likely that $\delta^{30}Si_{initial}$ varied through time as silicic acid was sourced from different pools. To test the robustness of the supply record, we calculated 1000 iterations of Si utilization using a randomly selected $\delta^{30}Si_{initial}$ from a range of deglacial δ^{30}Si values (1.16‰ - 2.04‰) from the Gulf of Alaska (Maier et al., 2015) (total range, 90%, and 95% percentile intervals in gray, **Figure 2e**).

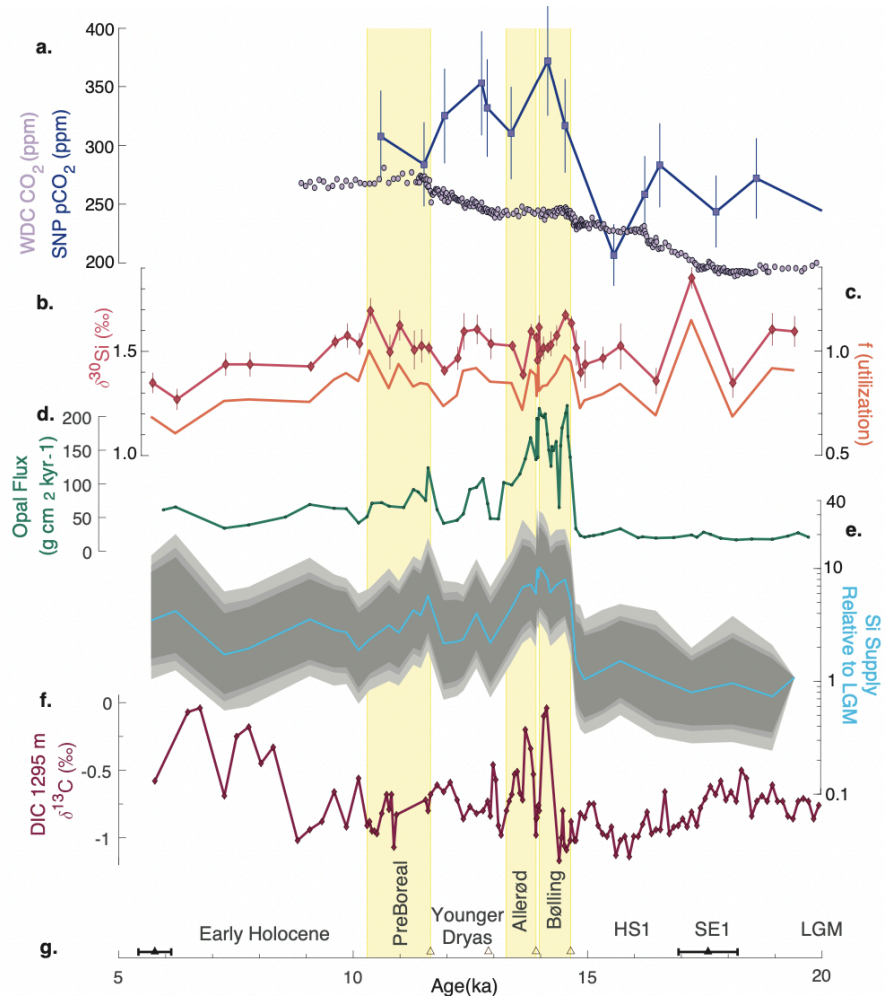

Figure 1.2: Silica and carbon dynamics across the deglaciation. (a) Atmospheric CO_2 concentration from the West Antarctic Ice Sheet Divide ice core (WDC) (ppm), lavender, (Marcott et al., 2014) overlain with a subarctic Pacific estimate of pCO_2 of surface waters from site MD01-2416 (ppm), dark blue (Gray et al., 2018). (b) Measured $\delta^{30}Si_{Coscinodiscus}$ values (‰ vs. NBS 28) reflect the utilization of silicic acid. (c) Silicic acid utilization, known as f, calculated assuming a fixed initial value. (d) Opal flux ($g \cdot cm^{-2} \cdot kyr^{-2}$), a measure of primary productivity, shows the highest productivity occurs in the early Bølling and Older Dryas (Calculated with ^{230}Th-derived mass accumulation rate; see SI Section 2). (e) Calculated Si supply assuming a fixed initial value (cyan) and a Monte Carlo simulation of 1000 possibilities with varying initial values (faint gray envelope shows the full range, light gray envelope shows the 95% percentile interval and dark gray envelope shows the 90% percentile interval). (f) *Uvigerina*-derived $\delta^{13}C$ of dissolved inorganic carbon (DIC) at 1295 m; negative values are characteristic of aged waters and near-zero values are characteristic of surface waters. (g) Age tie points shown with black triangles at radiocarbon-based ages and empty brown triangles at sedimentology-based ages. Yellow bars show the occurrence of laminated sediments at U1340.

Several diatom groups indicate environmental conditions in this region (**Text S5**). We newly interpret *Neodenticula seminae* to be an indicator of iron-limited, high-nutrient low-chlorophyll (HNLC) conditions with episodic iron fertilization, due to its abundance in low-iron waters and ability to rapidly take advantage of brief iron fertilization events (Marchetti et al., 2006; Yoshida et al., 2020, 2023). *N. seminae* abundances at our site roughly correspond to the bulk sediment Si:N ratios, another proxy for iron limitation; iron-limited communities have high Si:N ratios likely because thickly-silicified frustules deter predation while awaiting unpredictable iron-deposition events (Fig S4; **Text S5.1**; Assmy et al., 2013; Pichevin et al., 2014). The near-coretop assemblages (5-8 ka) are ~50% *N. seminae*, accurately representing modern HNLC conditions where it dominates summer production (Onodera & Takahashi, 2009; Sancetta & Robinson, 1983) (**Figure 3a)**.

Stratification indicators include Deep Chlorophyll Maximum flora (DCM; *Rhizosolenia, Thalassiothrix,* and *Coscinodiscus* species), which have a competitive advantage in highly nutrient-stratified systems and indicate a late-season nutricline (Worne et al., 2021). DCM flora comprise ~20% of the near-coretop assemblages, reflecting the modern fall bloom. Spring stratification is indicated by *Actinocyclus* species, primarily *Actinocyclus curvatulus*, which grows in thin, stable, low-nutrient surface layers, particularly those caused by distal ice melt (**Figure 3b;** Worne et al., 2021).

Chaetoceros spp, primarily resting spores, indicate upwelling events; this genus "blooms-and-busts" during high-nutrient conditions (including high-iron

conditions) such as a spring bloom or sea-ice-edge upwelling (Abrantes, 1988; Flynn et al., 2023; Tréguer et al., 2018).

Finally, several diatoms indicate sea-ice dynamics: *Thalassiosira antarctica* indicates thick sea-ice (Caissie et al., 2010). Another group characteristic of sea-ice margins blooms during spring ice melt (*Thalassiosira gravida, Thalassiosira hyalina, Thalassiosira nordenskioeldii; Stellarima; Odontella*) (Andersen et al., 2004; Barron et al., 2009; Stroynowski et al., 2017). *Fragilariopsis cylindrus* grows in 0°C-surface temperatures, including ice melt and polynyas (von Quillfeldt, 2004); if present at ~15% of the species composition, as at 14.8 ka, it indicates 1-4 months of sea ice per year (Caissie et al., 2010).

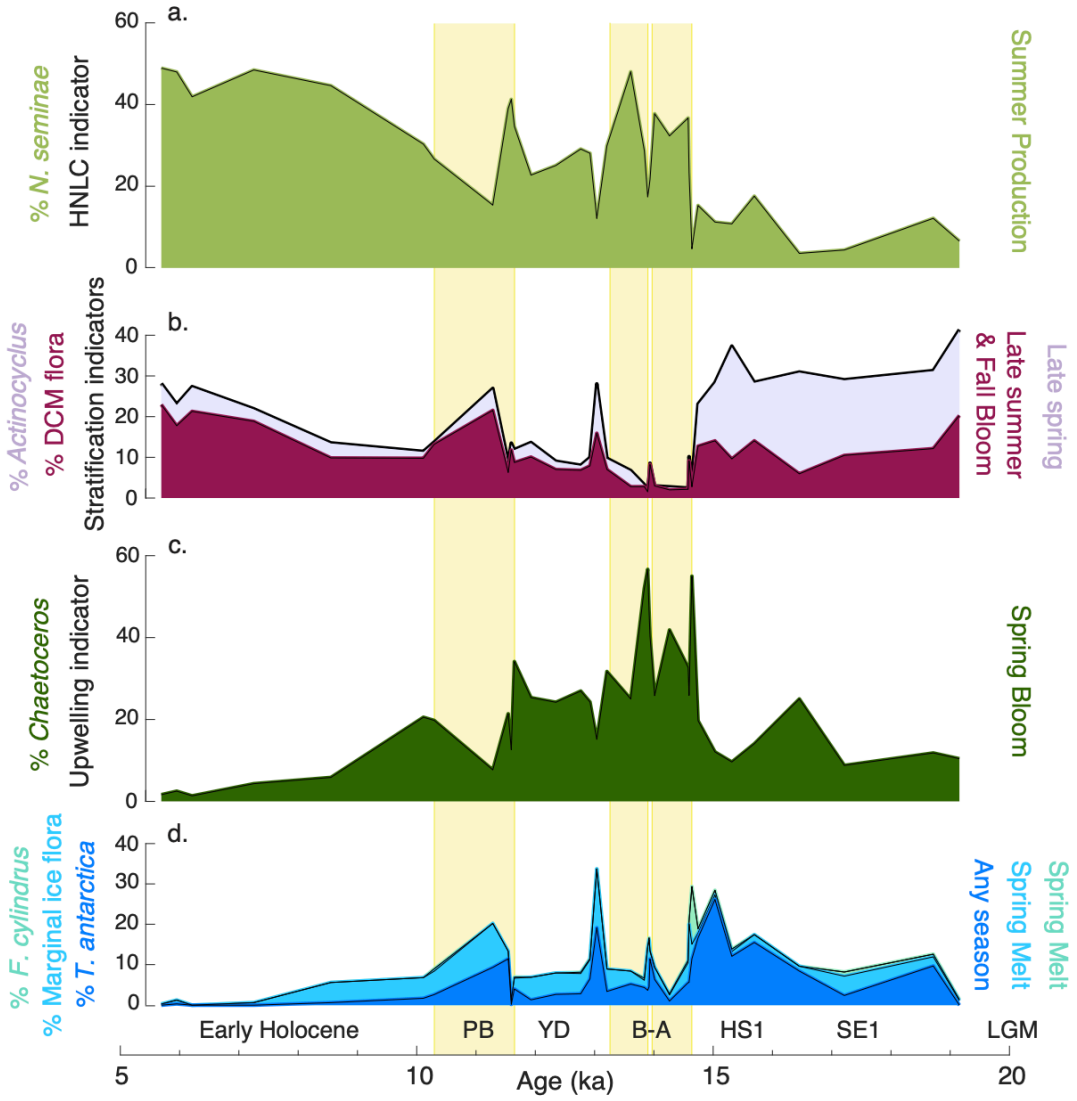

Figure 1.3: Relative percent abundances of diatom environmental indicators show that most of the high productivity of the Bølling-Allerød (B-A) was from upwelling and HNLC indicators. The seasonality of each group is also noted. Laminated sedimentary intervals are marked with yellow bars. (a) HNLC indicator *Neodenticula seminae* (%). (b) Stratification indicators, with stacked abundances: *Actinocyclus* spp, lavender, indicating low-nutrient surface layers (%), and Deep Chlorophyll Maximum (DCM) flora, burgundy, indicating a strong nutricline (%). (c) Upwelling indicator *Chaetocerous* spp (%). (d) Sea ice indicators with stacked abundances: marginal ice flora, light blue, indicating sea ice edge communities (%), *Thalassiosira antarctica,* dark blue, indicating thick sea ice, and *Fragilariopsis cylindrus,* pale green, indicating 0 °C waters. Named time intervals are shown, including the abbreviations LGM (Last Glacial Maximum), SE1 (Siku Event 1), HS1 (Heinrich Stadial 1), B-A (Bølling-Allerød), YD (Younger Dryas), PB (PreBoreal), and the Early Holocene.

4 Nutrient Supply in the Deglaciation

During the LGM and early deglaciation, we find low opal productivity and low Si supply (**Figure 2**), and diatom assemblages indicate both spring and fall stratification, suggesting a low-nutrient surface layer characterized much of the growing season (**Figure 3**). These findings are consistent with established regional dynamics: during the LGM, deep Pacific waters (>2000 m) were isolated from overlying intermediate waters (Rafter et al., 2022 and references therein), which in the SNP were filled with an expanded "Glacial" North Pacific Intermediate Water (GNPIW) that likely formed in the Bering Sea (Kender et al., 2018; Knudson & Ravelo, 2015; Max et al., 2014; Okazaki et al., 2010; You, 2003). Upwelling near our site would have tapped newly-formed GNPIW, which, having recently been surface water, would be low in nutrients (Kender et al., 2019). Coastal areas and marginal seas were also seasonally covered by sea ice, inhibiting winter mixing (Detlef et al., 2020; Takahashi et al., 2009), and stratification in the open SNP was enhanced, possibly inducing nitrogen limitation (H. Ren et al., 2015). Low light availability from sea-ice cover, low incident insolation, or wind mixing below the critical depth may have further limited productivity. In any case, the isolation of deep waters, presence of GNPIW, and extensive sea ice explain the low Si supply at the LGM (**Figure 4**).

During the early deglaciation from 14.8-19.4 ka, our $\delta^{30}Si_{\textit{Coscinodiscus}}$ record suggests large changes in utilization (or $\delta^{30}Si_{initial}$) occurred, possibly linked to regional changes in surface and intermediate circulation related to sea ice extent, Siku

Event 1, or other flooding events (Praetorius et al., 2020; Walczak et al., 2020). These utilization changes had seemingly little effect on opal productivity (**Figure 2**), which indicates silica was not the primary limiting factor. Iron delivery from dust was higher during the LGM and most of the deglaciation (Lam et al., 2013; Serno et al., 2015), which may have lowered Si:N utilization, perhaps circumventing silica limitation by more strongly diminishing N supply. The glacial circulation described above would have stripped both silica and nitrogen out of surface and intermediate waters; this would make regional surface $\delta^{30}Si_{initial}$ higher at the LGM (Pichevin et al., 2020). In our record, the $\delta^{30}Si_{\textit{Coscinodiscus}}$ value at 19.4 ka is 1.60‰; higher than Holocene values but lower than the highest deglacial values (here, 1.86‰ at ~17.2 ka; in the Gulf of Alaska, 2.0‰ at ~16 ka, Maier et al., 2015; Fig S2). These singular high $\delta^{30}Si_{\textit{Coscinodiscus}}$ values may be related to higher silicic acid utilization from brief stratification events (Maier et al., 2018).

Diatom sea-ice indicators increase during Heinrich Stadial 1 (HS1, 17.5 – 14.8 ka), (**Figure 3d**), agreeing with a detailed investigation further north in the Bering Sea which found sea ice growth during HS1 followed by rapid sea ice retreat at the transition to the B-A (Detlef et al., 2020). Sea ice extent at this latitude responds to winter storm intensity: ice growth is favored when the Aleutian Low is weak or shifted south of the Bering Sea, which may have occurred during HS1 due to global atmospheric shifts (e.g., displacement of the Intertropical Convergence Zone or weakening of the East Asian Monsoon, Maier et al., 2018). Sea ice retreat is

attributed to locally intense winter wind mixing over the Bering Sea, eroding near-surface stratification and preventing sea-ice formation (Detlef et al., 2020).

Opal flux increases eight-fold at the onset of the Bølling (14.8 ka), while only a moderate change in $\delta^{30}Si_{Coscinodiscus}$ occurs (0.28‰ ± 0.14‰), suggesting the primary reason productivity increased was not increased utilization but increased supply (shown by the large step increase in the calculated Si Supply, **Figure 2d**). Increased Si supply could be supplied by wind-driven vertical mixing such as curl-induced Ekman suction and the intensity of winter winds (Gray et al., 2020). The abundance of *Chaetoceros* indicates increased upwelling particularly at the onsets of the laminated intervals (**Figure 3c**) (Abrantes, 1988). Sea ice diatoms switch from thick-ice to marginal-ice indicators, suggesting an earlier spring melt (Worne et al., 2021), and disappearance of *Actinocyclus* suggests a lack of stable meltwater layers, both consistent with stronger wind mixing in early spring (**Figure 3**). Winter wind mixing and Ekman suction would synergistically increase nutrient supply to the surface subarctic Pacific. However, these mechanisms may not have been sufficient to increase Si supply if low-nutrient GNPIW was the only source.
Contemporaneously, GNPIW formation was suspended during the B-A, related to the cessation of sea ice formation; in the absence of GNPIW, aged Pacific deep water shoaled to fill intermediate depths (Detlef et al., 2020; Gray et al., 2018; Max et al., 2014). The benthic $\delta^{13}C$ of dissolved inorganic carbon ($\delta^{13}C_{DIC}$) at U1340 (1295 m), measured on *Uvigerina peregrina* and calibrated to water column DIC values (Cook et al., 2016; Schlung et al., 2013), shows this transition (**Figure 2f**). The $\delta^{13}C_{DIC}$

decreases to its lowest value in the early Bølling (-1.17‰) indicating increased presence of aged waters. This is evidence that deep waters (>2000 m before the B-A) shoaled above 1295 m. As aged deep waters shoaled, wind-driven vertical mixing could tap a new source of nutrients and introduce them to the surface community, instigating the B-A high productivity.

It is unclear, however, if vertical exchange between Deep Pacific Waters and the surface occurred continuously throughout the B-A or if water column overturn may have occurred as a brief instigating event. Step increases in Si supply and increased relative abundance of upwelling indicators repeat at the onsets of the Bølling, Allerød and PreBoreal, suggesting instigating triggers re-occurred each time (**Figures 1 and 2**). The Si supply record shows continuous high abundance of dissolved Si throughout the B-A (12.9-14.7 ka), with a late-Bølling peak driven by low $\delta^{30}Si_{\textit{Coscinodiscus}}$ during the highest productivity (**Figure 2c**). This indicates either high Si supply from continuous deep water outcropping, excess Si from iron limitation (HNLC conditions), low $\delta^{30}Si_{initial}$ values partially obscuring the utilization signal, or a combination of the three.

Remineralized silica from aged waters would carry a low $\delta^{30}Si_{initial}$ signature, while lateral advection from subtropical waters would carry a higher $\delta^{30}Si_{initial}$ (Pichevin et al., 2020; Reynolds, 2009). Incorporating a large uncertainty in the $\delta^{30}Si_{initial}$ value widens the possible values of Si supply, indicated by the grey shading in **Figure 2e.** All scenarios point to excess underutilized Si, and the late-Bølling peak in supply remains a robust feature, ranging from 3.5 to 36 times the LGM value. The

maximum extreme (36x the LGM) is created by an unlikely combination of inputs: complete utilization at the LGM paired with a shift to a higher $\delta^{30}Si_{initial}$ signature during the B-A. The minimum extreme (3.5x the LGM) represents a scenario with heavier-than-modern $\delta^{30}Si_{initial}$ and incomplete utilization in the LGM paired with a shift to lower $\delta^{30}Si_{initial}$ and more complete utilization during the B-A. Alternatively, high Si supply with a low $\delta^{30}Si_{initial}$ may have been partially sourced from terrestrial (riverine) inputs. Glacial runoff can have low $\delta^{30}Si$ signatures (-0.25‰, vs. 1.25‰ in nonglacial rivers) (Hawkings et al., 2018) and rapid meltwater events may have increased riverine Si inputs. The $\delta^{30}Si$-derived records cannot distinguish between Si supply from upwelling vs. riverine inputs and we therefore rely on diatom indicators and carbon isotopes to describe the physical oceanographic setting.

During the B-A, subarctic Pacific circulation was similar to modern circulation but with stronger winds (Gray et al., 2018), a lack of internal haloclines from Bering Shelf Winter Water, GNPIW, or NPIW (Detlef et al., 2020; Sarnthein et al., 2004), and a saltier sea surface (Du et al., 2018); this resulted in improved vertical exchange (**Figure 4**) and plausible deep-water outcropping in winter. At our site, *Chaetoceros* and *N. seminae* are both abundant (**Figure 3**), indicating macronutrient supply supported multiple species successions throughout the growing season (Caissie et al., 2010). Large spring blooms suggest seasonal dynamics with abundant spring nutrients and suppressed spring grazing, implying widespread winter mixing (Flynn et al., 2023; Sverdrup, 1953). Deep mixing across a wide region is also indicated by benthic-planktic ^{14}C offsets, which decrease from >1000 to <400 years at

our site and in the SNP during the deglaciation (Gebhardt et al., 2008; Schlung et al., 2013, **Table S2**). Gulf of Alaska ^{14}C records also indicate strong ventilation at intermediate depths during the B-A; however, it was not the location of direct deep water outcropping because the surface remained stratified (Praetorius et al., 2020). At our site, $\delta^{13}C_{DIC}$ appears to capture direct ventilation, with near-0‰ values at 14.1 ka implying 1295-m depth waters were recently sourced from surface waters (**Figure 2f;** Schlung et al., 2013). While this observation is based on only a few data points which may be affected by behavior or vital effects of *U. peregrina,* this timing corresponds to the "flip" in circulation recorded in ^{14}C and $\delta^{13}C$ throughout the Pacific (Rafter et al., 2022).

Dominant *N. seminae* and high bulk-sediment Si:N suggest iron limitation occurred at our site throughout the B-A and early PreBoreal. Although iron supply was higher than modern conditions due to elevated dust delivery and possibly dissolved iron from flooding continental shelves (Davies et al., 2011; Lam et al., 2013; Serno et al., 2015), the rate of iron supply did not keep pace with a larger increase in macronutrient supply (Maier et al., 2015). We propose the introduction of new macronutrients instead both fueled high productivity and intensified iron limitation, causing high Si use and burial relative to organic carbon (Assmy et al., 2013), explaining the opal deposition events across the Subarctic Pacific. Iron limitation curbing the efficiency of the biological pump also explains a nearby pCO_2 record which shows excess near-surface CO_2 during the highest productivity (**Figure 2a**, Gray et al., 2018). If the high Si supply within the B-A and early PreBoreal

primarily reflects an HNLC regime, then significant instances of deep water overturn and CO_2 outgassing may have occurred only briefly at the onsets of those intervals. This corresponds to two interludes of rapid atmospheric CO_2 rise recorded in Antarctic ice (Marcott et al., 2014). While Southern Ocean changes account for large intervals of CO_2 rise during HS1 and the Younger Dryas, brief but significant interludes at 14.8 and 11.7 ka display a higher $\delta^{13}C$ signature than the Southern Ocean events (Anderson et al., 2009; Bauska et al., 2016). This signature can be explained by rapid phytoplankton growth at a marine outgassing site, along with rapid incorporation of ^{12}C by land plants in the Northern Hemisphere (Yu et al., 2010), congruous with the B-A and PreBoreal productivity in the Subarctic Pacific.

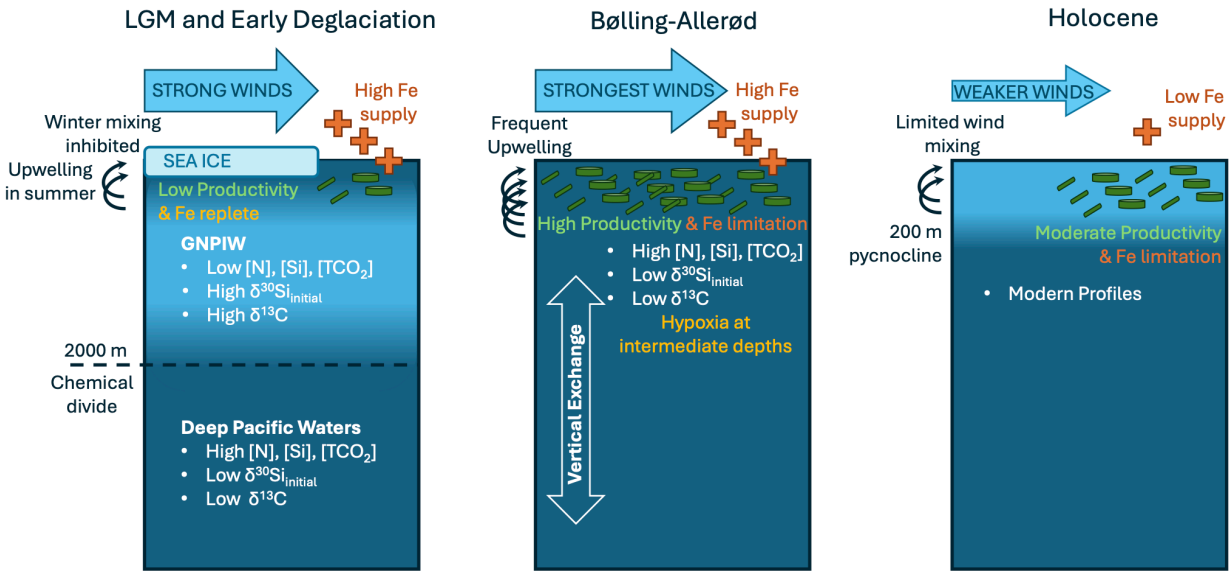

Figure 1.4: Schematic to demonstrate major changes during the deglaciation. The schematic represents the most cohesive explanation considering the newly presented $\delta^{30}Si_{Coscinodiscus}$ and diatom species records. The LGM and early deglaciation are characterized by low productivity despite high Fe supply, suggesting macronutrient limitation (or light co-limitation) related to sea ice and GNPIW dynamics; this explains the low Si supply and high $\delta^{30}Si_{Coscinodiscus}$ values. The B-A is characterized by high productivity and the alleviation of macronutrient limitation, driven by vertical exchange introducing formerly Deep Pacific Waters to the surface ocean; deep winter mixing, frequent upwelling, and possible iron limitation explain the high Si supply and moderate $\delta^{30}Si_{Coscinodiscus}$ values. Finally, the HNLC Holocene is characterized by moderately high productivity and iron limitation driven by low Fe supply and a strong pycnocline limiting winter mixing; this explains the high Si supply and low $\delta^{30}Si_{Coscinodiscus}$ values.

6 Conclusions

In summary, we suggest the high-productivity deglacial events of the Subarctic Pacific were caused by macronutrient supply that outpaced iron supply. This was precipitated by a unique mode of Pacific circulation where an annual resupply of nutrients fueled by wind-driven winter mixing tapped formerly deep, long-sequestered waters. The trigger for this operational mode may have been surface freshening shutting down intermediate water formation and favoring internal mixing

(Walczak et al., 2020), atmospheric changes indicated by ice cover (Detlef et al., 2020), or major changes in the global ocean (Rafter et al., 2022). The upwelling of aged deep water introduced silica and other nutrients to surface waters, fueling productivity and releasing old, long-sequestered CO_2 to the atmosphere. Brief intervals of CO_2 release may explain the sharp rises of atmospheric CO_2 at 14.8 and 11.7 ka. This source of CO_2 to the global atmosphere during the B-A drove the deglaciation forward, as it contributed to Northern Hemisphere warming and continued atmospheric CO_2 accumulation during an interval when the Southern Ocean was a net carbon sink during the Antarctic Cold Reversal. We conclude CO_2 from the Subarctic Pacific played an important role in the deglaciation and should be considered as a source for other analogous global climate events.

Supplemental Text S1. New Age Model and Reservoir Ages for U1340

We created a new age model for U1340 (53°24N, 179°31W, 1295 m depth) using previously published radiocarbon data and the occurrence of laminated intervals. The new age model is shown in Table S1. All radiocarbon data, originally published in Schlung et al. 2013, were re-calibrated using Calib 8.2 (Stuiver & Reimer, 1993), which incorporates the global ocean reservoir correction (R) from Marine20 (Butzin et al., 2017). We use a local reservoir correction (ΔR) of 225 ± 300 years after Schlung et al. 2013. The re-calibrated radiocarbon dates are shown in Table S2.

Three of these re-calibrated radiocarbon dates are used in the new age model. The age model is also based on four tie points to the Greenland Ice Core (GISP) chronology based on the occurrence of laminated sedimentary intervals, which are thought to be regionally synchronous (Kuehn et al., 2014). In two cores in the northern Bering Sea, also at intermediate depths (1107 m and 1111 m), the laminae were determined to be annual and the number of laminae were directly correlated to the number of years in the GISP record for the warm phases of the Bølling, Allerød, and PreBoreal (Kuehn et al., 2014). For the initiation of the laminated intervals at U1340, we use the dates established by Kuehn et al. (2014) of 14.64, 13.90, and 11.65 ka for the initiation of the Bølling, Allerød, and Pre-Boreal laminated intervals respectively. The beginning of the Younger Dryas, marked by the end of the Allerød laminations and a change to more terrigenous sediment, is given the established date of 12.84 ka (Kuehn et al., 2014).

We consider the above chronology based on the occurrence of laminated intervals to be more reliable than the radiocarbon data across these intervals, because the sudden shift to higher primary productivity and intermediate-depth hypoxia is thought to have occurred synchronously across the region (e.g., Detlef et al., 2020; Kuehn et al., 2014). In contrast, reservoir ages are known to have been strongly affected by the changes in regional circulation during the various periods of the deglaciation (e.g., Rafter et al., 2022; Sarnthein et al., 2013 and refs therein). An age model based on radiocarbon alone places the occurrence of the Bølling high productivity and benthic hypoxia ~600 years earlier than other cores in the region, and places the PreBoreal hypoxia ~1200 years earlier, which is unlikely to be correct (Schlung et al., 2013). Furthermore, all five radiocarbon dates from these intervals are age-reversals when the lamination-based age model is used. Instead, the five radiocarbon dates which are not used in the age model are used to generate new reservoir (ventilation) ages.

These five new reservoir (ventilation) ages are shown in Table S2. Marine reservoir ages are defined by planktic microfossil ^{14}C minus the contemporaneous atmospheric ^{14}C as calculated by IntCal20 (Reimer et al., 2020) and therefore represent R + ΔR. The modern whole-ocean R is approximately 550 years at year 0 B.P. (Butzin et al., 2017); and the modern local ΔR is approximately 225 years (Reuther et al., 2021; Schlung et al., 2013), meaning the local reservoir age in the modern Bering Sea is estimated to be 775 years (i.e., 550+225 years). All five new ventilation ages are higher than the modern estimate of 775 years, but within the

range of values found in polar regions during the LGM; values from 1000-2000 were typical in polar regions, where sea ice cover has a strong effect on air-sea gas exchange (Butzin et al., 2017; Heaton et al., 2023). The high ventilation ages throughout the deglaciation may indicate the presence of aged (radiocarbon-depleted) deep waters upwelling to the surface (see main text). This interpretation is potentially corroborated by the notable minima in benthic-planktic ^{14}C offsets throughout this interval: as low as 350 years during the Younger Dryas, in contrast to a modern estimate of ~1200 years (Schlung et al. 2013; shown in Table S2). The highest reservoir age of 1970 ^{14}C years, which occurs at 10154 ka, could indicate very minimal mixing with the atmosphere during the Boreal period. However, we caution that firm conclusions concerning the timing of these changes cannot be drawn from these few values. Future work should obtain a higher-resolution record of ventilation (reservoir) ages to investigate regional circulation changes.

Supplemental Table 1.1: Age Model for U1340.
*The uncertainty for this age point reflects the large potential range in reservoir ages during this interval, which is larger than the analytical uncertainty.

Sample	Depth	Age	Uncertainty	Citation	Sed. Rate
	(MCD)	years B.P.	± years		(cm/kyr)
U1340A 1H 01 0-5 cm planktics	-0.0355	5770	350	Schlung et al. 2013	19
Laminated interval initiation (Pre-Boreal initiation)	1.0945	11650	20	Kuehn et al. 2014	7
Laminated interval end (Younger Dryas initiation)	1.1795	12840	20	Kuehn et al. 2014	17
Laminated interval initiation (Allerød initiation)	1.3645	13900	20	Kuehn et al. 2014	64
Laminated interval initiation (Bølling initiation)	1.8415	14640	20	Kuehn et al. 2014	53
U1340A 1H 03 42-47 cm planktics	3.3850	17570	630*	Schlung et al. 2013	54
U1340A 2H 03 112-116 cm planktics	9.172	28190	360	Schlung et al. 2013	

Uncertainty values in our age model, shown in Supplemental Table 1.1, are ± 20 years for the tie points to the Greenland ice cores because the correlations are based on a 20-year integrated curve (Kuehn et al., 2014). Uncertainty for the initial and glacial radiocarbon tie points reflect the radiocarbon uncertainty as calibrated in Calib 8.2. During the deglaciation, however, our age model uncertainty is higher than the radiocarbon calibration due to the reservoir age findings described above. That is, our original range of uncertainty in ΔR was 600 years for all data points (± 300) based on the modern ocean; however, the new reservoir ages suggest the range in ΔR was much larger. The highest range between adjacent reservoir ages is 1255 ^{14}C years (1970 ^{14}C years in the early Holocene vs. 715 years ^{14}C in the mid-Holocene),

suggesting the potential for reservoir age changes is ± 630 years, larger than modern estimates supposed (Heaton et al., 2023). Therefore, the uncertainty for radiocarbon-based age dates during the deglaciation is more realistically ± 630 years (noted in Supplemental Table 1.1 at age point 17570 years B.P.).

Supplemental Table 1.2: Radiocarbon Data. After calibration, radiocarbon data are rounded to nearest 10 years; IntCal data and reservoir ages are rounded to nearest 5 years. All measured radiocarbon data originally published in Schlung et al. 2013.

Sample	Depth (MCD)	^{14}C Age ^{14}C years	ΔR ^{14}C years	Calib 8.2 Median Probability years B.P.	Assigned Age in new Age Model years B.P.	Ventilation (Reservoir) Age ^{14}C years	Δ ^{14}C benthic - planktic ^{14}C years
U1340A 1H 01 0-5 cm planktics	-0.0355	5800 ± 35	225 ± 300	5770 ± 350	5770	715	
U1340A 1H 01 84-89 cm planktics	0.8070	10890 ± 57	225 ± 300	11820 ± 450	10154	1970 ± 80	2420
U1340A 1H 01 117-122 cm planktics	1.1350	11980 ± 35	225 ± 300	13090 ± 330	12217	1560 ± 55	370
U1340A 1H 01 122-127 cm planktics	1.1850	12440 ± 35	225 ± 300	13610 ± 380	12872	1475 ± 55	350
U1340A 1H 02 21-22 cm planktics	1.6545	13440 ± 40	225 ± 300	15000 ± 480	14347	1050 ± 65	890
U1340A 1H 02 42-47 cm planktics	1.8850	13640 ± 40	225 ± 300	15300 ± 460	14723	1240 ± 90	1070
U1340A 1H 03 A/W 42-47 cm planktics	3.3850	15420 ± 64	225 ± 300	17570 ± 390	17570	955	9190
U1340A 2H 03 112-116 cm planktics	9.1720	25090 ± 120	225 ± 300	28190 ± 360	28190		

Supplemental Text S2. Expanded Methodology and Error Reporting

Silica weight percent (biogenic opal) was measured on 76 samples. 7.5 mg of sample was placed in a 0.1 M Na_2CO_3 solution at 85°C for four hours, cooled to room

temperature overnight, and 100 µL were reacted with a molybdate blue complex. Absorbances were measured at 812 nm on a Thermo-Scientific Evolution 220 UV-visible spectrophotometer at the USGS Pacific Ocean Paleoclimate Lab in Menlo Park, CA. Weight percent values (Figure S1) assume 10% hydration ($SiO_2 \cdot 0.4\ H_2O$); error bars show a replicate-derived error of ±1.54%, representing the average 1-σ standard deviation for 26 sample replicates. The 1-σ standard deviations for Claystone, Diatomite, & Karluk Lake in-house standards were ± 1.68, 3.93, and 0.06 wt% respectively for these runs (n=5).

Thorium and Uranium were measured on 21 samples. The Thorium and Uranium error bars are the replicate range from the larger of two sample replicates (replicates are shown in Figure S1). Sediment mass accumulation rates (MARs) were calculated using the 230Th-normalization method, which corrects for sediment focusing (Costa et al., 2020). We use opal flux (opal weight % multiplied by ^{230}Thorium MAR) as the primary method to quantify primary productivity for use in further calculations (e.g., silica supply). The maximum replicate error on the opal flux calculation (Figure 2, main text) is ±0.29 $g \cdot cm^{-2} \cdot kyr^{-2}$.

Silicon isotopes were measured on 42 samples. Our reported $\delta^{30}Si_{\textit{Coscinodiscus}}$ values represent the average of 3 – 6 runs and error bars are the standard deviation for each sample's measurements. The long-term average values of inter-lab silica standards (‰) vs. NBS 28 (National Bureau of Standards Silica) are given in Table S3.

Supplemental Table 1.3: $\delta^{30}Si$ values for Inter-lab Standards Diatomite and Big Batch.

	$\delta^{29}Si$ ‰	$\delta^{30}Si$ ‰		$\delta^{29}Si$ ‰	$\delta^{30}Si$ ‰
Diatomite	0.68	1.31	Big Batch	-5.61	-10.88
1-σ	0.09	0.11	1-σ	0.07	0.14

The analytical error for the $\delta^{13}C_{Uvigerina}$ record was reported to be ±0.05‰ in Schlung et al. (2013); however, the uncertainty of DIC $\delta^{13}C$ is much larger. A regional study of foraminiferal stable isotopes (Cook et al., 2016) compiled benthic $\delta^{13}C$ from the Bering Sea and found that coretop $\delta^{13}C_{Uvigerina}$ was offset from nearby hydrocasts, particularly at intermediate depths. While hydrocast DIC $\delta^{13}C$ from 700-1470 m depths measured -0.6 to -0.5‰, $\delta^{13}C_{Uvigerina}$ averaged -0.95‰ (v. PDB). With the canonical calibration of +0.9‰ (Alan C. Mix et al., 1995), this results in an offset of $\delta^{13}C_{Uvigerina}$ to more positive values than DIC, 0.4±0.2‰ too high (Cook et al., 2016). The authors investigated the possibility that this offset was due to vital effects related to infaunal behavior linked to surface productivity but found no correlation. Instead, they suggested a carbonate ion effect due to the intense OMZ in the region (Cook et al., 2016). We therefore use the regional offset of 0.4‰ to correct our $\delta^{13}C_{Uvigerina}$ values but acknowledge the large uncertainty in this calibration. The conclusions that we describe in the main text are only those where shifts in benthic foraminiferal $\delta^{13}C$ are greater than these uncertainties.

Supplemental Text S3. Productivity Proxies and Particle Fluxes

The three productivity proxies at our site, Opal weight percent (wt%), ^{230}Thorium MAR, and diatom valve counts, generally agree on the timing and

magnitude of productivity changes. Opal wt% and diatom valve counts are both direct proxies for diatom production, but both are inextricably tied to preservation. When surface production is high, more opal is preserved (dissolved silica in bottom water sediments creates ideal conditions for preservation). Site U1340 underwent extreme environmental changes during the deglaciation, and we expect both records are influenced by this positive feedback between production and preservation.

Diatom valve counts are a quantitative count of all intact diatom valves visually identified on microscope slides. An intact diatom valve is any valve where more than half of a centric diatom valve is present, or one complete end of a pennate diatom valve is present (Schrader & Gersonde, 1978). This methodology means that where dissolution and fragmentation have degraded opal material, diatom counts will under-represent surface productivity. The period from 20 – 15 ka in particular was marked by many fragmented diatom pieces which could not be identified and thus are not included in the valve counts. This interval may have experienced post-depositional benthic dissolution. Conversely, the laminated intervals of the Bølling and Allerød contain many finely-silicified diatoms which display excellent preservation despite not always being preserved in sediments due to their fragile construction (e.g., *Thalassiosira hyalina* (Grunow) Gran *and Thalassiosira gravida* Cleve). The methodology employed to measure opal wt% is designed to dissolve biogenic opal from diatoms, creating a record of diatom primary production, without dissolving thicker opal from radiolarians or sponge spicules (Mortlock & Froelich, 1989). Visual inspection of our sample material post-processing suggested that some

thickly-silicified diatoms in our samples were not fully dissolved in the sample processing (e.g., *Coscinodiscus* Ehrenberg species, *Rhizosolenia* Brightwell species). The resulting weight % opal presented here may therefore be an under-representation of diatom opal in certain high-opal samples.

The good agreement between the opal wt% and diatom valve counts bolsters confidence in the accuracy of our measurements. Opal wt% and diatom valve counts were generated by independent methods and show a similar pattern, including relatively low productivity during the LGM and early deglaciation, a sudden, rapid increase in productivity during the Bølling-Allerød (B-A), a decrease during the Younger Dryas (YD), a second rapid increase during the Pre-Boreal, which is less intense than the productivity of the B-A, a small minima in the early Holocene, and an increase towards the coretop.

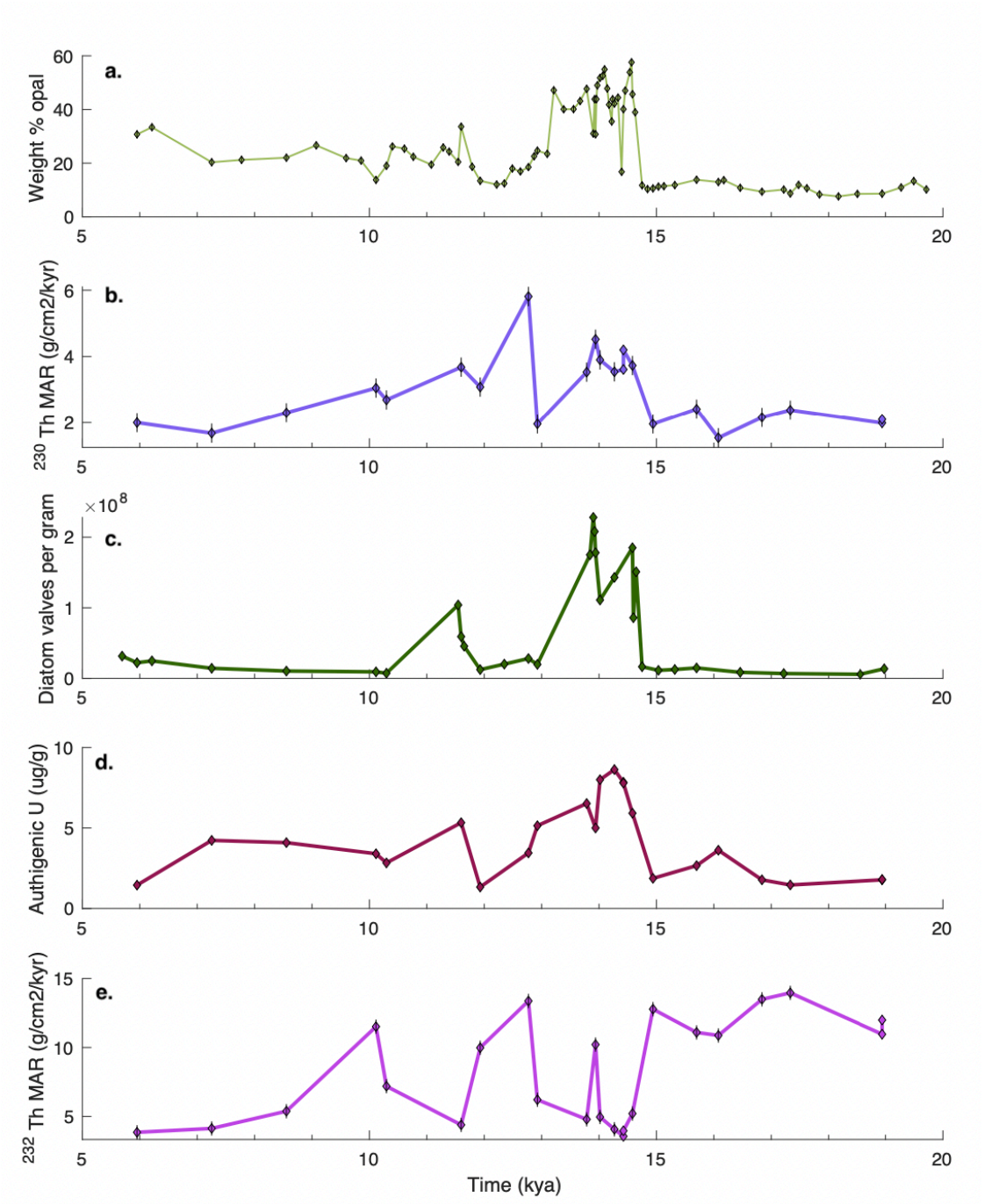

Supplemental Figure 1.1: Productivity proxies and particle fluxes. All five of the proxies shown represent different approaches to quantify primary production or other particle fluxes to the sediments. Error bars indicate replicate variability. (a) Weight percent biogenic opal, light green; (b) ^{230}Thorium MAR (g/cm^2/kyr), purple; (c) diatom valve counts (valves/gram), dark green; (d) authigenic Uranium (ppm), maroon; and (e) ^{232}Thorium MAR (g/cm^2/kyr), pink.

The mass accumulation rate of ^{230}Thorium (^{230}Th MAR) is a measure of all biogenic particles, not only opal production. Our ^{230}Th MAR generally agrees with the two opal proxies but differs mainly by having an extreme high point in the Younger Dryas. This record of ^{230}Th MAR is already corrected for non-biogenic particle flux (^{232}Th), so the high point should not be influenced particles such as ash. It is more likely that this high point reflects a time of high production by non-diatom plankton such as coccolithophores, cyanobacteria, and small eukaryotes. We can anecdotally confirm a high $CaCO_3$ content in the YD as well as the B-A samples, although we did not measure weight percent $CaCO_3$. The benefit of ^{230}Thorium is that, unlike biogenic opal, its presence in the sedimentary record is relatively unaffected by post-depositional dissolution. We therefore use opal flux (opal wt% · ^{230}Thorium MAR) ($g \cdot cm^{-2} \cdot kyr^{-2}$) to quantify primary productivity in further calculations.

The concentration of authigenic uranium (U_{auth}) is a benthic oxygenation proxy; the formation of authigenic uranium is highly sensitive to low-oxygen conditions. The timing and magnitude of the U_{auth} proxy agrees with the occurrence of the sedimentary laminations in our record (e.g., yellow bars in Figure 2) indicative of a hypoxic depositional environment and concurrent with a lithology change to high opal accumulation. Although benthic oxygenation is also affected by circulation, which also changed during the deglaciation, the U_{auth} at U1340 appears to be

primarily influenced by surface productivity as it follows a similar trend to the productivity proxies above.

The mass accumulation rate of ^{232}Thorium (^{232}Th MAR) is a proxy for non-biogenic particles, such as ash, dust, and ice-rafted debris (IRD). At this site location, we expect ^{232}Th MAR to mainly reflect IRD (Serno et al., 2014). IRD is visually present as sand- and silt-sized grains in many samples, and may have been locally sourced from sea ice rafting or marine-terminating glaciers in the Aleutians or Cordilleran Ice Sheet. IRD appears to have been high throughout most of the LGM and early deglaciation, with a rapid decrease concurrent with the warm Bølling, Allerød, and P-B intervals (Figure S1). This finding is similar to the "volcanic component" of the detrital flux (i.e., IRD and ash, but not dust) that reached the open SNP, which also decreased during the B-A (Lam et al., 2013). In our record, there is also a resurgence of IRD during cold intervals including the YD, and, surprisingly, the end of the Older Dryas period around 13.9 ka and again at the close of the PB around 10.2 ka.

Changes in ^{232}Th MAR are inverse to productivity changes, and most tightly linked with benthic U_{auth} (R^2 = -0.7 for linearly-detrended residuals, excluding the near-coretop Holocene data point). These ^{232}Th MAR fluctuations, in sync with global climate shifts, suggest that ice behavior was tightly linked to the regional circulation, nutrient supply, and productivity changes described in the main text.

Supplemental Text S4. Utilization model

4.1 Open vs. Raleigh system

Based on modern observations in the Subpolar North Pacific and its marginal seas, spring and summer blooms are best represented by a seasonally closed Si supply with Rayleigh fractionation and ~75% utilization, while fall blooms are likely fueled by increased mixing and an open or steady state system (Giesbrecht et al., 2022; Reynolds et al., 2006). We choose an open state model for three reasons: (1) our 1-cm sediment samples are integrating on long timescales oceanographically; (2) *Coscinodiscus* is a fall-bloom genus; and (3) silica is abundant in regional surface waters, so it is unlikely to reach >90% utilization where the Rayleigh and steady-state models diverge the most isotopically.

4.2 The fractionation factor, epsilon (ε)

Culturing studies have found that most diatoms have fractionation factors, denoted ε, of -1.1 ± 0.4‰ (± 1SD), with little to no variation due to species, temperature, or silicic acid-availability effects (De La Rocha et al 1997). To our knowledge, no *Coscinodiscus* Ehrenberg species have been tested in culturing experiments; and there is some evidence that ε is higher in particular species of polar diatoms and can change when grown in iron-limiting conditions (Meyerink et al., 2017). Perhaps more useful than culturing experiments are "apparent" ε values calculated from in-situ gradients between $\delta^{30}Si$ values and silicic acid concentrations in the region. In the open Subarctic North Pacific, apparent ε values are as low as -0.4‰ due to the mixing of water masses with different preformed values (Reynolds et

al., 2006). (This study was performed in spring before the majority of productivity occurred). On the Bering Shelf, apparent ε values of -1.18 ± 0.02‰ (1SE) characterize Bering Shelf Water during peak growing season. In the modern ocean, this water flows into the Arctic; but in the past when the Bering Strait was closed, Bering Shelf Water may have flowed towards our site. A value between -0.4 and -1.2‰ is probably the best approximation for our site. We therefore chose to use the traditional value of -1.1‰ for discussion in the main text. As long as ε is a constant value, as is expected for a single species, a different value of ε does not affect the conclusions of the paper. Visual inspection suggested our samples were >95% *Coscinodiscus marginatus* Ehrenberg with occasional *Coscinodiscus oculus-iridis* (Ehrenberg) Ehrenberg and *Coscinodiscus radiatus* Ehrenberg present. We expect these closely related species to have a similar ε to *C. marginatus*.

4.3 Choice of $\delta^{30}Si_{initial}$ for "simple model" (1.7 ‰)

In-situ studies of $\delta^{30}Si$ of silicic acid are scarce in the SNP and its marginal seas. Much of the surface water at our site is from the lateral advection of the Alaskan Stream, which sources water from the Gulf of Alaska (Carton et al., 2018). However, there are no studies of in-situ $\delta^{30}Si$ in the Gulf of Alaska or the open Bering Sea. We therefore use an estimate of $\delta^{30}Si_{initial}$ from a global model which finds an average value of 1.7‰ for the North Pacific region (Pichevin et al., 2020). This value agrees reasonably well with the data from two nearby locations: one site in the open SNP found surface waters were 1.14-1.23‰ in May, at the beginning of the growing season when silica was abundant (Reynolds et al., 2006). Another site on the Bering

Shelf, where Si recycling is more rapid, found values of 1.94-2.12 ‰ in July at the peak growing season (Giesbrecht et al., 2022). The true value for $\delta^{30}Si_{initial}$ at our site is likely along a mixing line between Bering Shelf Winter Water and thermocline-level SNP water, which is consistent with the average value of 1.7‰ from the global model.

4.4 Choice of $\delta^{30}Si_{initial}$ for Monte Carlo simulation (values of 1.6 ± 0.56‰)

To constrain how the value of $\delta^{30}Si_{initial}$ could have changed from the LGM to the Holocene, we found the range of $\delta^{30}Si$ values that may have reached our site from both lateral and vertical advection.

In the modern ocean, nearly all of the surface water (>300 m) at site U1340 arrives via lateral advection (Carton et al., 2018). Currents around the Aleutian Islands can cause lateral advection from all directions, but the majority of the lateral transport is from the westward Alaskan Stream, which sources water from the Gulf of Alaska (Carton et al., 2018). To estimate the possible $\delta^{30}Si$ of these waters, we use $\delta^{30}Si_{diatom}$ values measured in *Coscinodiscus* in the Gulf of Alaska from the deglaciation (Maier et al., 2015) (Figure S3). The values of *Coscinodiscus* in the Gulf of Alaska are more likely to represent complete utilization (because it is further from the core of upwelling waters, e.g., Yoshikawa et al., 2018); any silica used there may be partially or fully remineralized by the time it reaches our core site. Thus, the range of 2.04 to 1.16 ‰ (1σ of 0.12‰) represents the possible range of values for lateral advection to our site (i.e., 1.6 ± 0.56‰).

In addition, we estimated the $\delta^{30}Si$ from vertically advected waters. In the modern ocean, intermediate SNP waters (100-600 m depth) have values between 1.14 to 0.72 ‰ ± 0.14 (2SD) (Reynolds et al., 2006). The supply of silicic acid to our site from these depths is very small in the modern ocean compared to lateral advection, however both the magnitude of supply and the $\delta^{30}Si$ of vertically advected waters may have been different over the last twenty thousand years, requiring further estimates across this timescale. Very little data exists from which to estimate deglacial changes in $\delta^{30}Si$ at depth; but one study examined how the nutrient content of intermediate water may have differed during the LGM (Cook et al., 2016). During the LGM, benthic $\delta^{13}C$ from 700-1000 m depth in the Bering Sea (which we presume to be in the core of Glacial North Pacific Intermediate Water) was 0.14‰ heavier than the Holocene value (Cook et al., 2016). This heavier $\delta^{13}C$ suggests more regional recycling of nutrients, which would correspond to a lower concentration of silicic acid, [dSi], than the modern. If we assume that the $\delta^{13}C$ change can be correlated to silicic acid concentrations using a modern hydrocast from the Bering Sea, the 0.14‰ heavier $\delta^{13}C$ equates to a difference of ~5 µmol/L [dSi], or 67 vs. 72 µmol/L (Dickson et al., 2000). From this change in silicic acid concentration, we can estimate the corresponding change in $\delta^{30}Si$ using the global compilation of [dSi] and $\delta^{30}Si$ in (Reynolds, 2009). This correlation predicts that a change from 72 to 67 µmol /L [dSi] equates to a change of 0.04‰ $\delta^{30}Si$ (a change from 1.14‰ in the Holocene to 1.18‰ at the LGM). This change is much smaller than the potential error associated with the

assumptions involved and is fully encompassed by the range of lateral values described above.

Therefore, any change in silicic acid due to increased vertical advection from NPIW would be isotopically indistinguishable from laterally advected silicic acid from elsewhere in the region. This is not surprising because much of the modern SNP contains high concentrations of silica in near-surface waters, so lateral transport of silicic acid would be the immediate source silicic acid. This does not negate our approach because on a geologic timescale, the ultimate source of silicic acid to the entire region, including the Gulf of Alaska and the other marginal seas of the Subarctic North Pacific, is from vertical upwelling.

4.5 Comparison with Regional $\delta^{30}Si_{Coscinodiscus}$ records

Overall, there is agreement between the $\delta^{30}Si_{Coscinodiscus}$ record from Site U1340 in the Bering Sea (this study) and those from Site MD01-2416 in the northwest Subpolar North Pacific (SNP) and Site SO202-27-6 in the open Gulf of Alaska (GoA) (Maier et al., 2015). The near-coretop (5-7 ka) values are similar in all three records. Collectively, all three records also suggest relatively low Si utilization during the B-A and early PB intervals, supporting the conclusion that Si was underutilized, or sourced from deep waters with a lower $\delta^{30}Si_{initial}$, during the high-productivity events.

During the LGM and early deglaciation, i.e., 19-15 ka, both the GoA and Bering Sea sites have the most extreme ranges of $\delta^{30}Si_{Coscinodiscus}$ values in their respective records. In the GoA, these large changes in $\delta^{30}Si_{Coscinodiscus}$ were attributed

to temporary stratification events, recorded in $\delta^{18}O_{Coscinodiscus}$ and interpreted as sea surface salinity changes. Temporary stratification events likely explain the large $\delta^{30}Si_{Coscinodiscus}$ changes in the Bering Sea as well; however, the resolution of both records may be too low, compared to the duration of these events, to determine how closely synchronized the GoA and Bering Sea were during these events. Lower sea levels and extension of the CIS would have fully blocked the shallow passes that today connect the Bering Sea to the Gulf of Alaska, meaning that different stratification dynamics could have occurred during this interval.

=

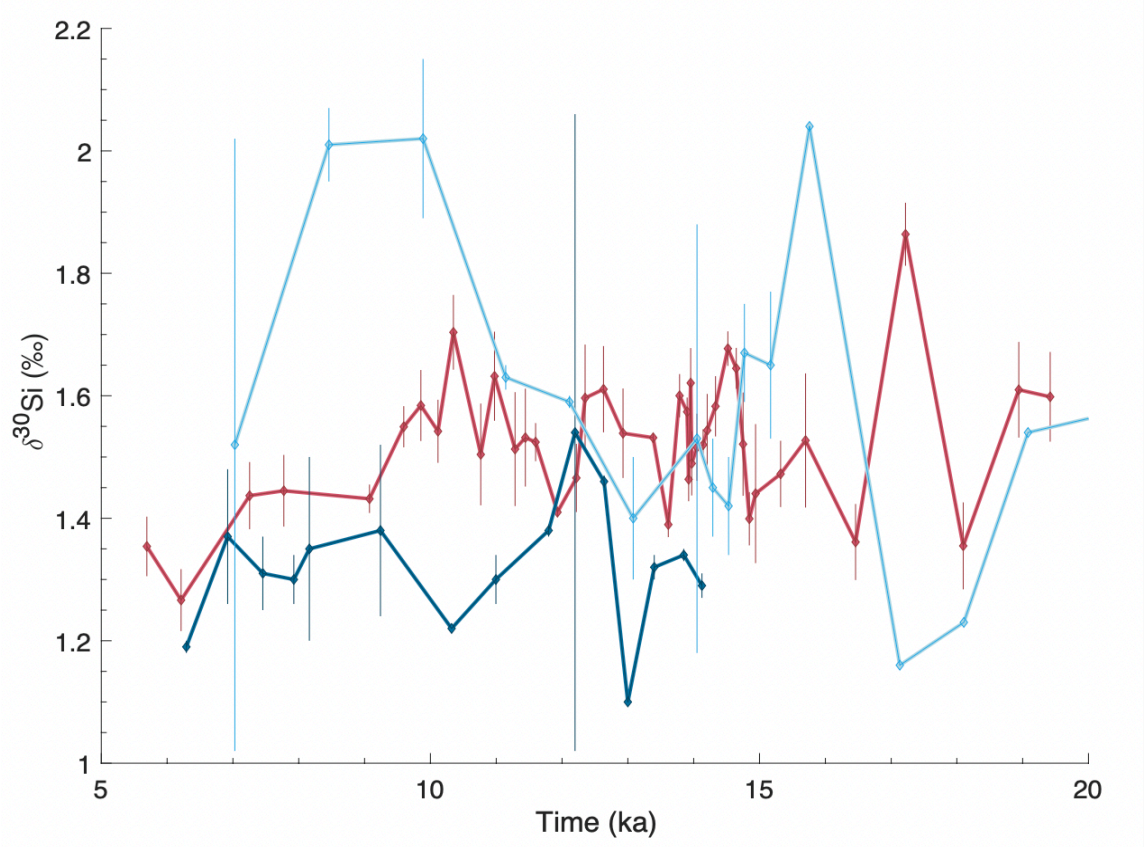

Supplemental Figure 1.2: Comparison of $\delta^{30}Si_{Coscinodiscus}$ values from Site U1340 (red, this study) with Site MD01-2416 in the northwest open Subpolar North Pacific (dark blue) and Site SO202-27-6 in the open Gulf of Alaska (light blue) (both from Maier et al., 2015).

From 10-15 ka, i.e. the B-A, YD, and PB, the higher absolute values in the Bering Sea compared to the NW SNP record could suggest that the core of nutrient upwelling, with a low $\delta^{30}Si_{initial}$ signature, occurred more intensely in the SNP. Alternatively, it could be that iron limitation was more intense in the open SNP than the Bering Sea, while U1340 in the Bering Sea was closer to iron sources from the continental shelf, increasing Si utilization. Both the Maier et al. 2015 sites display local minima in values in the early Younger Dryas, which we did not find in our record; this could be due to discrepancies in age models, sampling gaps which alias the abrupt changes in the $\delta^{30}Si$ records, or differences in biogeochemical cycling between the regions.

Site U1340 shows increasing Si utilization (increasing $\delta^{30}Si_{\textit{Coscinodiscus}}$ values) at the end of the Preboreal, similar to the GoA site. This similarity may be related to circulation changes in the region, when higher sea levels would have better connected the Bering Sea to the Gulf of Alaska. The Holocene (5-7 ka) values roughly converge in all three records, and generally display lower values than the deglaciation.

Supplemental Text S5. Iron, Si:N, and Diatom Groups

In the main text we frequently refer to genera rather than species to simplify the interpretation and refer to several groups of diatoms that merit further explanation. The species present at our site, the groups they are assigned to, and rationale for their characterizations as environmental indicators are explained below.

Iron supply by dust to the open Subarctic North Pacific was measured by Lam et al., 2013 and Serno et al., 2015. Both studies found iron supply was high during the

LGM and most of the deglaciation, with a decline after ~12 ka. The dust flux from Serno et al. 2015 is shown in Figure S4. At our site, the detrital flux (^{232}Th MAR) signal is likely dominated by IRD rather than dust (Serno et al., 2014); it is high during cold intervals and low during warm intervals (Figure S1). Although IRD can provide a source of iron during spring ice melt, the detrital flux deposition at our site is inversely correlated to productivity, so this iron source cannot explain the high-productivity of the B-A and PB. In sum, the particle flux records find no evidence for iron fertilization. However, another potential iron source, remobilized iron from flooding continental shelves, has also been hypothesized to have caused iron fertilization during the B-A (Davies et al., 2011). This iron may have been introduced in a dissolved or colloidal form, and thus would not be included in any detrital flux records. We therefore chose to interrogate the diatom community composition, which should respond to any iron source, for evidence of iron limitation.

5.1 *N. seminae* abundance and Si:N as HNLC indicators

The evidence for *Neodenticula seminae* (Simonsen & T. Kanaya) Akiba & Yanagisawa indicating HNLC conditions in the Subarctic Pacific are manifold. Recent work has found that *in situ N. seminae* abundances in the North Pacific are highly correlated with trace amounts dissolved iron, suggesting that *N. seminae* is the diatom that best responds to very low or very brief levels of natural iron fertilization (Yoshida et al., 2020). In an incubation experiment, *N. seminae* was also the only species that continued to reproduce after seawater was treated with DFB, an iron-chelator that removes iron from seawater (Yoshida et al., 2023). This strongly

suggests that *N. seminae* is uniquely adapted to blooming in low-iron conditions. In addition to being the primary diatom to live in modern HNLC waters, *N. seminae* was one of the first responders to a large-scale iron fertilization experiment (SERIES), primarily due to its abundance before the iron enrichment began and its small size (i.e., high surface area-to-volume ratio) allowing for rapid iron uptake (Marchetti et al., 2006). After continued iron addition, other diatoms bloomed as well, including *Chaetoceros, Rhizosolenia and Thalassiothrix*, suggesting that these genera have higher iron requirements. The co-occurrence of *Chaetoceros* during intervals with abundant *N. seminae* does not contradict the characterization of those intervals as iron-limited, but may suggest a seasonality to iron limitation. It appears that *Chaetoceros* species typically bloom in iron-replete conditions, however temporary, with their luxury uptake during intense spring blooms potentially inducing iron limitation for subsequent seasonally occurring diatoms (Flynn et al., 2023; Yoshida et al., 2023).

On a geologic timescale, *N. seminae* abundances in the subarctic Pacific are known to be strongly linked with glacial-interglacial changes (Sancetta & Silvestri, 1986). Early work supposed that decreases in *N. seminae* during glacial periods could be due to low-temperature intolerance; however, *N. seminae* grows at temperatures around 7.5 °C in the modern ocean (J. Ren et al., 2014), and summer temperatures at our site based on alkenone thermometry are higher than this during the early deglaciation (19-16 ka) (Schlung et al., 2013) without increases in the abundance of *N. seminae*. We therefore newly suggest that some of the glacial-interglacial

variability in *N. seminae* abundances could be amplified by *N. seminae* being out-competed by other diatoms when iron is not limiting.

In the Bering Sea, *N. seminae* has also been interpreted as an indicator of the strength of the Alaskan Stream through narrow passes and therefore an indirect indicator of sea level rise in the region (Schlung et al., 2013; Stroynowski et al., 2015). However, the fluctuation of *N. seminae* with glacial/interglacial cycles occurs in the open western subarctic Pacific in addition to the Bering Sea (Sancetta & Silvestri, 1986) so its patterns of abundance in the region do not need to be related to sea level. The presence of *N. seminae* at our site during our earliest sample at 19 ka suggests that even at sea level low stands, there would be a seed population present in the Bering Sea which could allow *N. seminae* to bloom. Instead, the increases in *N. seminae* abundance in the Bering Sea that correlate to the input of the Alaskan stream could be due to the introduction of lower-iron waters from the Gulf of Alaska.

A global sediment trap compilation (Pichevin et al., 2014) suggests that the ratio between Si and organic matter is, on a broad scale, driven by high-nutrient, low-chlorophyl (HNLC) conditions. This may be because thickly-silicified frustules deter predation while awaiting unpredictable iron-deposition events (e.g., Assmy et al., 2013 and refs therein). The absolute values of Si:N ratios in sediments may also be influenced by other factors, such as preservation, which we detail below.

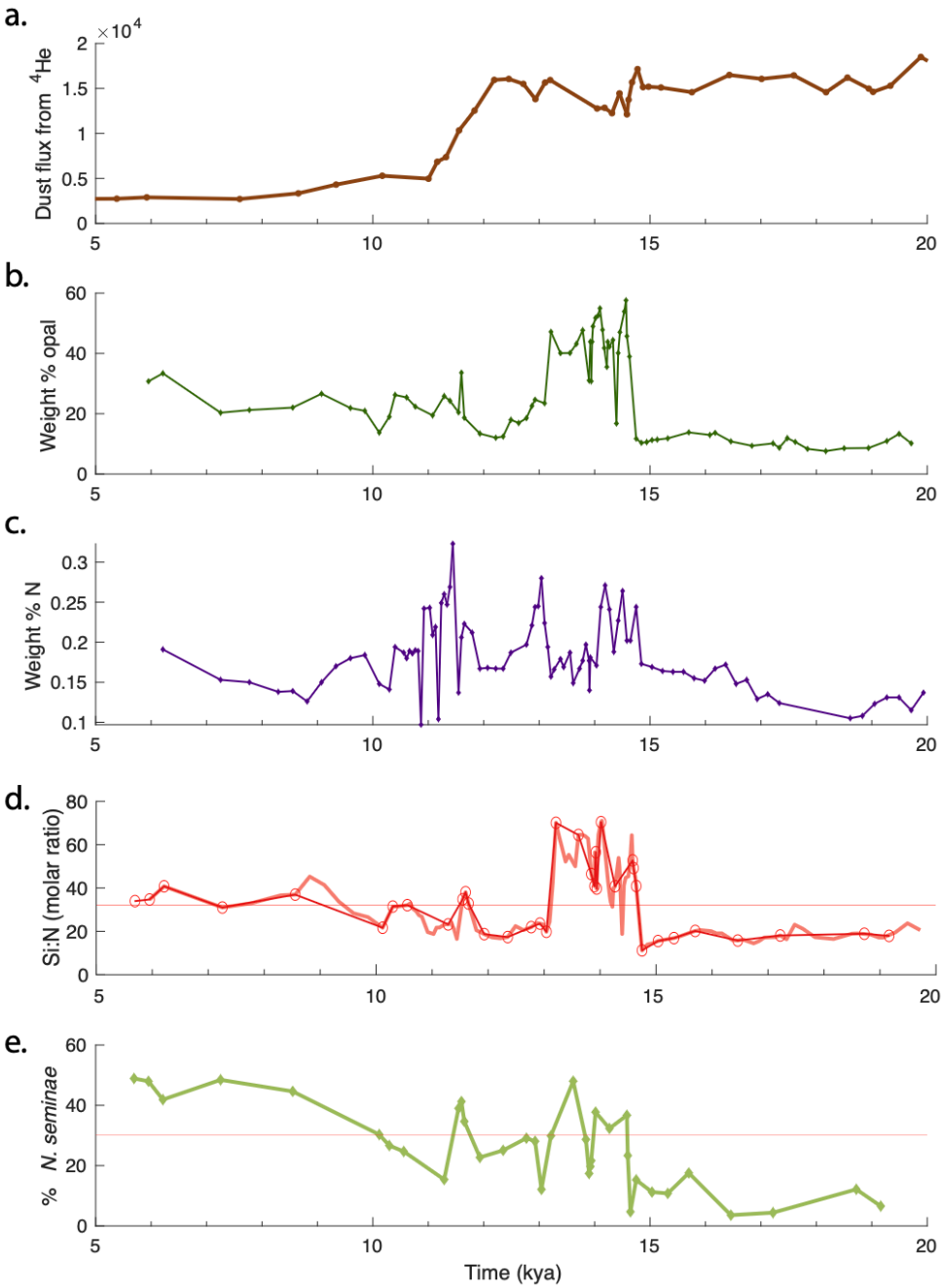

Supplemental Figure 1.3: Dust and Si:N. (a) Dust flux estimated from ^{4}He (Serno et al., 2015), (b) weight % biogenic opal, (c) weight % nitrogen, (d) molar ratio of Si to N, interpolated as a continuous record (faint red line) and subsampled as discrete points to match the diatom abundance timepoints (red circles and strong red line) (e) relative abundance of *N. seminae* (%). Horizontal lines at 32 Si:N and 31% relative abundance of *N. seminae* are included to aid in the visual interpretation.

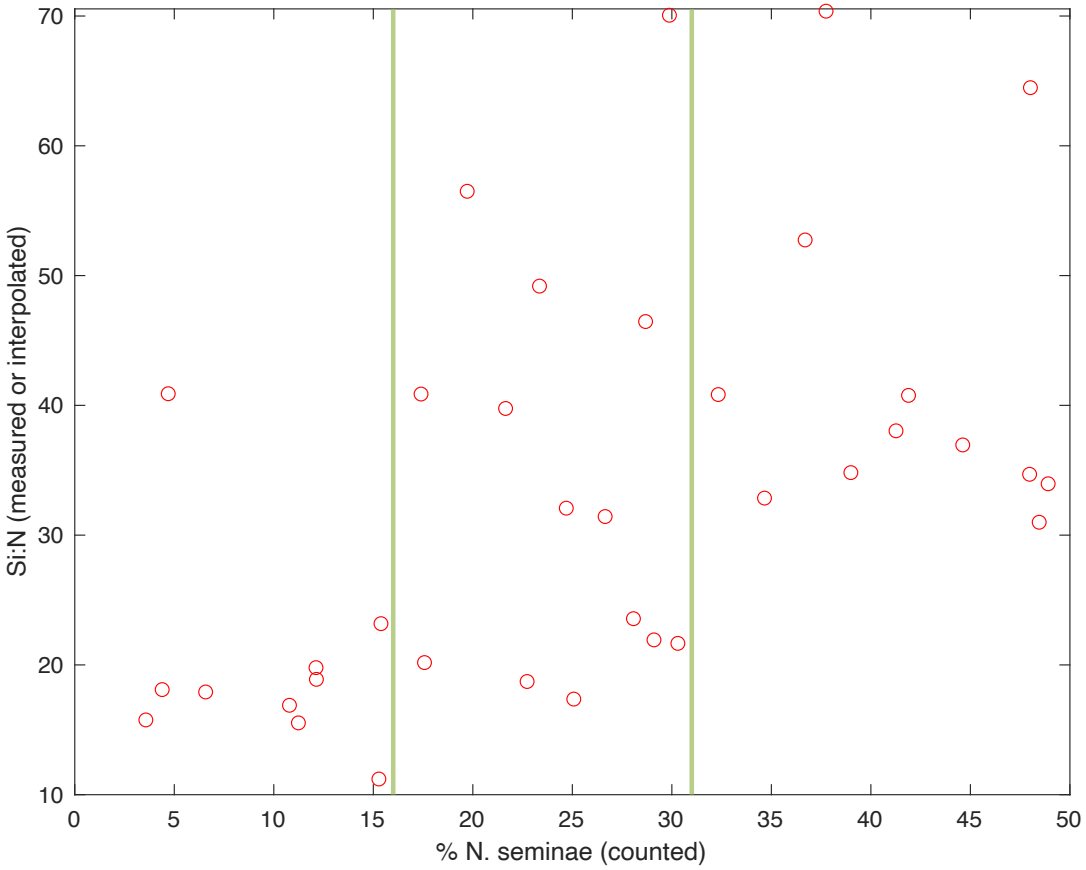

Supplemental Figure 1.4: Potential HNLC indicators, % *N. seminae* vs. Si:N. There is not a clear relationship; however, abundances of *N. seminae* above 31% are all associated with high Si:N ratios (>30) and abundances of *N. seminae* below 16% are all associated with low Si:N values (<23) or summer temperatures colder than 6°C.

We determined Si:N ratios in our samples to further examine the record for HNLC conditions. Bulk sediment $\delta^{15}N$ and weight% nitrogen (wt% N) were measured on an Elemental Analyzer coupled to an IRMS in the Stable Isotopes Laboratory at the University of California Santa Cruz using 80 mg of freeze-dried, pulverized, homogenized sediment samples. Some $\delta^{15}N$ values were reported in Schlung et al., 2013 and some are new to this study. The wt% N, shown in Figure S3,

is higher in the mid-deglaciation than at the LGM, like our productivity proxies; but the finer details do not closely agree to the other productivity proxies shown in Figure S1. Weight % biogenic opal (wt% Si) is shown in Figure S1 and again in Figure S3. We converted the measured wt% Si and wt% N data to molar Si:N ratios. Linear interpolation was used to create a continuous record of Si:N (Figure S3) because wt% Si and wt% N were sometimes not measured on the same samples. The resulting record of Si:N ranges from 11 mol/mol (at 14.8 ka) to 71 mol/mol (at 14.0 ka). This interpolation was subsampled to match the timescale of diatom relative abundance data (shown in Figure S3 as larger red circles).

Si:N ratios in sedimentary archives can be driven by many factors, broadly: (1) genuine shifts in surface community production and export, (2) remineralization in the water column, and (3) sedimentary processes including exposure at the sediment-water interface before burial, post-depositional diagenesis in sediments, and pore water saturation.

First, shifts in community production and export between diatoms vs. non-diatom organisms will be the primary influence on sediment trap Si:N values (Pichevin et al., 2014). This is because diatoms are the only organisms represented in the wt% Si measurement, which is designed to solely measure diatom opal and exclude other sources of Si in the sample (Mortlock & Froelich, 1989). On the other hand, both diatoms and many non-diatom organisms, including producers and consumers, are represented in the exported organic matter measured by wt% N. On a global scale, the relative abundance of diatom vs. non-diatom organisms is driven by

high-nutrient, low-chlorophyl (HNLC) conditions, where diatoms tend to thrive due to abundant Si availability and adaptations for low-iron environments (Pichevin et al., 2014).

Second, bacterial respiration in the water column prior to deposition can remineralize organic nitrogen very efficiently, meaning that a much smaller fraction of N production reaches the sediment at this site's depth (1295 m) compared to opal, which is relatively unaffected by water column conditions (Ragueneau et al., 2000). The removal of N in the water column will depend on the rain-rate of organic matter and the oxygen content of the water column (e.g. Martiny et al., 2014 and refs therein).

Given this strong control on N deposition, we assess water column conditions at this site using the ratio of organic carbon (C_{org}) to organic N (wt% N). C_{org}:N ratios are primarily affected by water column oxygenation in the upper few hundred meters (Martiny et al., 2014). At this site, C_{org}:N was found to vary from 8.4 - 10.3 mol/mol across this timescale (Schlung et al., 2013). Therefore, variability of up to 2 mol/mol Si:N may be the result of water column conditions. The highest values occur during the B-A and Younger Dryas, suggesting that ventilation of the water column was quite strong, potentially more strongly degrading organic matter during these intervals (while Si would be relatively unaffected). This process could result in lower N preservation relative to N production during the B-A and Younger Dryas. It may also partly explain why Si:N ratios are higher during the B-A and YD interval than

the Holocene. Lower C_{org}:N ratios occur during the Holocene, suggesting better organic matter preservation in the younger samples.

Third, once material reaches the sediment-water interface, preservation of both N and Si are strongly driven by the rate of burial. The sedimentation rates at our site are known (Table S1) and the rate of burial should be the same for both N and Si at a single site. However, preservation dependency on burial rates is generally related to oxygen exposure time for organic matter (N) but related to saturation of pore waters for Si. Therefore, N and Si may have experienced differential preservation in the sediment. For Si, the saturation of pore waters creates a positive feedback on preservation, which may have further augmented Si preservation during high-productivity intervals (Ragueneau et al., 2000). At this site, the benthic oxygenation state, indicated by U_{auth} MAR, primarily follows opal productivity, meaning that opal deposition co-occurred with rapid and anoxic burial (Figure S1). This co-occurrence of opal flux and U_{auth} means that remineralization at the sediment-water interface is not likely to drive the main structure of the Si:N record, since these pressures generally co-occurred at this site during this interval.

Ultimately, Si:N ratios are a qualitative measure, and we expect the signal to be variable. Therefore, we restrict our interpretation to “low” vs. “high” Si:N values representing “transient” vs. “chronic” iron limitation. Sediment trap data often includes biogenic Si and C_{org} but does not always include N; we therefore convert Si:C ratios to Si:N ratios. The C_{org}:N ratios of marine sediments typically range from 8 to 10.5 in marine environments at this depth (1295m at present, 1165 m if sea level

was 130 m lower). The floor for transient iron limitation of 1:1 Si:C_{org} suggested by Pichevin et al., 2014 therefore equates to an 8:1 Si:N molar ratio, assuming a C_{org}:N of 8:1. A conservative regional estimate for chronic iron limitation in the region of 4:1 Si:C_{org} would then approximately equate to a Si:N of 32:1. We include a line at 32 Si:N to aid visual interpretation in Figure S3. If C_{org}:N ratios are instead at their maximum of 10.5, then the value of 32 Si:N would represent a Si:C_{org} of 3, which is still consistent with the typical North Pacific values indicating chronic iron limitation in Pichevin et al., 2014 of 3-4 mol/mol.

At U1340, all of the Si:N molar ratios in our record are >10 mol/mol (and therefore Si:C_{org} is >1). This suggests that the entire record falls into the category of transient iron limitation according to the global compilation in Pichevin et al., 2014. Near the coretop and in the mid-Holocene, Si:N molar ratios are characterized by Si:N values close to 32 mol/mol, consistent with modern observations that suggest chronic iron limitation in the region. Si:N ratios above this value, indicated by a red line in Figure S3, represent chronic iron limitation at this site. The result suggests that the Bølling-Allerød, and to a lesser extent the beginning and end of the PreBoreal, were times of particularly extreme iron-limitation. These high Si:N values are higher than the modern subarctic Pacific and within the range found in the Southern Ocean (Pichevin et al., 2014).

To our knowledge, this is the first study to directly use *N. seminae* abundances or bulk sediment Si:N ratios as HNLC indicators. Although both may be crude indicators, the occurrence of *N. seminae* generally agrees with Si:N ratios measured at

our site (Figure S4). Our comparison finds that relative abundances of *N. seminae* above 31% reflect intervals where chronic iron limitation occurred (Si:N >30 in all 12 samples). Likewise, relative abundances 16% or lower reflect intervals when iron limitation was transient (Si:N <23 in 9 of 10 samples; summer temperature <6 ℃ in the outlier). There is some ambiguity in the iron status when *N. seminae* abundances are between 16-31%, which may represent samples with high annual variability in Fe availability or may be partly due to the interpolation. Given that these % abundances are relative to the production and preservation of other diatoms, as well as the potential influence of temperature, these relative abundances may not apply to other sites.

These large changes in iron supply are reflected in the utilization of Si (i.e., our silicon isotope record). Although iron limitation increases intracellular uptake of Si relative to other nutrients, increasing Si utilization (f) (Brzezinski et al., 2003), the Si:N ratios at this site suggest that transient iron limitation always occurred at this site, meaning this elevated utilization condition may have never lifted. Furthermore, when low-iron conditions are persistent and extreme enough to induce HNLC conditions, a near-surface pool of silicic acid grows which in fact decreases the relative utilization of Si. This is exemplified by the HNLC Holocene, which is a time of excess silicic acid supply and therefore low Si utilization. We apply the same logic to the B-A in the main text.

5.2 Diatom Groups

For the purposes of this paper, all diatoms are grouped at the genus level. Some genera were only identified to genus-level; where possible, species were identified according to the taxonomy in Stroynowski et al., 2015. For the *Thalassiosira* Cleve genus, diatoms were identified to species-level only for certain important indicator species.

The group we label deep chlorophyll maximum (DCM) flora contains multiple species with similar niches, whose abundances may compensate for one another. The concept of a shade flora assemblage, which grows throughout the late summer and is deposited en masse when autumn winds mix the layer below the critical depth (coined the "fall dump,") is from (Kemp et al., 2000). This includes the genera *Rhizosolenia, Thalassiothrix,* and *Coscinodiscus.* Although the initial study region was in the temperate North Pacific, these diatoms appear to consistently indicate stably stratified late summer waters, particularly those of deep nutrient stratification, in the Bering Sea as well (Stroynowski et al., 2015, 2017; Worne et al., 2021). At our site, all *Rhizosolenia* found were *Rhizosolenia hebetata* Bailey, although its morphology differs during different intervals, which could be classified as different 'forma.' All *Thalassiothrix* observed were *Thalassiothrix longissima* Cleve & Grunow. *Cosinodiscus* were primarily *C. marginatus*, with occasional *C. radiatus* or *C. occulus-irridis*.

Nearly all of the *Actinocyclus* Ehrenberg species at our site are *Actinocyclus curvatulus* Janisch, with *Actinocyclus ochotensis* A.P. Jousé occasionally present; we therefore we chose to group all *Actinocyclus* species for simplicity. We suggest that

the co-occurrence of DCM flora with *A. curvatulus* creates a good indicator of stratified conditions.

Early work in the Bering Sea suggested that *A. curvatulus* and *Shionodiscus trifultus* (Fryxell) Alverson, Kang & Theriot always appear together, and represent cold summers (Sancetta & Robinson, 1983), however our record shows that the two genera have different patterns of abundance. This could partly be because *Shionodiscus* Alverson, Kang & Theriot species counted in this study include all *Shionodiscus oestrupii* (Ostenfeld) Alverson, Kang & Theriot and *Shionodiscus frenguelliis* (Kozlova) Alverson, Kang, & Theriot, the latter of which was sometimes common. In any case, while both *Shionodiscus* and *Actinocyclus* are associated with stably stratified surface waters (Sancetta & Robinson, 1983), the different patterns of their occurrence in our record suggest they do not necessarily flourish in the same season or environmental conditions. In a sediment trap study from Station AB, located proximally to Site U1340, *A. curvatulus* was more likely to occur from Jan-Apr while *S. trifultus* was more likely to occur from Apr-Oct (although their seasonal abundances varied greatly from year to year) (Onodera & Takahashi, 2009). Different patterns in *Actinocyclus* and *Shionodiscus* are also seen on long timescales in the Bering Sea, with various *Actinocyclus* species occurring during periods with some sea ice presence (Worne et al., 2021). The authors of that study suggest that when spring melt creates a surface layer of nutrient-depleted, well-stratified water, *Actinocyclus* species comprise the spring or summer bloom (Worne et al., 2021). This behavior has been observed in the modern Antarctic, where *A. curvatulus* was the dominant species

in a meltwater-stabilized bloom in austral summer (January) (Piquet et al. 2011), and it is often present in a similar environment in the open waters of the North Atlantic sector of the Arctic ocean (Andersen et al., 2004). We therefore consider *A. curvatulus* to represent thin near-surface stratification as well as likely indicating that sea ice was present earlier in the year.

The *Chaetoceros* Ehrenberg group was only counted at the genus level, because most occur as resting spores which are not distinguishable to the species level. Vegetative cells are also included in this group. This genus can occur in coastal open-ocean, or ice-edge settings when there is upwelling and high nutrient supply, including major nutrients and iron (Fatima Abrantes, 1988; J. Ren et al., 2014).

The group of sea-ice or marginal-ice related flora is the most complex and composed of the greatest number of species. The included species may indicate thick pack ice, marginal ice, ice melt layers, or open polynyas surrounded by sea ice. The species included are: *Fragilariopsis cylindrus* (Grunow ex Cleve) Helmcke & Krieger*, Thalassiosira antarctica* Comber*, Thalassiosira gravida Cleve, Thalassiosira hyalina* (Grunow) Gran*,* and *Thalassiosira nordenskioeldii* Cleve*, Odontella aurita* (Lyngbye) Agardh*,* and *Stellarima stellaris* (Roper) Hasle & Sims. We explain the inclusion of each species below. Most species in the sea-ice flora group generally bloom in early spring, but depending on the timing of sea ice melt, which may have varied throughout the timescale of our record, the timing of that bloom may have occurred in different months of the year (Fujiwara et al., 2016).

F. cylindrus is a canonical sea-ice indicator; however, recent work suggests it also flourishes in open waters surrounded by sea ice, and therefore is better thought of as an indicator "polar waters" and near-zero-degree temperatures (von Quillfeldt, 2004).

T. antarctica is a well-established indicator of pack-ice (thick, multi-year ice) (Stroynowski et al., 2017; Worne et al., 2021). This species mostly occurs in our record as resting spores but vegetative cells are occasionally present during the laminated intervals, possibly due to better preservation. There is generally little productivity at our site in meteoric winter due to low incident light, but *T. antarctica* can grow in-ice and may be associated with autumn sea-ice blooms (Pike et al., 2009) as well as possibly being the only diatom robust enough to comprise any winter, spring or summer bloom if there is sea ice cover throughout the year (Stroynowski et al., 2017). When co-occurring with other *Thalassiosira* species that are indicative of spring ice melt, *T. antarctica* may also indicate meltwater blooms (Krawczyk et al., 2012).

T. gravida, *T. hyalina*, and *T. nordenskioeldii* are often grouped together because all are associated with waters near sea-ice margins, and are associated with high productivity in the cold, low-salinity melt waters immediately following the breakup of seasonal sea ice (Andersen et al., 2004; Barron et al., 2009; Sancetta & Robinson, 1983). *Odontella aurita* and *Stellarima stellaris* are likewise associated with marginal sea-ice (Worne et al., 2021). Both occur with the other marginal ice species but are usually not common (always <10%, usually <5% of the assemblage).

Shionodiscus species include *S. trifultus, S. oestrupii* and *S. frenguellii*, which we group together as the genus *Shionodiscus* in our counts. These are always common in the record (10%-30%).

A final group of diatoms, not discussed in the main text, represents shallow shelf environments and thus their occurrence at our open-ocean site represents transport from shallower areas, likely due to sea ice movement. These are: *Paralia sulcata* (Ehrenberg) Cleve, *Eupyxidicula turris* (Greville) Blanco & Wetzel) and *Asteromphalus* Ehrenberg species. (Barron et al., 2009; McQuoid & Nordberg, 2003; Stroynowski et al., 2017). While these diatoms are individually rare (<5% of the assemblage), they appear to occur together, at slightly higher abundances, at the LGM, at 16.5 ka, and in the late Younger Dryas. Although in sum they are <7% of the total abundances at these times, the timing of these recurrences may indicate some aspect of LGM-like ocean circulation or ice transport.

The cosmopolitan diatom *Thalassionema nitzschioides* (Grunow) Mereschkowsky was present in every sample but never at abundances more than 5%. The following diatoms occurred only uncommonly or rarely in our record and are not included in any of the groups above: *Azpeitia tabularis* (Grunow) Fryxell & Sims; *Fossulaphycus arcticus* Blanco; *Cocconeis* Ehrenberg species; *Delpheneis* Andrews species; occasional *Fragilariopsis* Hustedt species and several *Thalassiosira* species not listed above, which we report as a group.

Acknowledgements

Chapter 1, in full, is a preprint of the material as it will likely appear in Geophysical Research Letters, where it is currently in review. K. A. deLong, T. Blackburn, B. Caissie, J. Addison, Z. Stroynowski, M. R. Sipala, F. Marcantonio, and A. C. Ravelo, Geophysical Research Letters, 2024. The dissertation author was the primary investigator and author of this paper.

Chapter 2 AMINO ACID PALEO-PROXIES REVEAL NITROGEN AND TROPHIC DYNAMICS IN THE DEGLACIATING SUBARCTIC PACIFIC

1 Introduction

The availability of nitrogen exerts a first-order control on marine production and carbon sequestration in most marine ecosystems; the cycling of nitrogen in the marine environment is therefore an important link between ecosystems and global climate. Predicting how marine N cycling may change in response to a future climate disruption can be aided by studying past analogous events, such as the abrupt Bolling-Allerod warm event which occurred during the recent deglaciation. The marine sedimentary record is a major archive of past environmental change, but quantifying marine N cycling is challenging due the complexity of extracting and interpreting nitrogen from sedimentary archives and our incomplete knowledge of nitrogen dynamics on geologic timescales.

In marine settings, the annually-integrated $\delta^{15}N$ of sinking particulate organic nitrogen (PON) reflects nitrate utilization in the surface (Altabet & Francois, 1994; Sigman et al., 2000). To reconstruct past N utilization, one common approach is to measure the $\delta^{15}N$ of bulk sediments, appealing because it requires minimal sample processing and is relatively quick to measure (Robinson et al., 2012). However, interpretation of sedimentary $\delta^{15}N_{bulk}$ measurements are rarely straightforward as many heterogeneous N compounds are potentially present, each with its own history of production, degradation, and preservation (Robinson et al., 2012). More refined $\delta^{15}N$ proxies have thus been developed in recent years for use in paleo-studies,

including measuring $\delta^{15}N$ in fossil tests such as diatom-bound and foraminifera-bound $\delta^{15}N$ (Robinson et al., 2023 and refs therein), and measuring compound-specific isotopes of amino acids (CSI-AA) preserved in sedimentary archives. CSI-AA, like fossil-bound approaches, circumvents many of the problems associated with bulk analysis because it removes the issue of unknown N in mixtures, and isotope values of individual compound patterns can be examined to assess if significant alteration has occurred. While CSI-AA data in sediments is not yet extensive, AA high deposition environments have been show to retain the original isotopic signatures in forms relatively protected from diagenesis (Batista et al., 2014; Shen et al., 2021). Fossil-bound studies often further isolate certain species or size classes of organisms, which may be necessary given potentially large species-specific offsets (e.g., Dove et al., 2023; Studer et al., 2013). One advantage to using bulk-sediment CSI-AA is that it relies on ecosystem-wide signatures that are not affected by phytoplankton species composition (Batista et al., 2014). While this ecosystem-wide integration is a strength of the CSI-AA approach, it requires an appropriate interpretive framework, based on a clear understanding of how N cycling in planktonic ecosystems impacts amino acid isotope values.

CSI-AA has been applied as a paleoceanographic proxy in a growing number of investigations; however, the systematics of amino acids on long timescales (e.g., decadally integrated timescales or greater) have not been fully described, leading to ambiguity in the correct interpretive framework. In particular, it is not known if the framework commonly used in ecology (e.g., Chikaraishi et al., 2009; McMahon &

McCarthy, 2016), which was developed and tested for the most part in individual organisms, also applies to paleoarchives. One major issue is the impact of nitrogen recycling between producers, consumers, and microbes in the planktonic ecosystem on various timescales (Batista et al., 2014; Smart et al., 2020; Yoshikawa et al., 2022). CSI-AA was originally developed for use in modern ecology, primarily to study instantaneous trophic dynamics (e.g., Chikaraishi et al., 2009). These studies build on the ecological principle that an individual organism can be assigned a Trophic Position (TP). Primary producers are assigned a TP of 1; subsequent metabolism enriches the $\delta^{15}N$ of the organism's amino acids (AAs). In this framework, the $\delta^{15}N$ of "source" amino acids are slightly enriched (e.g., by 0.4‰) with each trophic transfer, while the $\delta^{15}N$ of "trophic" amino acids are greatly enriched (e.g., by 6.6‰) with each trophic transfer (Chikaraishi et al., 2014; Ohkouchi et al., 2017). Thus, an organism's TP can be quantified by measuring the difference between the $\delta^{15}N_{SourceAAs}$ and $\delta^{15}N_{TrophicAAs}$ and using known discrimination factors to estimate the number of trophic transfers that have occurred. Extending this traditional TP paradigm to marine sediments, a bulk-community TP of 1 should be found where there is pure algal deposition; where consumers (zooplankton) contribute to the total N in sediment, we would expect their contribution to greatly enrich $\delta^{15}N_{TrophicAAs}$ with a near-negligible effect on $\delta^{15}N_{SourceAAs}$. If $\delta^{15}N_{SourceAAs}$ and $\delta^{15}N_{TrophicAAs}$ are independent variables, as is typically assumed in ecology, then $\delta^{15}N_{SourceAAs}$ would continue to track $\delta^{15}N$ of primary production (also called $\delta^{15}N_{baseline}$), while the difference between sedimentary

$\delta^{15}N_{SourceAAs}$ and $\delta^{15}N_{TrophicAAs}$ would reflect the average trophic position of the planktonic community. From this, it follows that $\delta^{15}N_{SourceAAs}$ would accurately represent the average value of local surface dissolved inorganic nitrate/ite $\delta^{15}N$ ($\delta^{15}N_{DIN}$), at least to the same extent that phytoplankton $\delta^{15}N$ does (Choi et al., 2023; Sherwood et al., 2014; Ohkouchi et al., 2017). That is, the effects of regional utilization, denitrification, nitrogen fixation, etc. would be incorporated into the phytoplankton $\delta^{15}N$ signature.

However, one foundational study of CSI-AA in sediments found a large caveat to these assumptions based on long-term isotopic mass balance (Batista et al., 2014). The mass-balance hypothesis proposed by these authors suggested that where there is complete N utilization, $\delta^{15}N_{SourceAAs}$ (i.e., 'baseline' signatures) must become depleted with increases in TP of the planktonic community. This is because, in a closed system with a fixed pool of heavy and light isotopes, enrichment of $\delta^{15}N_{TrophicAAs}$ cannot continue *ad infinitum* with increasing TP; instead, some of the N in the system must be depleted in order to enrich $\delta^{15}N_{Trophic}$ values, resulting in *lower* $\delta^{15}N_{SourceAAs}$ values with higher ecosystem TP (Batista et al., 2014). If this interpretive framework applies to all integrated-timescale records, such as sedimentary records, then using $\delta^{15}N_{SourceAAs}$ as a proxy for surface $\delta^{15}N_{DIN}$ would be misleading; instead, the more accurate recorder of surface changes would be the total sum of all particulate organic nitrogen ($\delta^{15}N_{PON}$) (Batista et al., 2014). In sediments, the $\delta^{15}N_{PON}$ can be approximated by summing the $\delta^{15}N$ from all measured amino acids, termed THAA (Total Hydrolysable Amino Acids); the study therefore

suggested $\delta^{15}N_{THAA}$ be used in sedimentary records to track changes in $\delta^{15}N_{DIN}$ wherever N is fully utilized (Batista et al., 2014). That study was conducted in the Santa Barbara Basin, which experiences complete N utilization and can be considered a closed system due to the relative isolation of surface waters, which may have made that study unique, since much of the ocean is never a fully closed system; furthermore, the limited scope of this single study could not determine on what timescales or by what mechanism this mass-balance occurred. Therefore, subsequent paleo-investigations have rarely taken the mass-balance hypothesis into account (e.g., Golombek et al., 2024; Li et al., 2019). If community recycling does deplete $\delta^{15}N_{SourceAAs}$, then an inverse relationship between TP and $\delta^{15}N_{SourceAAs}$ should be widespread, because nitrogen utilization is complete in most marine environments. Before oceanographic conclusions such as changes in $\delta^{15}N_{DIN}$ can be inferred from a CSI-AA record, it is essential that the dynamics of amino acid cycling on long timescales are understood.

To test the mass-balance hypothesis and to investigate changes in the marine nitrogen cycle on geologic timescales, we generated CSI-AA from Site U1340 in the Bering Sea across the recent deglaciation. This site is known to have undergone extreme oceanographic changes during the period of our investigation, including large changes in productivity, water column structure, and nutrient dynamics (DeLong et al., 2024; Schlung et al., 2013). These large oceanographic changes are accompanied by changes in TP, and thus serve as natural experiments to test the mass-balance hypothesis and to assess what approach best captures changes in

surface $\delta^{15}N_{DIN}$ in sedimentary archives. In addition, conflicting diatom- and foraminifera-bound records in the region have left the role of nitrogen utilization through the deglaciation unclear (Ren et al., 2015), which CSI-AA can address in a new way. In the new record presented here, periods of high TP are indeed correlated to depleted $\delta^{15}N_{SourceAA}$ values, suggesting N recycling drives baseline $\delta^{15}N$ depletion in some or all oceanographic conditions, highlighting the need for future investigations of nitrogen $\delta^{15}N$ partitioning in marine communities. Here we show that after accounting for the influence of recycling on CSI-AA proxies, large changes remain in our $\delta^{15}N_{SourceAAs}$ and $\delta^{15}N_{THAA}$ records, suggesting that large changes in $\delta^{15}N_{DIN}$ must have occurred during the deglaciation, consistent with introduction of a new nitrate source during the Bolling-Allerod. Finally, we compare our CSI-AA records to nearby diatom-bound and foraminifera-bound $\delta^{15}N$ records and confirm that diatom-bound $\delta^{15}N$ and $\delta^{15}N_{SourceAAs}$ appear to record similar signals of baseline $\delta^{15}N$, while foraminifera-bound $\delta^{15}N$ and $\delta^{15}N_{THAA}$ are records of particulate organic nitrogen $\delta^{15}N$.

2 Materials and Methods

2.1 CSI-AA Chemical Analysis

CSI-AA for $\delta^{15}N$ were generated from bulk sediment samples which were freeze-dried, pulverized by mortar and pestle and homogenized. Approximately 400-600 mg of sample was hydrolyzed under standard conditions (6 N HCl for 20 hours at 110°C) and isopropyl-TFA derivatives were prepared based on the method of (Silfer et al., 1991). Derivatized samples were analyzed on a Thermo Trace Ultra gas

chromatograph coupled to a Thermo-Finnigan Delta Plus XP isotope ratio mass spectrometer. Amino acids were separated for $\delta^{15}N$ analyses using a BPX5 column (60 m×0.32 mm, 1 μm film thickness; SGE Analytical Science, Trajan, Austin, TX, USA).

2.2 Calculated Values

The calculated value Total Hydrolysable Amino Acids (THAA) is the average $\delta^{15}N$ value for all recovered amino acids, mass-weighted by molar percent abundance. The ΣV is the sum of the variance around the Average Trophic $\delta^{15}N$ value as described in McCarthy et al., 2007. The Degradation Index (DI) is calculated from Dauwe et al., 1999 with only the subset of amino acids that were recovered.

To calculate Trophic Position (TP), i.e., the average trophic position of the planktonic ecosystem, we use the following equation from (Golombek et al., 2024):

$$TP = ((\delta^{15}N_{Trophic} - \delta^{15}N_{Source} - \beta) / TDF) + 1$$

This equation uses the average $\delta^{15}N$ of all recovered trophic amino acids (Glu, Ala, Val, Asp, Ile, Leu, Pro), unweighted, for the $\delta^{15}N_{Trophic}$ value, and likewise, the average of Phe and Lys, unweighted, for the $\delta^{15}N_{Source}$ value (Golombek et al., 2024). By using a TP equation that is a composite for multiple AAs, it includes the important information encoded in $\delta^{15}N_{Ala}$ enrichment (Moira Décima et al., 2017) and smooths inter-sample variability that may result from diagenesis (Golombek et al., 2024) or that may be purely analytical in nature. In our samples, recovery of $\delta^{15}N$ of Glu was analytically inconsistent due to the co-elution of an unknown compound which

caused a small shoulder peak in most samples, resulting in a high degree of variance of $\delta^{15}N_{Glu}$ compared to the other $\delta^{15}N_{Trophic}$ values.

The β parameter represents the offset of trophic values from Phe in marine autotrophs; we use 2.9 (Golombek et al., 2024). Uncertainty in β introduces the largest uncertainty to the TP calculation; a recent review found β values may vary more than previously appreciated, estimating uncertainty to be ± 1.3 for Phe and ± 2.6 for Lys in marine ecosystems with eukaryotes (1-σ uncertainties, Ramirez et al., 2021). If ecosystem shifts caused significant and sustained shifts in β, it might be indistinguishable from a change in TP in our calculation. For the trophic discrimination factor parameter (TDF), we use 6.6, derived from a meta-analysis (Nielsen et al., 2015). The exact TDF for each amino acid varies from organism to organism, but in natural marine environments and on integrated timescales, uncertainty in TDFs may be negligible (Landry & Décima, 2017). Thus, the exact TP values would vary if a different TDF was used, but trends would remain the same.

2.3 Application of Batista Model

The Batista model's inputs are measured $\delta^{15}N_{THAA}$ and TP (Batista et al., 2014). It partitions the N isotopes among the included amino acids assuming complete utilization and mass-balance. For the purposes of our investigation, we only focus on the $\delta^{15}N_{Phe}$ output. The model predicts that all data will fall on a single TP-Phe line if $\delta^{15}N_{DIN}$ is unchanging and only trophic structure, as measured by TP, controls the $\delta^{15}N_{Phe}$ values. In that study, the authors used the site's average $\delta^{15}N_{THAA}$ as a single input. In our longer timescale record, using a single input for $\delta^{15}N_{DIN}$

throughout is unlikely to be correct, as the $\delta^{15}N_{THAA}$ varies considerably through time (ranging from 8.8 - 14.2‰). Instead, we use the measured $\delta^{15}N_{THAA}$ and TP of each sample to calculate the predicted $\delta^{15}N_{Phe}$ for each point separately (Figure 3b). This allows $\delta^{15}N_{DIN}$ ($\delta^{15}N_{THAA}$) to vary through time.

We also use the model in a new way: instead of inputting $\delta^{15}N_{DIN}$ and TP to predict $\delta^{15}N_{Phe}$, we input our measured $\delta^{15}N_{Phe}$ and TP to calculate $\delta^{15}N_{DIN}$. To isolate only the variability associated with community TP in the Batista model (and exclude the variability inherent in changing $\delta^{15}N_{DIN}$), we input a constant $\delta^{15}N_{THAA}$ to the model; it then predicts $\delta^{15}N_{Phe}$ as a linear function of TP using the following equation:

$$\delta^{15}N_{Phe} = m * (TP - 1) + b$$

where m is -2.187 and b represents the value of the prediction where TP=1. In this case, b represents $\delta^{15}N_{SurfaceN}$, because it is what the value of $\delta^{15}N_{Phe}$ would be if there was no effect of ecosystem trophic structure on $\delta^{15}N_{Phe}$. Rearranging the equation to solve for $\delta^{15}N_{SurfaceN}$ gives the following equation:

$$\delta^{15}N_{SurfaceN} = \delta^{15}N_{Phe} - m * (TP - 1)$$

Based on the input TP values, which range from 1.02 – 1.81, the magnitude of the Phe-depletion ranges from 0.05‰ to 1.77‰ compared to the $\delta^{15}N_{SurfaceN}$ values.

3 Background: Oceanographic and Paleoclimate Setting

3.1. Oceanographic Setting

Site U1340 (53°24 N, 179°31 W, 1295 m) is located on the Bower's Ridge in the Bering Sea, a marginal sea of the Subarctic Pacific (Figure 1). The Subarctic Pacific is a high-nutrient, low-chlorophyll (HNLC) region where iron limitation

causes high near-surface nitrate concentrations (Figure 1, Aguilar-Islas et al., 2007; Gouretski & Koltermann, 2004; Zhu et al., 2021), which may give rise to unique nitrogen cycle dynamics such as incomplete nitrate utilization and a high degree of ammonium-fueled primary production (Yoshikawa et al., 2018, 2022). This subpolar, open-ocean, HNLC location is a contrast to the temperate Santa Barbara Basin where the foundational study for CSI-AA in sediments took place, which typically experiences near-complete N utilization (Batista et al., 2014). Across the timescale of our study from 19 ka - 5 ka, intervals of both incomplete utilization (Fe-limitation) and complete N utilization (N-limitation) are expected to occur at this location (DeLong et al., 2024; H. Ren et al., 2015) as the region experienced intervals of rapid environmental change.

In the modern ocean, the typical $\delta^{15}N_{Nitrate}$ signature supplied to our site is ~6.5‰, estimated from values which fall between 5.5–7.5‰ in the region from 200-500 m depths (Yoshikawa et al., 2018, 2022; Zhu et al., 2021). This regional $\delta^{15}N_{Nitrate}$ signature is exported from the nearby Bering Shelf, which experiences rapid N utilization (Zhu et al., 2021). Nitrate with this $\delta^{15}N$ signature is supplied to the Subarctic North Pacific by mixing in winter; subsequent spring and summer production causes near-surface $\delta^{15}N_{Nitrate}$ to rise to ~10–12‰ due to utilization (Yoshikawa et al., 2022; Zhu et al., 2021). Annual nitrogen utilization is incomplete, with as little as 30% of available nitrate used by mid-summer in the core of HNLC conditions (Yoshikawa et al., 2018; Zhu et al., 2021). In the nearby Gulf of Alaska, where a higher fraction of nitrate is consumed in summer, surface $\delta^{15}N_{Nitrate}$ values

have been measured as high as 21‰ (corresponding to ~85% utilization) (Yoshikawa et al., 2018). If N utilization were complete, then sinking PON should be equal to the nitrate supply (~6.5‰). Instead, sinking particulate organic nitrogen (PON) in the region appears to reflect incomplete utilization, varying from ~2.6‰ in the core of HNLC conditions to ~4.9‰ in the Gulf of Alaska (Yoshikawa et al., 2018).

In addition to iron limitation, incomplete annual nitrate consumption may also be attributed to high ammonium availability (Yoshikawa et al., 2022; Zhu et al., 2021). Based on the fraction of nitrate consumption alone, and using an isotope effect (ε) of -5‰, $\delta^{15}N_{phytoplankton}$ would be expected to be around 2-3‰ at our site and in the SNP region (Matsubayashi et al., 2020). Measured values of surface $\delta^{15}N_{PON}$ instead range from -2 to +2‰, i.e. mostly lower than expected from nitrate utilization, attributed to the prevalence of ammonium uptake (Mino et al., 2016; Zhu et al., 2021). A study reconstructing $\delta^{15}N_{phytoplankton}$ (also called $\delta^{15}N_{baseline}$) from copepod $\delta^{15}N_{AAs}$ estimated $\delta^{15}N_{Phe}$ to be also between -2 and +2‰ throughout the SNP and southern Bering Sea (Matsubayashi et al., 2020), confirming that $\delta^{15}N_{SourceAA}$ signatures accurately reflect $\delta^{15}N_{PON}$ and that these signatures are carried into higher trophic levels.

Despite the potential influence of ammonium dynamics on $\delta^{15}N_{phytoplankton}$ values, estimates of exported $\delta^{15}N_{PON}$ to sediment traps and coretops in the subarctic Pacific are often between 2.5–5.5‰ and are thought to reflect nitrate dynamics alone (i.e., the $\delta^{15}N_{Nitrate}$ supply signature and its incomplete utilization) (Brunelle et al., 2010; Wojtal et al., 2023). In the Bering Sea, $\delta^{15}N_{Bulk\text{-}PON}$ at 500 m depth is ~6‰ (Zhu

et al., 2021); the near-coretop $\delta^{15}N_{Bulk\text{-}sediment}$ value at site U1340 is 4.6‰, a value consistent with the above described regional nitrate dynamics (Schlung et al., 2013). This may be because there are higher-frequency processes that reflect, for example, ammonium use or degradation effects, but these are smoothed in an annual average (or centennial average, in the case of sediment core tops), leaving a mean signal that primarily reflects the $\delta^{15}N_{Nitrate}$ supply signature and its incomplete utilization. For example, At Station K2 at the southwestern edge of the subarctic North Pacific (Figure 1), surface $\delta^{15}N_{Bulk\text{-}PON}$ values ranged from -0.2–3.5‰, while 1000-m depth sediment trap $\delta^{15}N_{Bulk\text{-}PON}$ values ranged from 1.7-5.1‰ (Mino et al., 2016; Yoshikawa et al., 2022). This may be because surface PON was dominated by small, <6 um particles, which were more likely to have low $\delta^{15}N$, and given slower sinking speeds these small particles were more fully remineralized in the water column; in contrast, sediment trap material tends to be dominated by the signatures of large (>51 um) particles, which sink and are buried more efficiently with minimal $\delta^{15}N$ changes during sinking (Wojtal et al., 2023).

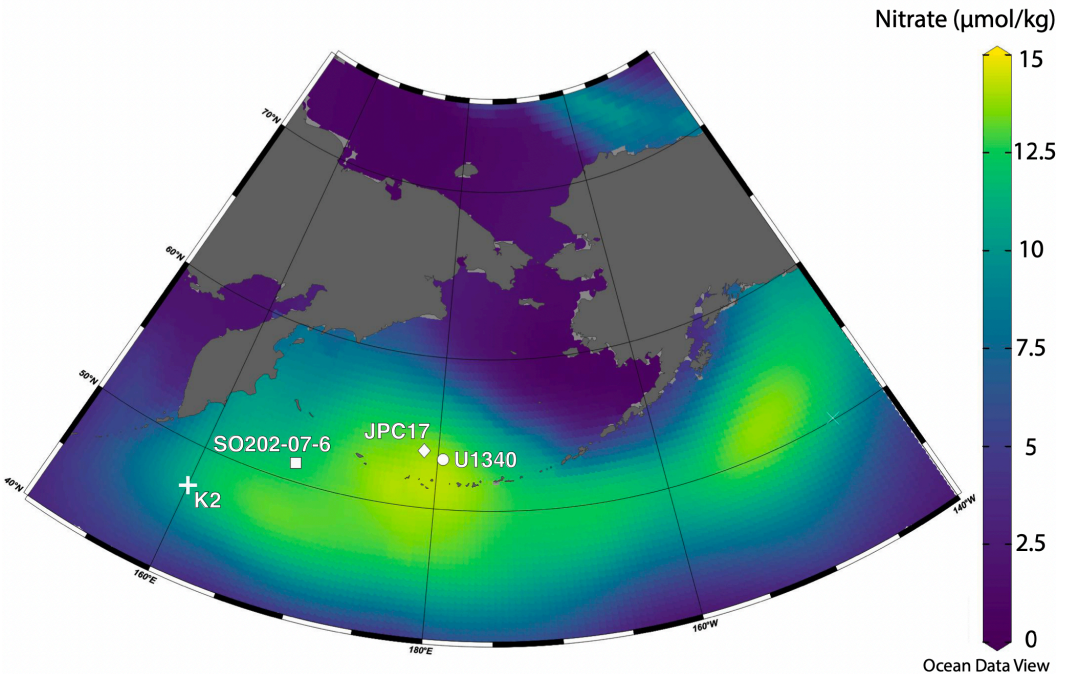

Figure 2.1: Map of core sites and surface nitrate concentration. Average annual surface nitrate (µmol/kg) shows underutilized nitrate, indicating HNLC conditions. Core sites shown include U1340 (this study), JPC17 (diatom-bound $\delta^{15}N$), SO202-07-6 (diatom-bound $\delta^{15}N$ and foraminifera-bound $\delta^{15}N$), and Station K2.

Trophic Position (TP) in marine particles can vary from 1.0, representing 100% primary production, to >2.5 in oligotrophic oceans (McMahon et al., 2015; Shen et al., 2021; Sherwood et al., 2014). TP can also vary from 1.0 - 2.0 in a single location, e.g., seasonally during a spring bloom vs. autumn production; or interannually during El Nino vs. non-El Nino years (Choi et al., 2023; Shen et al., 2021). TP values represent the average trophic chain length of the ecosystem, and also reflect the relative ratio of primary production vs. zooplankton export to sinking organic matter (Chavez et al., 2011; M Décima, 2022; Doherty et al., 2021). These values are set by the planktonic community and are not thought to reflect changes in the nekton (McCarthy et al., 2007). In sediments, the TP signal is derived from particle export (PON) and thus naturally integrates across large spatial and temporal

scales. Sediment trap studies suggest TP estimates from PON vary with water column depth, driven by preferential remineralization of smaller particles at shallower depths, similar to bulk $\delta^{15}N_{PON}$; and may also be influenced by the addition of bacterial biomass in sinking particles (Wojtal et al., 2023; Yoshikawa et al., 2022).

To our knowledge there are no modern estimates for TP in the Bering Sea, but it may be similar to estimates from sediment traps at K2, which ranged from 1.6-2.2 in 1000-m depth sediment traps (Yoshikawa et al., 2022). Similar TP values were found at mesopelagic depths (300-500 m) at Station Papa (Wojtal et al., 2023); however, it may be important to compare TP estimates from similar depths due to sinking particle dynamics.

3.1. Oceanographic Setting

Our study covers the last deglaciation from 6-19 ka; several millennial-scale events with large environmental changes occurred in the subarctic Pacific across this timescale. The Last Glacial Maximum (LGM; 19-22 ka) was an interval with low primary productivity, seasonal or perennial sea ice, and a highly stratified water column; both surface and intermediate waters were likely low in nutrients, particularly nitrogen, which may have created conditions of complete nitrate consumption (DeLong et al., 2024; H. Ren et al., 2015; Schlung et al., 2013). LGM-like conditions generally continued throughout the early deglaciation (16-19 ka) and Oldest Dryas (14.8-16 ka). The Bolling-Allerod (B-A; 14.7-12.9 ka) and PreBoreal (PB; 11.7-10.5 ka) were intervals of significant warming in the northern hemisphere, and are marked by high productivity (opal flux) and hypoxic deposition throughout

the subarctic Pacific (Kuehn et al., 2014). One hypothesis suggests this high productivity was caused by a large increase in macronutrient availability supplied from the upwelling of nutrient-rich Deep Pacific Water; increased macronutrient availability may have induced HNLC conditions (DeLong 2024). The Younger Dryas cold event (YD; 12.9 - 11.8 ka) occurs between the B-A and the PB; productivity during this event remained moderately high but sedimentation was oxic. Following the PB, the record represents the transition into the Holocene (0-10 ka). The near-coretop value, dated to ~6 ka, represents conditions similar to the modern ocean, with moderately high productivity and HNLC waters (DeLong 2024).

4 Results

The AA $\delta^{15}N$ data shows a typical marine organic matter pattern when normalized to Phe, indicating good preservation of AA isotopic values in the Bering Sea sediments back to ~19 ka (SI Table 1, SI Fig. 1). Applying the framework of Golombek et al., 2024, the Ala-Phe vs. Thr-Phe values indicate the samples are a mix of fecal pellet and phytoplankton sources, with a few samples more similar to degraded organic matter (SI Fig. 2). The ΣV values range from 1.5 - 3.1, indicating degradation varied significantly from sample to sample (SI Fig. 2). The degradation parameters ΣV, the degradation index (DI), and % Gly do not agree for every sample but generally show more degradation during the LGM and early deglaciation, and less degradation (better preservation) during the B-A laminations. A correlation matrix suggests these degradation parameters have the highest correlation with authigenic uranium concentration, which is indicative of benthic deoxygenation. This confirms

that oxygenation of the sediments is an important control on degradation (e.g., Hartnett et al., 1998) (SI Section 2, SI Fig. 3).

The $\delta^{15}N$ of the two source AAs measured, Phe and Lys, correlate well with an overall slope of 1.0, suggesting both are similarly preserved, and so are reliable as source amino acids in these sediments (SI Fig. 4). Samples where Lys and Phe are identical within analytical error occur during the B-A and PB periods, coinciding with high opal flux, high authigenic uranium and laminated sedimentation, and lower degradation (SI Fig. 2). $\delta^{15}N_{Lys}$ values change more widely than $\delta^{15}N_{Phe}$ with a range of 7.5‰ vs. a range of 5.3‰, meaning the behavior of Lys more strongly drives the shape of the TP record. The direction of change is the same for both in most, but not all, samples.

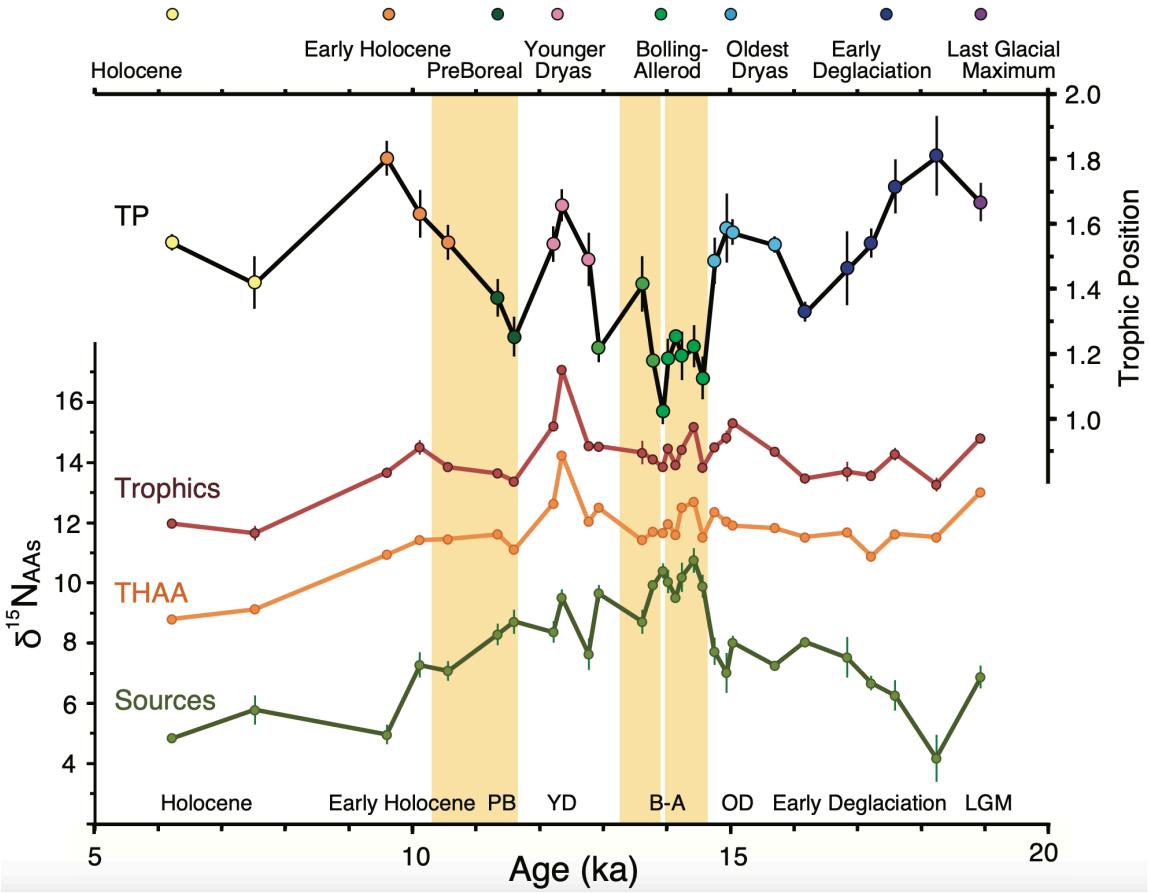

Figure 2.2: Amino Acid Results. (a) Trophic Position. (b) Average Trophic AAs ($\delta^{15}N_{Tr}$), red; $\delta^{15}N_{THAA}$, orange; Average Source AAs ($\delta^{15}N_{Src}$), green. Yellow bars represent the presence of sedimentary laminations at this site, i.e., hypoxic to anoxic sedimentation, which occur during the high-productivity PreBoreal and Bolling-Allerod intervals.

Our source AA record ($\delta^{15}N_{Src}$) is the unweighted average of $\delta^{15}N_{Phe}$ and $\delta^{15}N_{Lys}$. While specific values of $\delta^{15}N_{Src}$ cannot be considered direct recorders of $\delta^{15}N_{DIN}$ values, their trends indicate shifts in "baseline" $\delta^{15}N$, that is, the $\delta^{15}N$ of primary production. The $\delta^{15}N_{Src}$ rises through the first half of the deglaciation (19-14 ka) from ~6.0 to 11.5‰, reaching a peak during the mid-B-A. Values fluctuate in the Allerod and are high at the onset of the YD, then fall through the YD and PB from 11.0‰ to a minimum of ~5.5‰ in the Holocene.

The average value of all measured trophic AAs ($\delta^{15}N_{Tr}$) remains fairly stable between 13.3-15.3‰ for the majority of the record from 19-12.5 ka. In the mid-YD, it briefly rises to a maximum of 17.1‰. Following this peak there is a decrease back to stable levels between 13.4-14.1‰ during the PB, and then a gradual decrease to a minimum of 11.7‰ in the Holocene. Superimposed on this general shape, there are small coherent increases and decreases in $\delta^{15}N_{Tr}$ contribute to TP changes between 16.2-14.6 ka.

The $\delta^{15}N_{THAA}$ record (a proxy for average $d^{15}N$ values of all proteinaceous material) ranges from 8.8 - 14.2‰. For the most part, the shape of the $\delta^{15}N_{THAA}$ record echoes the general shape of the $\delta^{15}N_{Tr}$ record described above; the exception is that the earliest samples around 19 ka show higher values than the rest of the early deglaciation. Notably, $\delta^{15}N_{THAA}$ shows almost no changes at the B-A initiation.

TP at this site varies between 1.0 and 1.8 and shows coherent changes with climate intervals (Figure 2). The near-coretop value, dated to ~6 ka, is 1.54 ± 0.1, near the low end of modern estimates for the region (Wojtal et al., 2023; Yoshikawa et al., 2022); similar values also occur throughout the record. The highest values (>1.6) occur from 17.5 - 19 ka, at one mid-Younger Dryas point, and at one point in the Early Holocene ~9.6 ka. Lower values (1.0-1.3) occur during the B-A and PB; these values are lower than have been measured in exported particles in the region (Wojtal et al., 2023; Yoshikawa et al., 2022). The lowest value (1.0) occurs during a pause in the sedimentary laminations, a time period is known as the Older Dryas, but to avoid confusion with the Oldest Dryas, we will label and refer to it as the mid-B-A.

5 Discussion

5.1 CSI-AA Systematics and the Mass-balance Hypothesis.

One goal of this investigation is testing the CSI-AA mass-balance hypothesis, which suggests that under conditions of complete N utilization and in systems under the constraints of mass balance, increasing TP of the planktonic ecosystem will systematically deplete $\delta^{15}N_{SourceAAs}$ relative to $\delta^{15}N_{DIN}$, resulting in an inverse relationship between TP and $\delta^{15}N_{Phe}$ (Batista et al., 2014). As a result of this mass-balance, the authors suggested $\delta^{15}N_{DIN}$ changes through time would more accurately be captured by $\delta^{15}N_{THAA}$ than by $\delta^{15}N_{Phe}$ (Batista et al., 2014). Essentially, this hypothesis argues that the average bulk $\delta^{15}N$ of particulate organic nitrogen ($\delta^{15}N_{PON}$, or the proxy $\delta^{15}N_{THAA}$) is a better record for past $\delta^{15}N_{DIN}$ changes than $\delta^{15}N_{\textit{Phytoplankton}}$ ($\delta^{15}N_{Baseline}$ or $\delta^{15}N_{Phe}$). However, this hypothesis was originally proposed based on a single sedimentary record from the California margin, and has never been investigated in a region where complete N utilization may not occur. To test this hypothesis, we plot $\delta^{15}N_{Phe}$ vs. TP alongside the predicted values from the Batista model (Figure 3).

The Batista model can be used to generate "predicted" $\delta^{15}N_{Phe}$ values based on the inputs TP and $\delta^{15}N_{THAA}$. The model's starting assumption is that the $\delta^{15}N_{THAA}$ input is equal to the total $\delta^{15}N_{DIN}$; it then uses accepted TDFs to partition the N isotopes, assuming complete utilization and mass-balance. As a visual guide, we plot the model's TP-Phe relationship in Figure 3a and 3b for three points: (1) the lowest measured $\delta^{15}N_{THAA}$ (8.80‰, near-coretop), (2) the highest measured $\delta^{15}N_{THAA}$

(14.25‰, mid-Younger Dryas), and (3) the midpoint between the high and low values (11.52‰), approximately the average $\delta^{15}N_{THAA}$ for the mid-deglaciation (dashed blue lines in Figure 3a and 3b). Figure 3a shows the model-predicted $\delta^{15}N_{Phe}$; Figure 3b shows the measured $\delta^{15}N_{Phe}$ data; and Figure 3c shows the data-model $\delta^{15}N_{Phe}$ comparison.

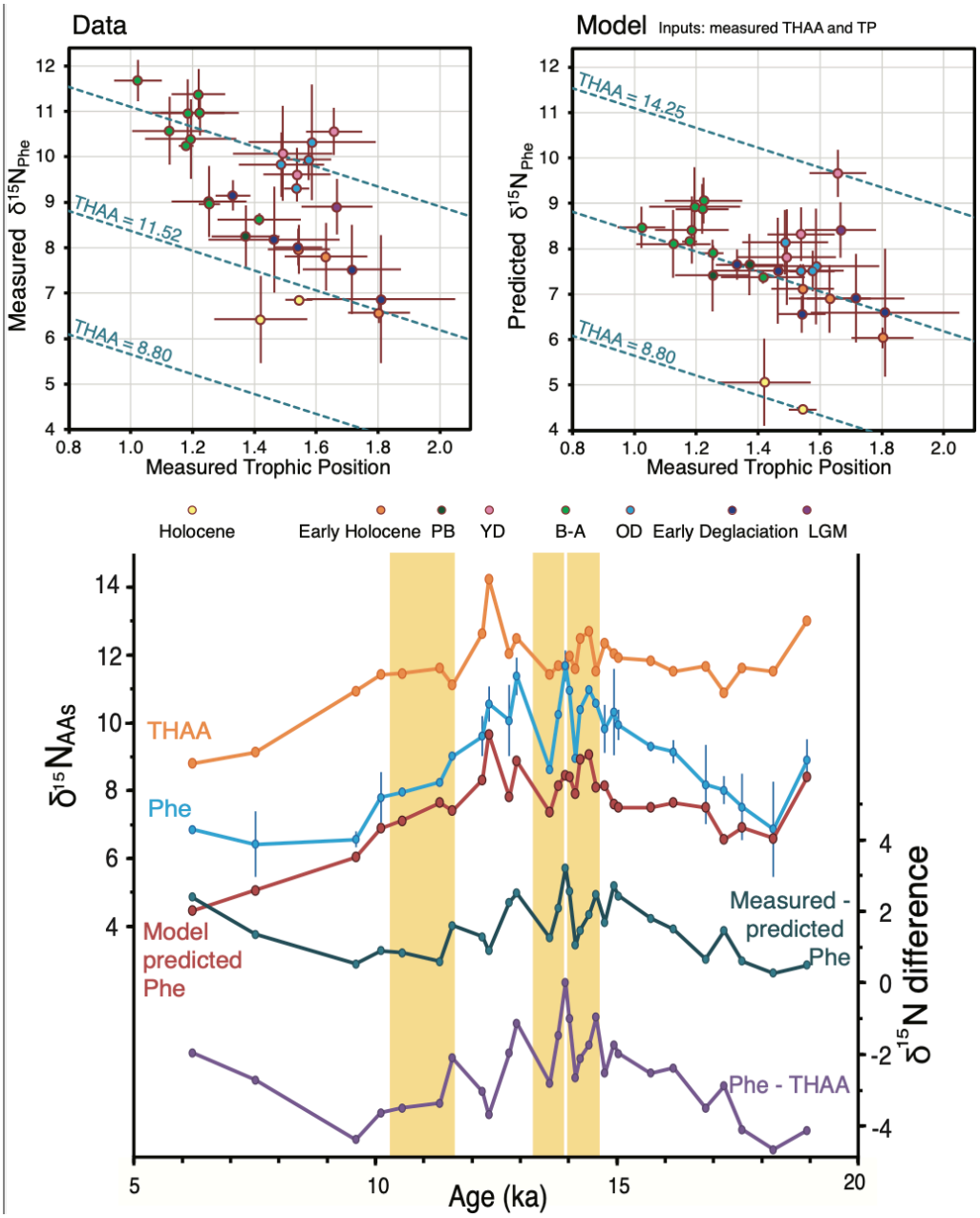

Figure 2.3: Assessing the TP-Phe relationship. (a) Predicted $\delta^{15}N_{Phe}$ from the Batista et al. model vs. Trophic Position. (b) Measured $\delta^{15}N_{Phe}$ vs. Trophic Position. The dashed blue lines represent the model-predicted Phe-TP relationship from the lowest measured $\delta^{15}N_{THAA}$ (8.80‰, near-coretop), highest measured $\delta^{15}N_{THAA}$ (14.25‰, mid-Younger Dryas), and the midpoint (11.52‰). (c) Measured $\delta^{15}N_{THAA}$ (orange), measured $\delta^{15}N_{Phe}$ (blue), model-predicted $\delta^{15}N_{Phe}$ (red), data-model $\delta^{15}N_{Phe}$ residual (teal), and the difference between $\delta^{15}N_{THAA}$ and $\delta^{15}N_{Phe}$ (purple). Yellow bars represent the presence of sedimentary laminations at this site which occur during the high-productivity PreBoreal and Bolling-Allerod intervals.

Our data do in fact display an inverse correlation (R^2= 0.41) as the Batista model would predict, with an overall trend quite similar to the the model-predicted relationship (Figure 3a and 3b). At the same time, our $\delta^{15}N_{Phe}$ data is higher in absolute value from the Batista model predictions by 1.5‰ on average and up to 3.2‰. This $\delta^{15}N_{Phe}$ data-model residual is largest (>2‰) in the Holocene, B-A, and OD samples and one YD sample (Figure 3c and 3d).

The overall inverse relationship between TP and Phe observed in our data demonstrates that samples with higher TP are indeed correlated to lower $\delta^{15}N_{Phe}$ values, suggesting depletion of $\delta^{15}N_{Src}$ likely occurs, presumably due to recycling and isotopic mass balance as proposed by Batista et al. 2014. However, it also appears that the Batista model does not fully capture the $\delta^{15}N_{Phe}$ dynamics throughout the record, meaning our understanding of the mechanisms driving these relationships must be incomplete. The mass-balance hypothesis as proposed by Batista et al. (2014) was predicated on N limitation, and thus need not apply in systems with excess N availability; this may be a partial explanation for why the model does not accuartely predict the $\delta^{15}N_{Phe}$ data. Another explanation could be related to ammonium use and trophic structure. We explore these in turn below.

One explanation for the data-model disrecepancy is that mass-balance did not control isotopic partioning of amino acid N during all or some of the time intervals. The modern conditions at this site are HNLC, meaning excess near-surface nitrogen exists throughout the year; the near-coretop (Holocene) sample also has a large data-model $\delta^{15}N_{Phe}$ residual (2.4‰) (Figure 3). If this “excess-DIN” explanation applies to

past intervals, then intervals with large data-model residuals may represent time periods with HNLC conditions, for example if iron or light availibility were stronger controls on production. This explanation therefore suggests that the Holocene and parts of the B-A, YD, and OD (the samples with high $\delta^{15}N_{Phe}$ data-model residuals) were periods with HNLC or excess-DIN conditions.

A second explanation may be related to the influence of "recycling," ammonium use, or other poorly understood trophic structure effects, that could drive $\delta^{15}N_{PON}$ ($\delta^{15}N_{THAA}$) values to differ from $\delta^{15}N_{DIN}$. The samples with the largest $\delta^{15}N_{Phe}$ data-model residuals are also those with minimal differences between measured $\delta^{15}N_{THAA}$ and measured $\delta^{15}N_{Phe}$ (Figure 3c). This is because the model parameters dictate that $\delta^{15}N_{Phe}$ must be between 3-5‰ lower than $\delta^{15}N_{THAA}$, but our measured $\delta^{15}N_{Phe}$ is offset from $\delta^{15}N_{THAA}$ by 3‰ or less in more than half the samples. This implies the $\delta^{15}N_{\textit{Phytoplankton}}$ and bulk $\delta^{15}N_{PON}$ were offset by 3‰ or less. Therefore, the $\delta^{15}N_{Phe}$ data-model residuals could be driven by THAA values that are "inaccurate" recorders of $\delta^{15}N_{DIN}$. More explicitly, these would be intervals where DIN had a high $\delta^{15}N$ signature, which caused higher $\delta^{15}N_{\textit{Phytoplankton}}$ ($\delta^{15}N_{Phe}$) values, but this did not also translate into high $\delta^{15}N_{PON}$ ($\delta^{15}N_{THAA}$) values (at least as the model predicted). This could be driven by varying ammonium use or other unknown trophic structure effects such as community composition influencing the $\delta^{15}N_{THAA}$ and $\delta^{15}N_{Phe}$ records differently during different time intervals. This explanation suggests that the observed depletion of $\delta^{15}N_{Src}$ is caused not solely by nitrate availability, but also by poorly understood recycling effects.

Overall, we hypothesize that samples with the highest $\delta^{15}N_{Phe}$ data-model residuals (i.e., where $\delta^{15}N_{Phe}$ is not strongly offset from $\delta^{15}N_{THAA}$) are intervals where mass-balance-driven depletion of $\delta^{15}N_{Src}$ did not occur, implying that $\delta^{15}N_{THAA}$ and $\delta^{15}N_{Src}$ are independent variables from TP when there is "excess" DIN supply. Intervals with minimal $\delta^{15}N_{Phe}$ data-model residuals appear to be times with more complete N utilization. This interpretation suggests the Bering Sea ecosystem may have switched between complete and incomplete N utilization multiple times throughout the record.

Whatever the driving mechanism between TP and $\delta^{15}N_{Phe}$, the linear fit of our data and the similarities in slope between our data and the model suggest the *potential* influence of TP on $\delta^{15}N_{Phe}$ can be quantified and accounted for. We therefore attempt to correct the $\delta^{15}N_{Phe}$ record for the TP-driven mass balance effect so that it better represents an estimate of the $\delta^{15}N_{DIN}$. We thus generated a new record, $\delta^{15}N_{SurfaceN}$ (Figure 4) using the Batista model to remove the predicted TP influence from our $\delta^{15}N_{Phe}$ record (as described in Section 2.3). For example, where TP = 1, there is no predicted TP-depletion of $\delta^{15}N_{Phe}$ and thus the correction is 0; at the highest TP of 1.81, the predicted $\delta^{15}N_{Phe}$ depletion is 1.77‰, which is added to the measured $\delta^{15}N_{Phe}$ value (6.87‰) to find $\delta^{15}N_{SurfaceN}$ (8.64‰). This record should reflect the shape, behavior, and trends of $\delta^{15}N_{SurfaceN}$, but not necessarily the absolute value, because source AAs reflect "baseline" (phytoplankton) values, which may be lower than surface N by ~5‰ due to uptake discrimination (D.M. Sigman & Casciotti, 2001). We also note that, because this $\delta^{15}N_{SurfaceN}$ record is derived directly from

$\delta^{15}N_{Phe}$ rather than from the average $\delta^{15}N_{Src,}$ its absolute values are higher than $\delta^{15}N_{Src.}$

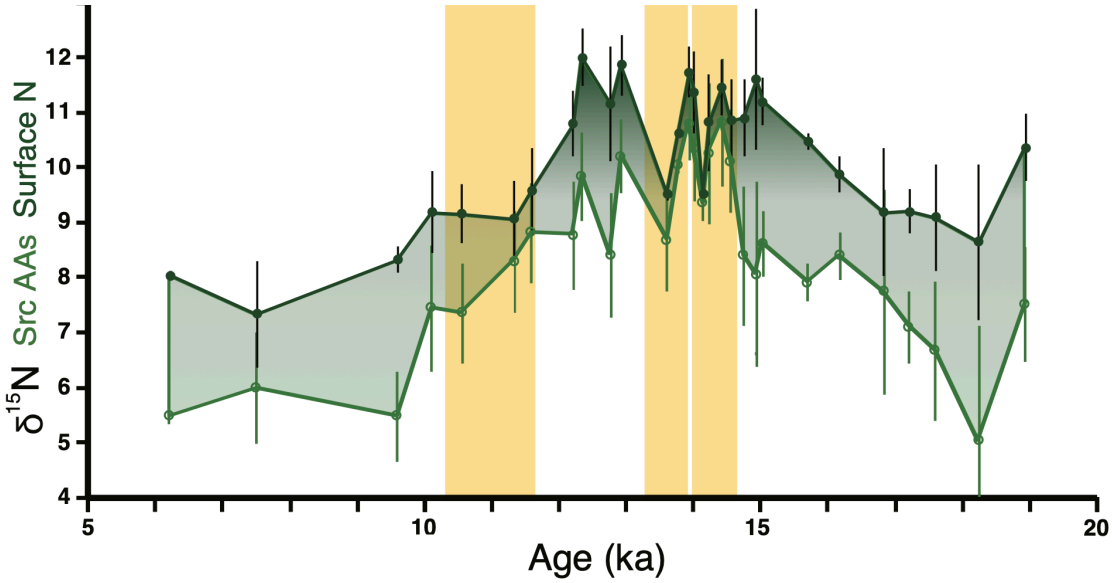

Figure 2.4: Comparison of $\delta^{15}N_{Src}$ (average source AAs) and the $\delta^{15}N_{SurfaceN}$ record, which is the $\delta^{15}N_{Phe}$ record corrected for TP-driven depletion.

The differences between the $\delta^{15}N_{Src}$ and $\delta^{15}N_{SurfaceN}$ records (green shading in Figure 3d) show the potentially large ambiguity between the Phe-derived $\delta^{15}N_{SurfaceN}$ record and the raw $\delta^{15}N_{Src}$ record. We do not have the information to assess which may best reflect $\delta^{15}N_{DIN}$ changes. However, we suggest $\delta^{15}N_{Src}$ is a better record than $\delta^{15}N_{THAA}$ for $\delta^{15}N_{DIN}$ changes in this region as long as the change is larger than 2‰ (because the maximum model-predicted $\delta^{15}N_{Phe}$ depletion is less than 2‰ in every sample).

In summary, our investigation finds a similar inverse relationship between $\delta^{15}N_{Phe}$ and TP as described in Batista et al. 2014 which suggests that, in some marine settings, the two parameters may be related. However, the modeled relationship does not appear to hold during all time intervals, likely due to changes in the

oceanographic conditions. We hypothesize that changes in surface N availability, and so the levels of N recycling and ammonia uptake are most likely responsible for these offsets. Future studies should investigate the settings and timescales on which this depletion might act.

5.2 TP of the Subarctic Pacific Ecosystem

Trophic Position (TP) in particles and sediments represents the average trophic structure of the planktonic ecosystem (Shen et al., 2021). TP at this site varies between 1.0 and 1.8, indicating substantial changes in ecosystem structure occurred over the record. Changes in TP are also coherent with climate events, suggesting that TP responded sensitively to regional climate, which is linked to changes in opal production and nutrient supply at this site (DeLong et al 2024; Figure 5).

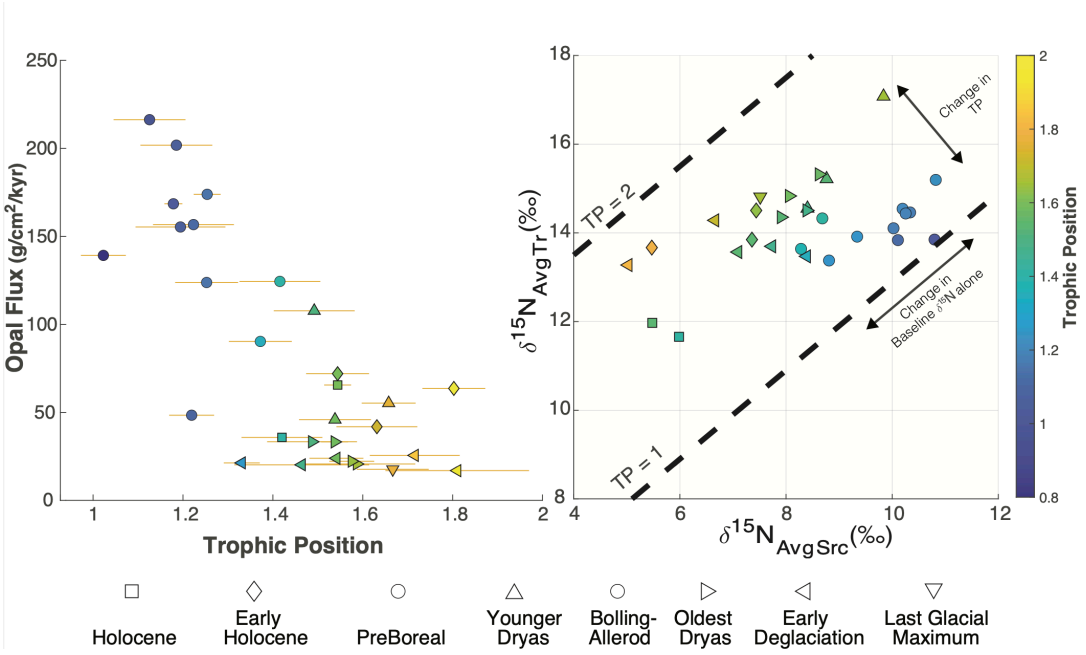

Figure 2.5: Trophic Position trends. (a) Correlation between Trophic Position and Opal Flux. (b) $\delta^{15}N_{Src}$ vs. $\delta^{15}N_{Tr,}$ colored by TP, showing the large range of $\delta^{15}N_{Src}$ changes indicating changes in baseline signatures.

Low-TP ecosystems typically occur when high nutrient supply supports larger phytoplankton cells and more direct energy transfer to higher trophic levels; high-TP ecosystems in contrast occur where low nutrient supply favors smaller primary producers, and are more typical of oligotrophic open ocean conditions (Chavez et al., 2011; M Décima, 2022). DeLong et al. 2024 used Si isotopes to determine that opal flux ($g \cdot cm^{-2} \cdot ka^{-1}$) is an indicator of macronutrient availability at this site. Thus, the correlation between TP and opal flux ($R^2 = 0.58$; Figure 5a) suggests TP at this site is significantly determined by bottom-up factors such as nutrient availability and phytoplankton size, supporting the theoretical framework for use of TP in paleorecords.

Opal flux is solely a measure of diatom production rather than all primary production, but diatoms are the most important phytoplankton group in this region (Onodera & Takahashi, 2009). Nitrogen flux (N flux, $g \cdot cm^{-2} \cdot ka^{-1}$, Figure 6), a measure of organic matter export to the sediments, roughly co-varies with opal flux but is less well correlated to TP ($R^2 = 0.29$). This lessened correlation is likely because N flux represents total export production, including non-siliceous phytoplankton and organic matter from zooplankton and heterotrophic bacteria. Furthermore, organic matter export may be determined by more complex factors than primary productivity alone, including top-down factors, remineralization during sinking, and post-depositional preservation.

The relationship between $\delta^{15}N_{Src}$ and $\delta^{15}N_{Tr}$ in our record indicates large changes in baseline $\delta^{15}N$ control much of the record (Figure 5b). Dashed lines

representing constant TP values show the magnitude of change expected in both AA groupings if baseline $\delta^{15}N$ value alone (i.e., $\delta^{15}N_{Phytoplankton}$) was changing (Chikaraishi et al., 2014). When data falls parallel to these trophic isoclines, it represents a system where the baseline signature changed, but with no change in ecosystem structure ("no change" in TP arrow). The overall trend in the data therefore suggests large baseline changes (due to $\delta^{15}N_{DIN}$ or utilization) most affected our record, both within specific periods of higher or lower TP values, and between climate intervals. The lower TP values all occur in the B-A, and are associated with higher $\delta^{15}N_{Src}$ values (dark blue circles in Fig. 2b). In contrast, the higher TP (yellow and green, occurring during the Early Deglaciation and Holocene) are associated with low $\delta^{15}N_{Src}$. One data point, which occurs in the mid-Younger Dryas, shows a similar $\delta^{15}N_{Src}$ to the B-A with a much higher TP, representing an ecosystem-driven change in $\delta^{15}N_{Tr}$; this data point also corresponds to the highest $\delta^{15}N_{THAA}$ value and the point with Ala-Thr values most similar to fecal pellets (SI Fig. 2).

The TP and $\delta^{15}N_{Src}$ values thus reveal the evolution of the region's ecosystem, with TP mainly reflective of opal production and large primary producers, and with $\delta^{15}N_{Src}$ values that are primarily driven by baseline changes. In the next section, we discuss the implications of these findings by climate interval.

5.3 The Subarctic Pacific through the Deglaciation

We can now use our new CSI-AA data, coupled with past work on this region, to draw a more detailed picture of shifts in production, plankton community structure, and N cycling through the deglaciation.

During the Last Glacial Maximum (LGM, 19-22 ka), both surface and intermediate waters were likely low in macronutrients, particularly nitrogen, throughout the subarctic Pacific (DeLong et al., 2024; H. Ren et al., 2015). Iron supply was higher during glacial boundary conditions, so nitrogen or light availability may have been limiting factors during the LGM and early deglaciation (Lam et al., 2013; H. Ren et al., 2015). The Bering Sea experienced seasonal or perennial sea ice cover and a stratified water column, and productivity was low, as seen in the opal flux and N flux records at our site (Figure 6, (DeLong et al., 2024). Diatom genera that indicate environmental conditions suggest stratification occurred in the photic zone (Figure 6a, showing the relative % of all *Actinocyclus, Coscinodiscus, Rhizosolenia, and Thalassiothrix* species; DeLong et al., 2024). As a result of these conditions, TP appears to have been relatively high (~1.7), indicating more microbial-dominated and complex trophic webs and suggesting that much of the primary production consisted of smaller producers, which may have included small diatoms, haptophytes, or cyanobacteria.

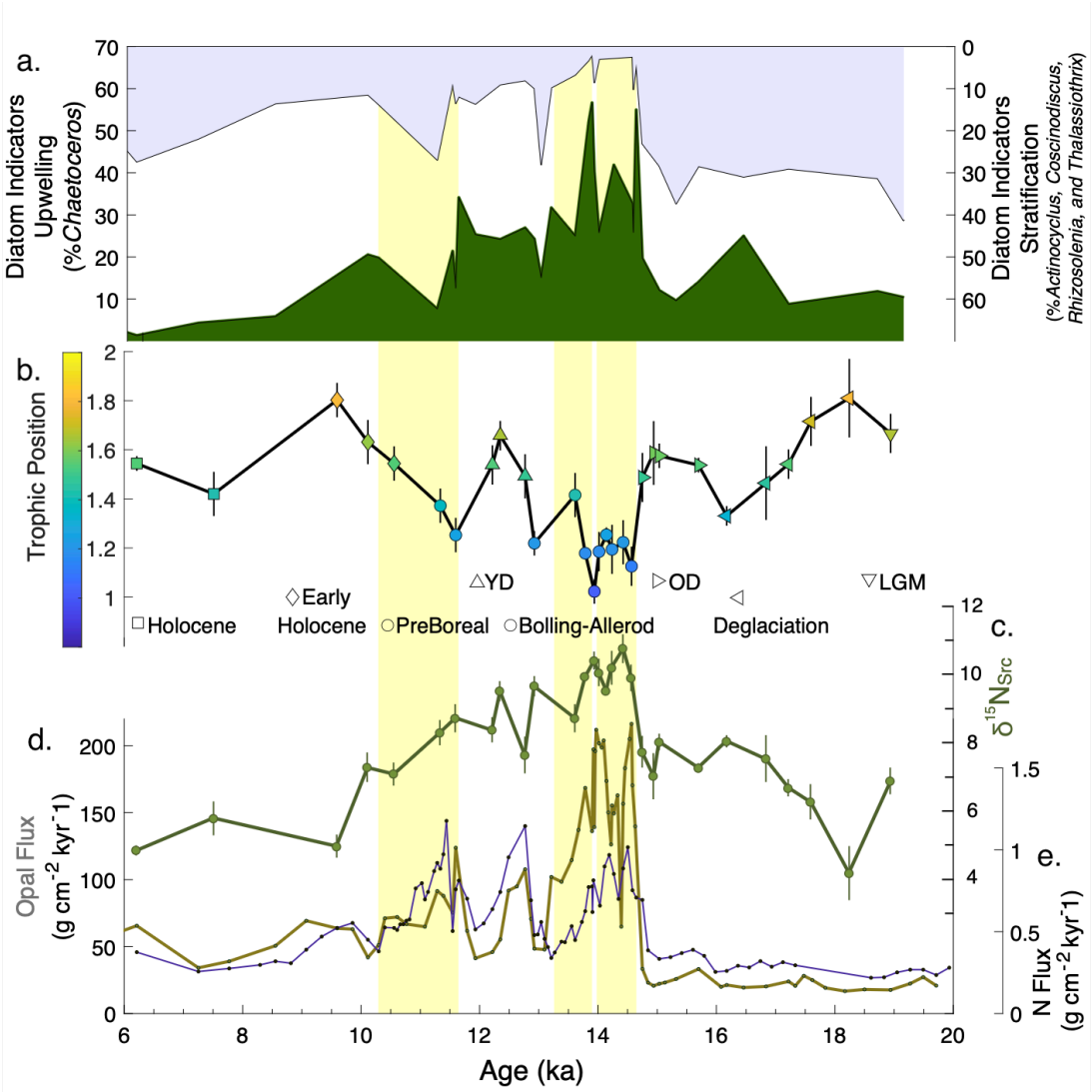

Figure 2.6: Deglacial changes. (a) Diatom indicators from DeLong et al. 2024 show the environment switched between upwelling (green) and stratification (light purple, axis reversed to demonstrate these are cumulative percentages). (b) Community TP, colored by TP and with time periods listed along with different-shaped markers to denote time period. (c) $\delta^{15}N_{Src}$ (d) Opal Flux ($g \cdot cm^{-2} \cdot ka^{-1}$), brown, and (e) N flux ($g \cdot cm^{-2} \cdot ka^{-1}$), dark purple, from DeLong et al. 2024.

As the global deglaciation commenced, LGM-like conditions mostly continued from 15-18 ka at this site (Figure 6), including low opal flux and stratification. A brief response in the TP and upwelling records ~16 ka may reflect Siku Event 1. Although total production does not appear to have been affected, there

is an uptick in % *Chaetoceros*, a diatom genus that is an upwelling indicator; this time also shows slightly higher authigenic uranium, which may indicate slightly higher organic export (SI Fig. 5). The slight decrease in the TP to 1.4 is consistent with increased upwelling leading to slightly shorter trophic webs or more direct algal deposition on the seafloor.

Following this brief event, moderately high (~1.6) TP resumes during the Oldest Dryas interval, defined here as 14.8-16 ka, a time with increased sea-ice in the region (DeLong et al., 2024; Detlef et al., 2020). At this site productivity remained low, but it may have increased in the Gulf of Alaska or other marginal environments (Davies et al., 2011; S. K. Praetorius et al., 2015).

The Bolling-Allerod (B-A, 14.7-12.9 ka) was a high-productivity event across the entire subarctic Pacific; at this site, opal productivity was two- to three-fold higher than the modern ocean (DeLong et al., 2024). In our record, TP immediately shifts to values around 1.2 for the duration of the high productivity, which suggests the ecosystem radically restructured in response to this climate event. High nutrient availability may have favored large diatoms over smaller producers, making trophic chains more direct. In addition to higher primary production, the B-A was a time of significant regional warming, rapid sea ice retreat, and rapid sea level rise that began to flood the continental shelves (Davies et al., 2011; Detlef et al., 2020). The breakdown of surface and intermediate stratification potentially released a large supply of macronutrients from the upwelling of nutrient-rich Deep Pacific Water (Brunelle et al., 2007; DeLong et al., 2024; Galbraith et al., 2007; Gray et al., 2018).

Together, these coincident changes would have contributed to ecosystem restructuring. For example, where deep winter mixing occurs, copepods hibernate overwinter, leading to spring blooms which are not efficiently grazed (Friedland et al., 2016; Kimmel et al., 2018).

The $\delta^{15}N_{Src}$ signal also increases sharply at the instigation of the B-A, suggesting a change in $\delta^{15}N_{DIN}$ (Figure 6). Because the TP reaches 1.0 during the mid-BA, the $\delta^{15}N_{Src}$ value should indicate a pure $\delta^{15}N_{baseline}$ signature (i.e., $\delta^{15}N_{Phytoplankton}$) with no trophic-driven influence. This $\delta^{15}N_{Src}$ value, 10.8‰, is significantly higher than the near-coretop $\delta^{15}N_{Src}$ value (~5.5‰, which is similar to modern estimates), indicating $\delta^{15}N_{DIN}$ was at significantly higher during the mid-deglaciation. This could result from increased utilization or a new nitrate source with a different preformed $\delta^{15}N_{DIN}$ signature, or both. If the B-A was an interval of HNLC-like conditions similar to today (DeLong et al., 2024), nitrogen utilization may have been incomplete; this would indicate the cause of the high $\delta^{15}N_{PON}$ was more likely from a higher preformed $\delta^{15}N_{DIN}$ signature. The B-A and PB are associated with hypoxia at intermediate depths allowing for water-column denitrification to occur, which could be the origin of higher preformed $\delta^{15}N_{DIN}$ (Brunelle et al., 2007; Schlung et al., 2013).

The Younger Dryas (12.9-11.8 ka) shows lower productivity and a return to higher TP values (~1.6), similar to the early deglaciation, again showing ecosystem restructuring in response to regional climate change. The $\delta^{15}N_{Src}$ signal stays ~8‰, still high compared to modern values, but lower than the B-A, which could indicate

less influence of denitrification; the changes could also be utilization-driven. The diatom community does not show a clear shift at the transition between the B-A and YD; upwelling indicators still occur, and nutrients may have been plentiful despite lower opal production (DeLong et al., 2024), which suggests the ecosystem response was due to other climate factors such as shifts in nutrient supply stoichiometry, stratification, sea ice, or circulation changes related to hemispheric cooling. Although the opal flux decreases, the N flux is relatively high in the Younger Dryas, indicating efficient export production (Figure 6). The TP is similar to the early deglaciation, likely related to smaller phytoplankton at the base of the food web. Smaller phytoplankton would usually have lower export efficiency than large phytoplankton, thus, it is likely the export production from zooplankton was quite high. Indeed, the Ala-Thr data (SI Fig. 2) shows the mid-YD data point is the closest to fecal pellet values.

The PreBoreal (11.7-10.5 ka) is another warm event, which shows an increase in opal flux similar to the B-A but less extreme. TP likewise drops to ~1.2 for a short duration. Following the PreBoreal, three samples from 9.5-10.5 ka represent a transitional period into the Holocene (0-10 ka), which display increasingly high TP values, reaching ~1.8; it is unclear what drove this shift, but it may be related to the cessation of deglacial conditions such as decreased wind forcing, low nutrient supply, the opening of the Bering Strait, or the formation of modern North Pacific Intermediate Water (Gray et al., 2018; Kuehn et al., 2014; Sarnthein et al., 2004). The $\delta^{15}N_{Src}$ values remain ~8‰ and then decline from the PB into the Holocene.

Finally, the near-coretop values, dated to ~6-8 ka, represent Holocene conditions similar to the modern ocean, with moderately high productivity and HNLC conditions (DeLong et al., 2024). The moderate TP values are similar to modern estimates and the youngest $\delta^{15}N_{Src}$ value of 5.5‰ is similar to the near-coretop bulk $\delta^{15}N$ value of 4.6‰, considered a reasonable value for modern sinking particulate organic nitrogen (PON) in the region where local source nitrate is ~6.5‰ and there is incomplete utilization (Schlung et al., 2013).

In summary, we find that Trophic Position, and therefore planktonic community structure, responds to regional climate change. Warm, high-productivity periods are associated with low TP and colder, lower-nutrient, or more stratified conditions associated with higher TP. The changes in TP at this location are primarily mediated by nutrient supply and opal productivity (DeLong et al., 2024). These findings are consistent with the framework that high nutrient supply leads to larger phytoplankton, more diatoms, and shorter, more direct trophic chains, while environments with smaller phytoplankton are associated with more complex trophic webs and more zooplankton than phytoplankton export (Chavez et al., 2011; M Décima, 2022).

5.3 Comparison with Fossil-Bound Records

Finally, an important question for CSI-AA in sediments is determining to what degree CSI-AA parameters reconstruct original primary production $\delta^{15}N$ values. Bulk-sediment $\delta^{15}N$ records are often interpreted as if they are reflective of $\delta^{15}N_{\textit{phytoplankton}}$ or $\delta^{15}N_{DIN}$ changes; however, the impacts of ecosystem export,

preferential preservation, and diagenesis are all well known to affect bulk signals (Robinson et al., 2012). One approach to this problem is to measure fossil-bound $\delta^{15}N$ in diatoms or foraminifera, with the assumption that N bound in a mineral matrix is largely immune from diagenetic impacts (Robinson et al., 2023). As a start in assessing how CSI-AA records may compare to these methods, we compare our results to nearby diatom-bound records and then to foraminifera-bound records from the open subarctic Pacific.

There are a number of outstanding uncertainties regarding nitrogen utilization in the deglaciating subarctic Pacific, particularly the changes between the LGM, early deglaciation (19-15 ka), and Bolling-Allerod. Diatom-bound and foraminifera-bound records both show higher $\delta^{15}N$ at LGM than the modern ocean; this has been interpreted as higher nutrient utilization, due to lower N supply, higher Fe supply, or both. Diatom-bound $\delta^{15}N$ records then show a decrease in the early deglaciation, and a return to higher values in the B-A; in contrast, foraminifera-bound records find no changes from the LGM through the early deglaciation and B-A (Figure 7, H. Ren et al., 2015). These different findings imply different interpretations about the origin of the higher $\delta^{15}N$ during the B-A: the diatom-derived records imply either increased utilization (for example, due to Fe fertilization) or a higher $\delta^{15}N$ signature in upwelling waters due to regional denitrification; on the other hand, the foram-derived records could imply no change in either utilization or $\delta^{15}N_{DIN}$, merely a change in gross nitrate supply (Brunelle et al., 2007; H. Ren et al., 2015; Schlung et al., 2013). CSI-AA can potentially address these conflicting interpretations using separate

proxies for baseline $\delta^{15}N$ ($\delta^{15}N_{Src}$) and the $\delta^{15}N$ of particulate organic nitrogen ($\delta^{15}N_{THAA}$).

For visual comparison, we also include our $\delta^{15}N_{SurfaceN}$ record, which is our $\delta^{15}N_{Phe}$ record corrected for possible TP-driven depletion (Figure 7). Including this record demonstrates the large uncertainties that relate our $\delta^{15}N_{Src}$ record to surface N; nevertheless, some conclusions can be drawn.

Before making a direct comparison between the diatom-bound $\delta^{15}N$ records ($\delta^{15}N_{d\text{-}b}$) and $\delta^{15}N_{Src}$ or $\delta^{15}N_{SurfaceN}$, it is important to consider to what extent we should expect them to agree. The nitrogen compounds in diatom frustules are highly selected compared to bulk cellular nitrogen (or sinking PON), and includes structural proteins, long-chain polyamines, and chitins (Robinson et al. 2023 and refs therein). This set of very specific N-containing compounds, as well as likely unique molar distributions, suggests that $\delta^{15}N_{d\text{-}b}$ likely should not record $\delta^{15}N$ identical values to AAs, which solely reflect average exported proteinaceous material. This further suggests that offsets are expected, and that if these are known calibrations might relate $\delta^{15}N_{d\text{-}b}$ to the original biomass $\delta^{15}N$, allowing a comparison can be made. Temporal considerations may also be important, as $\delta^{15}N_{AAs}$ represent an integrated primary production signal, and $\delta^{15}N_{d\text{-}b}$ may represent a particular season or be affected by floristic shifts throughout the record. Finally, a more difficult question is if the mass-balance model of Batista et al. should also apply to fossil-bound N. If the fossil-bound nitrogen is primarily proteinaceous, then we might expect that any mass-balance-driven depletion $\delta^{15}N_{SourceAAs}$ would also impact $\delta^{15}N_{d\text{-}b}$ values; however, this

is not a guarantee, because the $\delta^{15}N$ of each protein or amine may have a unique isotope fractionation effect due to the cellular machinery at work, and this is largely unknown (Robinson et al., 2023). Furthermore, the timescales and mechanisms which act to deplete $\delta^{15}N_{SourceAAs}$ due to "mass balance" are also unknown.

Keeping in mind these multiple caveats, we compare our $\delta^{15}N_{Src}$ and $\delta^{15}N_{SurfaceN}$ records to nearby $\delta^{15}N_{d\text{-}b}$ records (Brunelle et al., 2007) (JPC17; location shown on Fig 1, purple diamonds). A second site in the open Subpolar North Pacific (SNP) shows similar values (Studer et al., 2013) (Core SO202-07-6, location shown on Fig 1, brown diamonds). The $\delta^{15}N_{d\text{-}b}$ is isotopically depleted from surface $\delta^{15}N_{DIN}$ by its ε of -5‰ (H. Ren et al., 2015; D.M. Sigman & Casciotti, 2001), which should create a value close in absolute value to the $\delta^{15}N_{Src}$ record, which likewise should be reflective of phytoplankton values and thus lower than or equal to $\delta^{15}N_{DIN}$. Our new $\delta^{15}N_{SurfaceN}$ record has been corrected, which may make it higher in absolute value than $\delta^{15}N_{Src}$.

In terms of shape, the JPC17 $\delta^{15}N_{d\text{-}b}$ and $\delta^{15}N_{Src}$ records both show a decrease from the LGM to the Holocene, as well as a decrease from higher B-A values to lower Holocene values. Higher $\delta^{15}N$ values during the LGM have been interpreted as increased nutrient utilization from lower N supply creating a higher regional $\delta^{15}N_{DIN}$ (Brunelle et al., 2007, 2010; Studer et al., 2013); our results agree with this interpretation. As discussed in Section 5.2, we interpret our higher $\delta^{15}N_{Src}$ values in the B-A as representing a higher $\delta^{15}N$ signature in upwelling waters primarily due to regional denitrification. This elevated $\delta^{15}N$ signature appears to be much stronger in

the $\delta^{15}N_{Src}$ than the $\delta^{15}N_{d\text{-}b}$ records, with up to 5‰ higher $\delta^{15}N$ values throughout the PB, YD, B-A, and OD.

Differences between the $\delta^{15}N_{d\text{-}b}$ and $\delta^{15}N_{Src}$ records could represent floristic shifts in diatom species composition or seasonal dynamics affecting the $\delta^{15}N_{d\text{-}b}$ record (Studer et al., 2013). For example, *Chaetoceros* resting spores are known to be 5-7‰ lower than other diatoms (Dove et al., 2023). The B-A, YD, and PB intervals are 30-50% *Chaetoceros* by species count at our site (Figure 7), which is likely to be similar to the other Bering Sea site (although *Chaetoceros* are smaller in volume than most other diatoms found here) (DeLong et al., 2024). Diatom-bound samples also tend to be comprised of the largest diatoms, such as *Coscinodiscus*, a nutricline-dwelling, fall-bloom genus, which is more likely to grow directly on subsurface N (and thus have a lower $\delta^{15}N$) than the rest of summer production, which would incorporate higher $\delta^{15}N$ values from more complete utilization, and which might dominate an integrated-production record such as $\delta^{15}N_{Src}$. These examples demonstrate how floristic shifts and seasonal bloom dynamics could explain why the $\delta^{15}N_{d\text{-}b}$ records are lower than the $\delta^{15}N_{Src}$ record during the PB, YD, and B-A.

Detailed analysis beyond this basic outline is limited by the lower resolution of the diatom-bound record, and therefore must be somewhat speculative. Nevertheless, the YD and OD intervals appear to show consistent differences between the $\delta^{15}N_{d\text{-}b}$ and $\delta^{15}N_{Src}$ records: both intervals show a low $\delta^{15}N_{d\text{-}b}$ but an elevated $\delta^{15}N_{Src}$, and our $\delta^{15}N_{SurfaceN}$ record suggests surface N may have been even more elevated during these intervals. As these intervals are characterized by high TP and

N-limitation, one tentative explanation for lower $\delta^{15}N_{d\text{-}b}$ values during these times is the nitrogen recycling associated with higher-TP ecosystems, which could be causing mass-balance-driven depletion of the $\delta^{15}N_{SourceAA}$ record, perhaps caused even stronger depletion in the $\delta^{15}N_{d\text{-}b}$ record. Floristic shifts could contribute to the low values of the YD; however, they cannot explain the decrease in $\delta^{15}N$ between the LGM and the Early Deglaciation, during which almost no changes in the diatom community occurred at our site (DeLong et al., 2024) and are unlikely to have occurred at the diatom-bound sites (Studer et al., 2013). The authors of those studies suggested the extremely low values that occur during the Early Deglaciation and Oldest Dryas were caused by the inclusion of sponge spicules in their samples, which have low opal-bound $\delta^{15}N$ values, and were particularly abundant in those samples (H. Ren et al., 2015; Studer et al., 2013). This may be the case, but we note a slight decrease in our $\delta^{15}N_{Src}$ record between the LGM (19 ka) and the early deglaciation, which continues to be difficult to explain, as there is no known reason for a decline in nutrient consumption to occur at this time (Brunelle et al., 2007, 2010; Studer et al., 2013). Future work should investigate whether increased nitrate consumption under high-TP conditions can counterintuitively lead to lower $\delta^{15}N_{\textit{phytoplankton}}$ due to intense recycling.

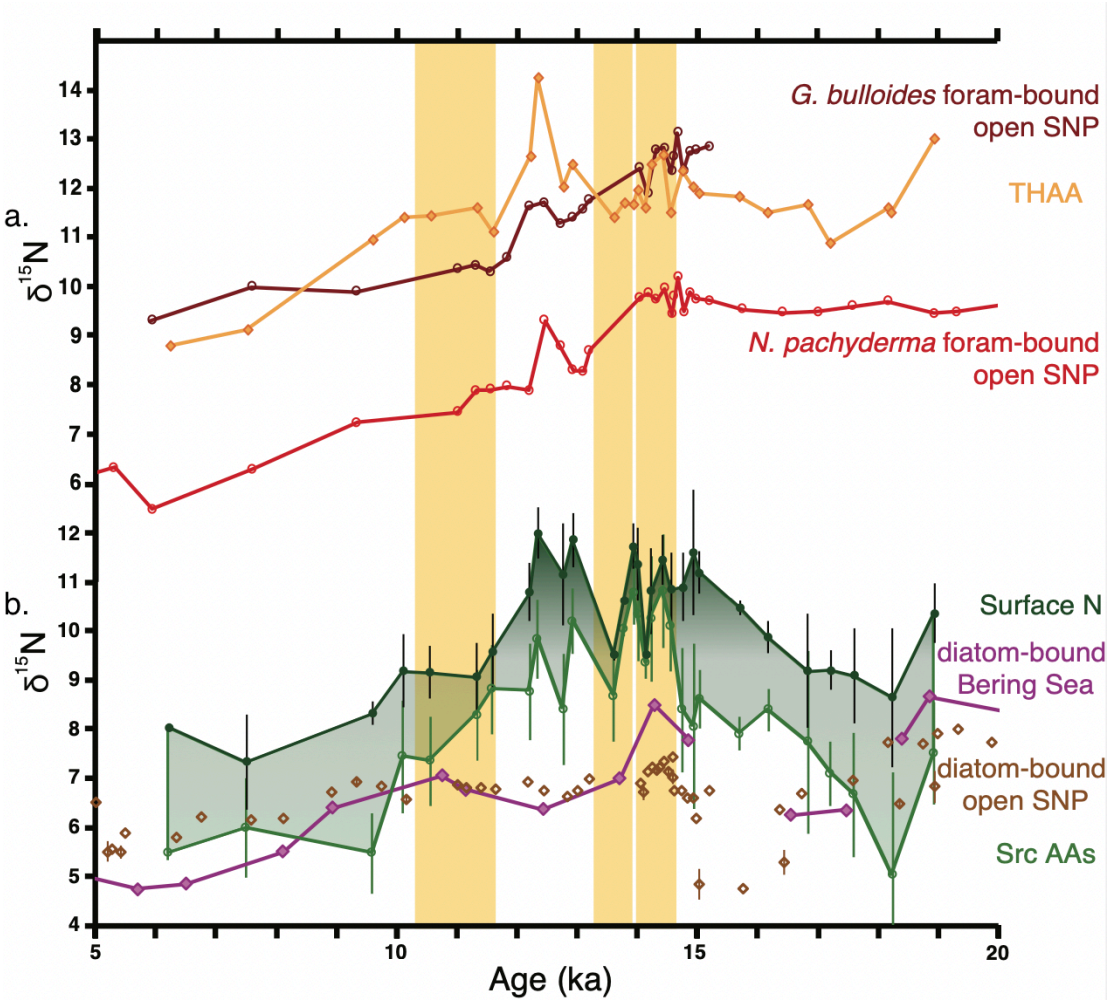

Figure 2.7: Comparison of CSI-AA with fossil-bound records. Above, comparison of our THAA data with two nearby foraminifera-bound records, *G. bulloides* in dark red, *N. pachyderma* in bright red from the open Subarctic North Pacific (SNP) (H. Ren et al., 2015). Below, our average $\delta^{15}N_{Src}$ and $\delta^{15}N_{SurfaceN}$ records with two nearby diatom-bound records; the Bering Sea in purple and the open SNP in brown (Brunelle et al., 2007; Studer et al., 2013).

Lastly, we compare our $\delta^{15}N_{THAA}$ record to two single-species foraminifera-bound records ($\delta^{15}N_{f\text{-}b}$), *Globigerina bulloides* and *Neogloboquadrina pachyderma,* from the open SNP site SO202-7-6, which show good agreement with one another (H. Ren et al., 2015). The offset between the two $\delta^{15}N_{f\text{-}b}$ records is attributed to the trophic position of the species. *N. pachyderma* does not bear algal symbionts and is a

mixed-layer dweller with a habitat generally between 50-150 m depth; it feeds on suspended PON including phytoplankton, detrital material, and bacteria in marine snow (Smart et al., 2020). The typical offset between $\delta^{15}N_{N.pachyderma}$ and particulate organic nitrogen (PON) is generally ~3‰, reflecting its heterotrophic diet (Smart et al., 2020). Where nitrate consumption is incomplete, and $\delta^{15}N_{PON}$ is therefore not synonymous with $\delta^{15}N_{DIN}$, foraminifera-bound $\delta^{15}N$ resembles bulk suspended PON $\delta^{15}N$ (Smart et al., 2020). For example, if diatom $\delta^{15}N$ is 5‰ lower than $\delta^{15}N_{DIN}$, then $\delta^{15}N_{N.\ pachyderma}$ would be expected to be about 2‰ lower than $\delta^{15}N_{DIN}$. *G. bulloides* is also a mixed-layer dweller but prefers active carnivory of zooplankton, it is thus ~3‰ enriched over *N. pachyderma* due to its diet.

Our $\delta^{15}N_{THAA}$ record should also record bulk exported PON, with an expected offset of ~2-5‰ compared to algal biomass ($\delta^{15}N_{Src}$) (Batista et al., 2014).

There is fairly good agreement between our $\delta^{15}N_{THAA}$ and the $\delta^{15}N_{f\text{-}b}$ records, with all records recording a local peak in the Younger Dryas and finding a ~5‰ decrease between the LGM and B-A versus the Holocene. However, the $\delta^{15}N_{N.pachyderma}$ shows almost no change from the LGM through the Early Deglaciation and B-A, while the $\delta^{15}N_{THAA}$ record shows some minor variability. Differences between the $\delta^{15}N_{THAA}$ and $\delta^{15}N_{f\text{-}b}$ records could indicate that different dynamics occurred in the open Subpolar North Pacific compared to our site in the Bering Sea. In the modern ocean, the Bering Sea receives more influence from the continental shelf and the Gulf of Alaska, so these circulation differences may have

also acted during these past intervals. However, as with the diatom-bound records, we will assume similar dynamics occurred in the Bering Sea and the open SNP.

Our $\delta^{15}N_{THAA}$ record demonstrates why a PON or foraminifera-bound record can be unchanging between the LGM, Early Deglaciation, and B-A despite the large changes in productivity, TP, and $\delta^{15}N_{Src}$ shown in Figure 7. The YD peak in our $\delta^{15}N_{THAA}$ record is caused by the confluence of a high $\delta^{15}N_{Src}$ signal (reflective of a high $\delta^{15}N_{DIN}$ and more complete N utilization), high Trophic Position, and a higher contribution of fecal pellets to PON. We suggest these dynamics are the reason the $\delta^{15}N_{f\text{-}b}$ records also peak in the YD. This additive effect demonstrates how, if compensating changes in $\delta^{15}N_{DIN}$ and TP were to occur, they would not necessarily be recorded in a PON record. For example, if a lower $\delta^{15}N_{DIN}$ signature coincided with higher N utilization and higher TP, the $\delta^{15}N$ of PON could be elevated despite the lower $\delta^{15}N_{DIN}$, as demonstrated in the large differences between our $\delta^{15}N_{THAA}$ and $\delta^{15}N_{Src}$ records during the Early Deglaciation (Figure 7). Likewise, we suggest a higher $\delta^{15}N_{DIN}$ combined with lower N utilization and lower TP led to a similar $\delta^{15}N_{THAA}$ value in the B-A as the Early Deglaciation, despite major reorganizations in circulation and ecosystem structure.

In conclusion, we suggest both $\delta^{15}N_{THAA}$ and $\delta^{15}N_{f\text{-}b}$ are best thought of as records of bulk exported PON. In ecosystems with complete N utilization, where $\delta^{15}N_{PON}$ faithfully records $\delta^{15}N_{DIN}$, it may be a useful proxy for $\delta^{15}N_{DIN}$. In this ecosystem setting in the HNLC Subarctic Pacific, where $\delta^{15}N_{PON}$ does not perfectly

record $\delta^{15}N_{DIN}$, $\delta^{15}N_{THAA}$ and foraminifera-bound records are of limited use without further context.

6 Summary and Conclusions

In summary, we used a Bering Sea sedimentary record through the last deglaciation to first test the mass-balance hypothesis that posits $\delta^{15}N_{Src}$ values are depleted by recycling (as measured by Trophic Position) and find that this depletion does occur, but possibly is significant only under certain oceanographic conditions. As a result, the TP-Phe relationship should be accounted for when interrogating the past for changes in $\delta^{15}N_{DIN}$ signatures. If the TP dynamics of a system are known and accounted for, changes in nitrogen cycling can be examined using $\delta^{15}N_{Src}$ or $\delta^{15}N_{Src}$ with a small correction. We conclude that the mid-deglaciation showed significant changes in water mass source to the region, with a high $\delta^{15}N_{DIN}$ signal affecting the B-A and Older Dryas. This may be the result of regional denitrification, utilization changes, or a combination of both during various climate intervals. We also find ecosystem Trophic Position responds sensitively to regional climate events, with high-productivity intervals characterized by low TP values, driven by increased diatom production. Finally, comparison to nearby records suggests $\delta^{15}N_{Src}$ and $\delta^{15}N_{d\text{-}b}$ record similar signals, but many sources of uncertainty remain in understanding any discrepancies between the two, including floristic shifts, seasonal dynamics, and the composition of diatom-bound nitrogen compounds. Our $\delta^{15}N_{THAA}$ record agrees well with nearby $\delta^{15}N_{f\text{-}b}$ records, suggesting both are good proxies for particulate organic nitrogen $\delta^{15}N$.

Shifts in TP in response to climate intervals of the deglaciation are oceanographically consistent with hypotheses about shifts in planktonic community structure and nutrient supply, supporting previous suggestions that TP may be one of the most informative CSI-AA parameters in paleorecords (Batista et al., 2014). We interpret our Bering Sea record as if changes in TP are well-preserved and reflect original surface-community values. However, more work is needed to verify the extent to which particle sinking, burial, and diagenesis may alter these signals. We also suggest that large baseline changes over the deglaciation were primarily driven by changes in $\delta^{15}N_{DIN}$, which we link to circulation changes. Unfortunately, the precise timing of circulation changes, as well as nitrogen utilization during the Early Deglaciation and Oldest Dryas intervals, remains ambiguous, as a higher $\delta^{15}N_{DIN}$ signal may have been driven by either utilization or denitrification, which both varied during different geologic intervals.

We find some evidence that under high-TP conditions and complete nitrate consumption, N recycling may lead to lower $\delta^{15}N_{phytoplankton}$ values; future work should verify that "mass-balance" hypothesis is correct and that the depletion of Source AA $\delta^{15}N$ does indeed occur relative to $\delta^{15}N_{DIN}$. Future studies should investigate the mechanisms which underpin this $\delta^{15}N_{Src}$ depletion, the conditions under which those mechanisms occur, and on what timescales they act. A better understanding of these mechanisms will reveal to what extent $\delta^{15}N_{SourceAA}$ and diatom-bound $\delta^{15}N$ should record the same values, which would have significant implications for interpreting both extant and future paleo-records. We also suggest

that because $\delta^{15}N_{THAA}$ and foraminifera-bound $\delta^{15}N$ records appear to generally record $\delta^{15}N_{PON}$, they are best used as proxies for $\delta^{15}N_{DIN}$ changes only where complete N consumption is constant throughout the record. These results highlight the importance of using the correct interpretive framework when interrogating the sedimentary record for past changes in the nitrogen cycle. On the whole, our study suggests that, if there is good preservation of amino acids, CSI-AA of bulk-sediment samples can reveal detailed information about past ecosystem structure and changes in baseline $\delta^{15}N$.

Supplemental Text and Figures

The degradation index (DI) was calculated using relative molar abundance as described in Dauwe & Middelburg, 1998 using the recovered AAs (i.e., excluding Tyr, Met and Arg). This results in three DI values >1.0, which is not a valid finding as the original index only ranged from -3 to +1. This demonstrates the difficulty in interpreting DI values when the original AAs cannot all be included in the calculation. However, there is good agreement between DI and % Glycine (%Gly), which could explain why DI is a useful point of reference.

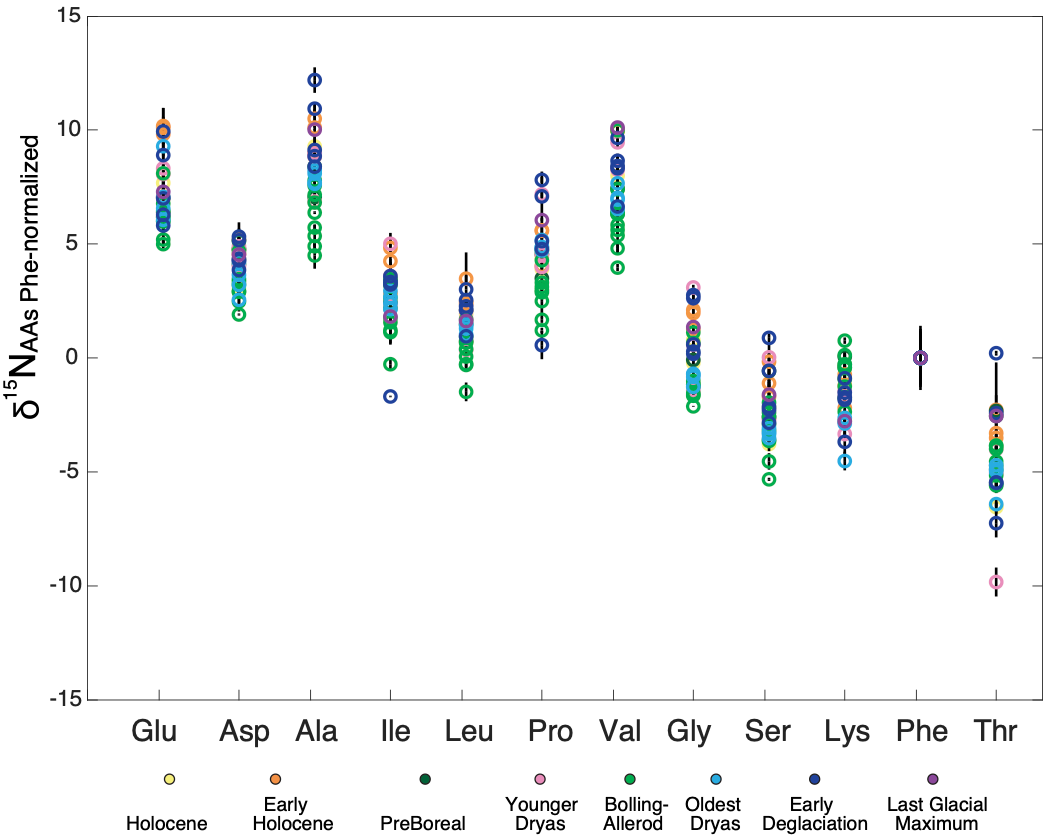

Supplemental Figure 2.1: $\delta^{15}N$ results, Phe-normalized, colored by time interval.

To assess the potential influence of microbial degradation, we created a correlation matrix of three degradation parameters (ΣV, %Gly, DI), versus the oceanographic signals we interpret in the main text ($\delta^{15}N_{Phe}$, $\delta^{15}N_{Lys}$, $\delta^{15}N_{Src}$, $\delta^{15}N_{Tr}$, TP) as well as Opal Flux and authigenic uranium (U_{auth}) from this site (DeLong et al. 2024), interpolated where the same samples were not measured. For this matrix, we use the negative value of DI and U_{auth} to align the directionality with the rest of the correlation matrix, so for all parameters higher values are associated with more degradation. Significant correlations are marked with asterisks (<0.05, *; <0.01, **).

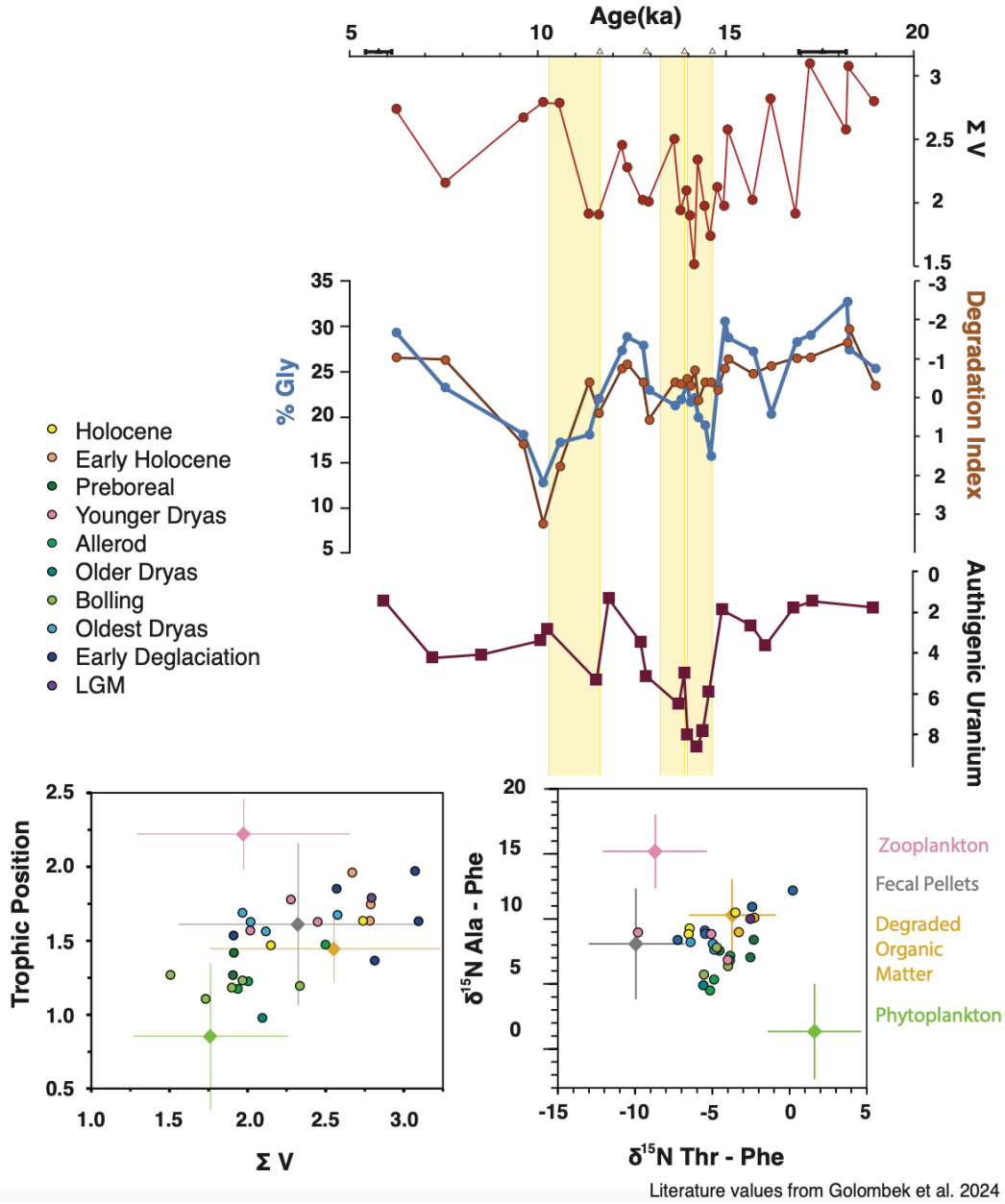

Supplemental Figure 2.2: Microbial Degradation Proxies show more degradation during the LGM and early deglaciation, and less degradation during the B-A. Yellow bars represent the presence of sedimentary laminations at this site, i.e., hypoxic to anoxic sedimentation.

We find that all degradation parameters are correlated to authigenic uranium ($-U_{auth}$), suggesting oxygenation of the sediments is an important control on

degradation (SI Figure 2). Low oxygen benthic conditions are driven by productivity (organic rain rate) and circulation; at this site, it appears that productivity is the stronger influence (DeLong et al. 2024), indicated by the high correlation with Opal Flux.

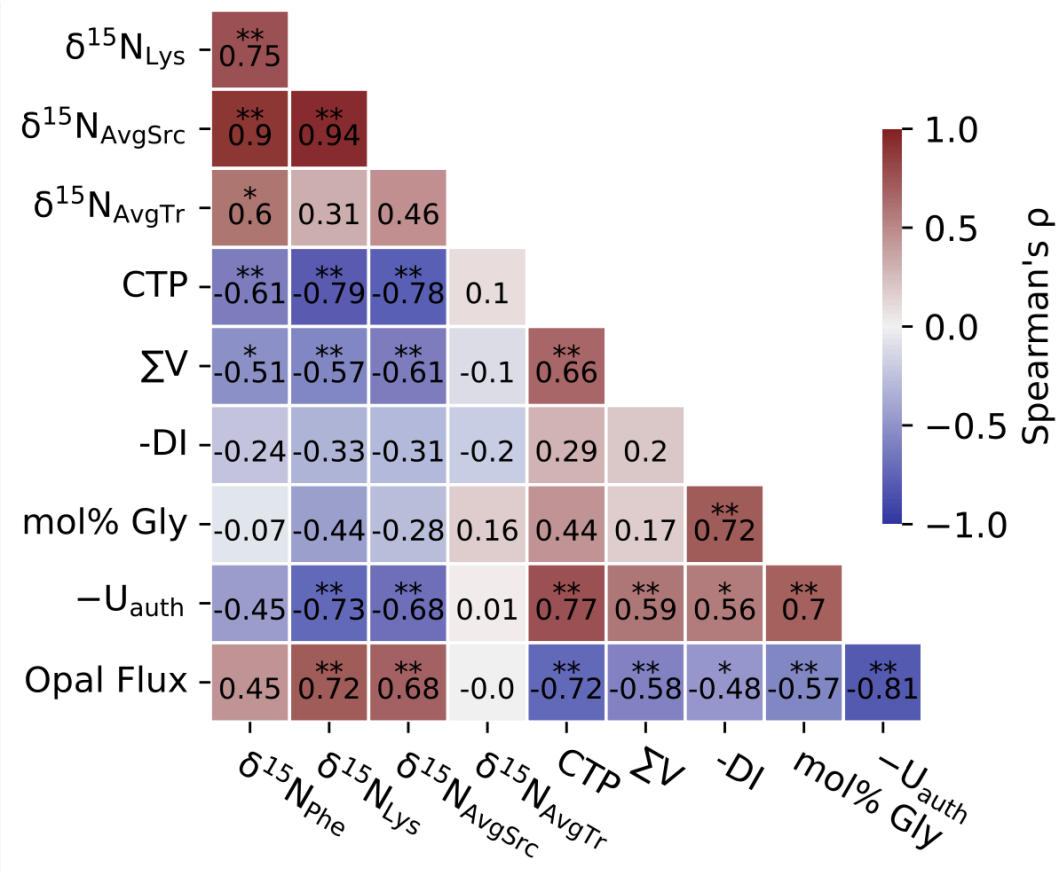

Supplemental Figure 2.3: A correlation matrix between CSI-AA data, degradation parameters, and authigenic uranium. Note the negative values of DI and U_{auth} are used to align all parameters to higher values indicating more degradation.

Thusfar, the only mechanisms of microbial degradation that have been identified either cause isotopic scatter or enrichment of $\delta^{15}N$ (McCarthy et al., 2007). One study suggested that microbial degradation in a benthic nepheloid layer, indicated by high degradation parameters, caused isotopic enrichment of $\delta^{15}N_{Src}$ (Lys

and Phe) (Golombek et al., 2024). We find the opposite, i.e., a modest correlation between depleted $\delta^{15}N_{Src}$ and SumV ($R^2 = 0.38$); this is largely driven by the fact that $\delta^{15}N_{Src}$ is high during the climate intervals with the best preservation, and $\delta^{15}N_{Src}$ is low during the intervals with the worst preservation (the early deglaciation and the Holocene). We find no correlation between $\delta^{15}N_{Src}$ and %Gly or the degradation index when all data is included. However, the degradation index returns positive values for three samples in the Early Holocene, indicating no degradation, which skews the dataset considerably. When these three samples are removed, there is a correlation ($R = 0.66$) between $\delta^{15}N_{Src}$ and DI, again with more depleted $\delta^{15}N_{Src}$ values corresponding to more degradation. We suggest these correlations are caused by the general grouping of oceanographic parameters during each climate interval rather than suggesting that degradation causes isotopic depletion. However, these processes are not well-understood and a mechanism that causes isotopic depletion of $\delta^{15}N_{Src}$ may await discovery.

The two source amino acids, Phe and Lys, correlate well with an overall slope of 1.0, suggesting both are reliable source amino acids ($m=1.0$, $R^2= 0.59$) (**SI Figure 3**). In all samples but one, $\delta^{15}N_{Lys}$ values are more depleted than $\delta^{15}N_{Phe}$, with an average offset around -1.6‰. Lys and Phe are identical within analytical error in some samples; these samples occur during the B-A and PB, and generally coincide with high opal flux and better post-depositional preservation as indicated by laminated sedimentation and high U_{auth}. The largest differences between Phe and Lys occur during the intervals higher trophic positions; this observation is the result of the

TP calculation, which inherently translates larger Lys-Phe discrepancies to higher trophic positions. The behavior of Lys strongly drives the TP calculation due to its larger range of values; however, smaller increases in the Average Trophic values also contribute to this TP shift. Thus, despite occasional differences between Phe and Lys, the differences do not appear to be driven by degradation, and an average value likely best reflects true differences in surface-derived source AA values.

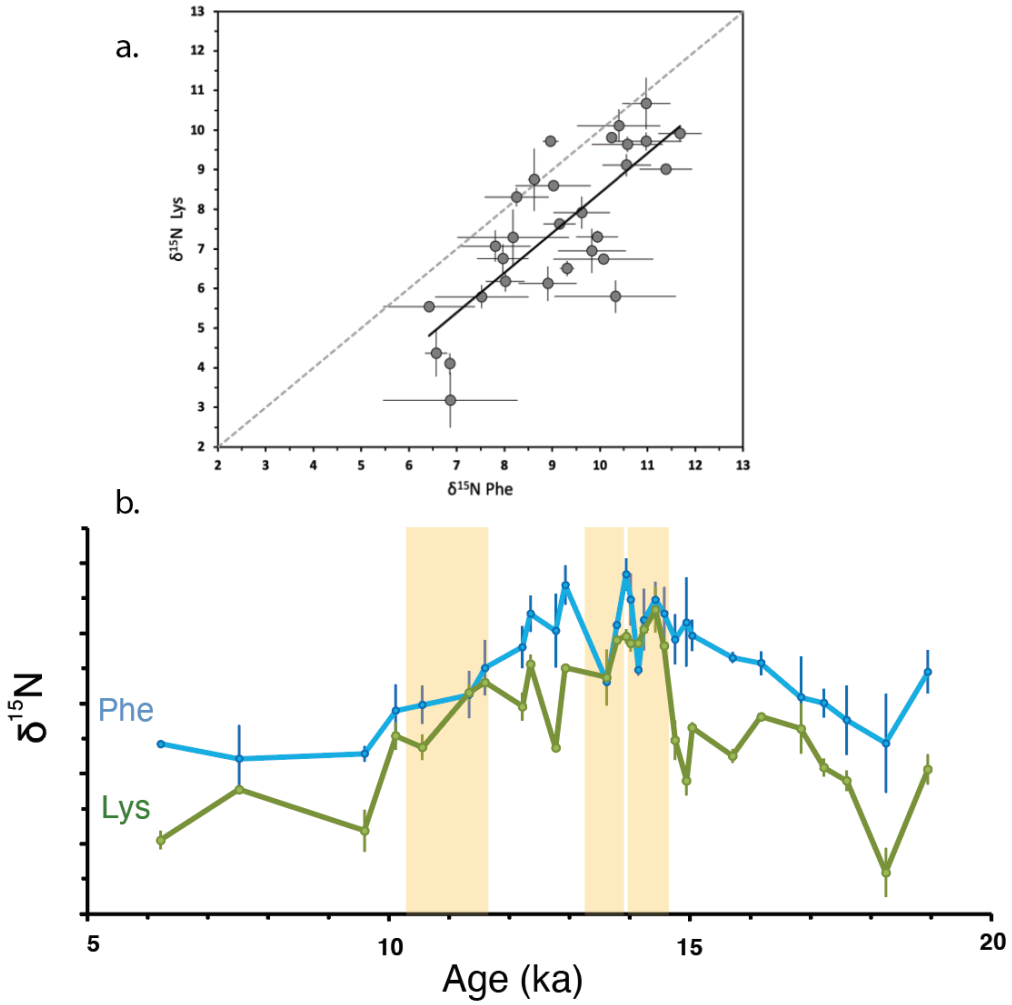

Supplemental Figure 2.4: Comparing $\delta^{15}N$ of Source AAs. (a) $\delta^{15}N_{Phe}$ vs. $\delta^{15}N_{Lys}$. (b) $\delta^{15}N_{Phe}$, blue, and $\delta^{15}N_{Lys}$, green, in time series. Yellow bars represent the presence of sedimentary laminations at this site, i.e., hypoxic to anoxic sedimentation.

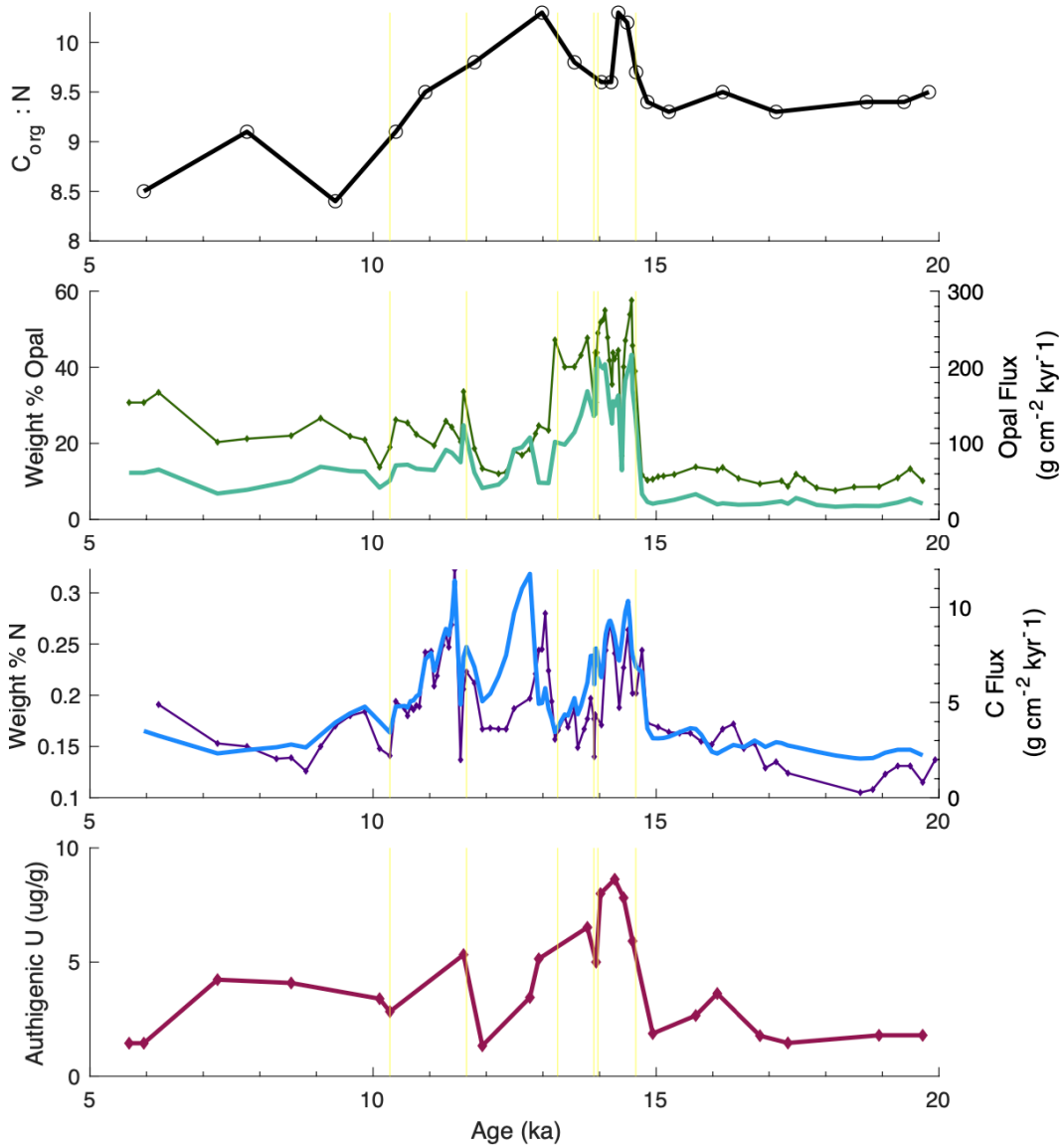

Supplemental Figure 2.5: Carbon Flux and Authigenic Uranium through time. (a) C:N ratio from Schlung et al. 2013. (b) weight% Opal and Opal Flux from DeLong et al. 2024. (c) weight% Nitrogen from DeLong et al. 2024 and calculated C Flux from the above measurements. (d) Authigenic Uranium concentration from DeLong et al. 2024.

Acknowledgements

Chapter 2, in part, is currently being prepared for submission for publication of the material with coauthors K. A. deLong, E. Pugsley, A. C. Ravelo, and M. McCarthy. The dissertation author was the primary researcher and author of this material.

Chapter 3 SOUTHERN PACIFIC SEDIMENT COLOR REFLECTS SUBANTARCTIC FRONT AND CLIMATE

1 Introduction

A number of proxies have been used to reconstruct Earth's climate over the past ~1.4 million years, including information from ice cores such as the Antarctic EPICA Dome C (EDC) (Clark et al., 2024; Lisiecki & Raymo, 2005; Zachos et al., 2001). The EDC contains reliable temperature proxies, such as deuterium (δD), and direct preservation of atmospheric gasses, such as CO_2, for approximately 800 ka; compression of ice layers with depth decreases the resolution of these proxies with age (Bereiter et al., 2015; Jouzel, 2004). The oldest ice in this record occurs at the onset of the late Pleistocene glacial cycles, characterized by highly asymmetric climate fluctuations, semi-permanent northern hemisphere glaciations, and a shift from 40-ka to 100-ka cyclicity. This late Pleistocene climate regime is preceded by cooling throughout the Mid-Pleistocene Transition (MPT) from 1250 to 750 ka (Zachos et al., 2001). This transition may have initially been instigated by tectonic and geologic processes such as global weathering changes or ice-sheet size instabilities, but these forcing factors were then amplified by changes in the Southern Ocean's carbon cycle, including circulation changes and biogeochemical feedbacks which fundamentally changed the relationship between orbital forcing, global temperatures, and atmospheric CO_2 (Berends et al., 2021; Hönisch et al., 2009; Sigman et al., 2021). The amplitude of global glaciations appears to have increased through the Pleistocene, suggesting strong positive feedbacks control much of the

response. Our knowledge of the triggers of global change and the feedbacks that amplify them is hampered by the lack of ice cores older than 800 ka, necessitating the use of disparate proxies across the MPT compared to those used to reconstruct late Pleistocene glacial cycles (Berends et al., 2021). Continuous high-resolution records of Southern Hemisphere climate change are thus crucial to improving our understanding of our current climate system.

Sediment color offers a higher resolution of information than discrete sediment sampling. While discrete sampling usually targets 1-cm^3 samples, digitally scanned photos contain ~10 pixels per millimeter of core (Wilkens et al., 2009). These digital color scans were routinely collected aboard the JOIDES Resolution beginning with Leg 198 of the Ocean Drilling Program in 2001 and continued through subsequent Integrated Ocean Drilling Program Expeditions. Sediment color, particularly its reflectance or lightness, is known to be related to calcium carbonate, opal, and organic matter content in marine sediments (e.g., Mix et al., 1995; Nederbragt et al., 2006; Wilkens et al., 2009). However, sediment color is influenced by many elements of lithology, including clay and mineral content, fossil composition, and chemical setting, meaning a unique calibration is necessary for each site (Li et al., 2022).

We use high-resolution color scans of sediments from Site U1539 to extend our knowledge of Southern Hemisphere climate behavior. Shipboard color photos, digitized in RGB (Red Green Blue) color coordinates, reveal fine-scale color changes that correspond to past climate events, including millennial- and centennial- scale

changes. A preliminary tentative age model for Site U1539 is based on glacial-interglacial alignment between the RGB Blue and the EDC δD record from East Antarctica (Lamy et al., 2021); for sediments older than the EDC, the age model is constructed by aligning RGB Blue to a global benthic $\delta^{18}O$ compilation (Lisiecki & Raymo, 2005). We selected the MIS 7/8 transition and 17/18 transition for high-resolution (0.5-cm) sediment content analysis to calibrate the RGB color information to sediment lithology. Our analysis suggests U1539 sediment color can be used to quickly predict the position of the SAF and its associated wind belts from ~1.4 Ma to the present. Correlating the marine processes at this site to the EDC record creates a new record of Southern Hemisphere climate at a higher resolution and a longer timescale than was previously known.

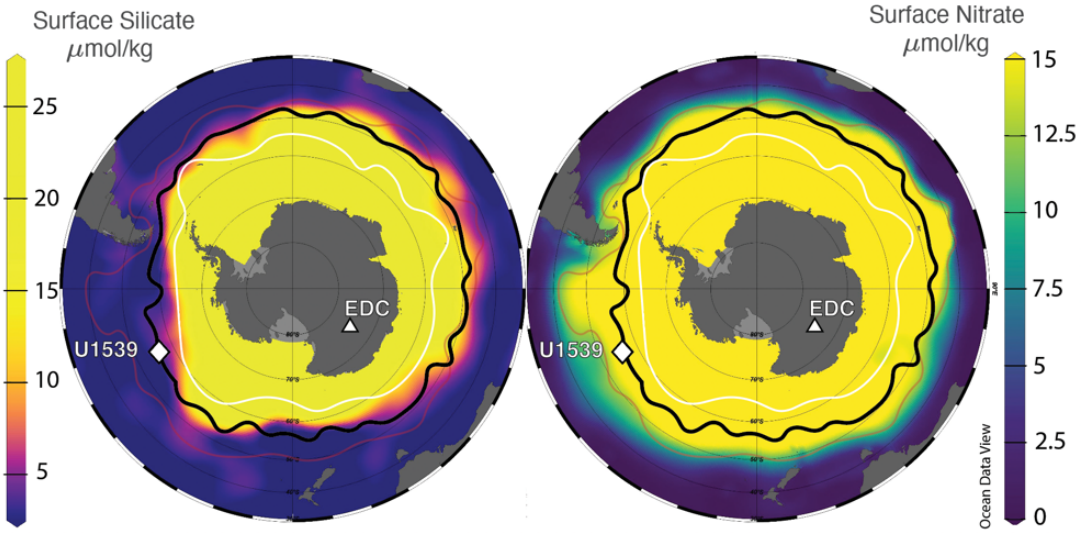

Figure 3.1: Maps of surface silicate and surface nitrate and location of Site U1539 and EPICA Dome C (EDC). The white line indicates the approximate location of the polar front. The bold black line denotes the approximate location of the Subantarctic Front (SAF). The faint red line indicates the extent of high-nitrate conditions and the Subtropical Front (STF). The Subantarctic Zone (SAZ) and Great Calcite Belt (GCB) lie between the black and red lines.

2 Background

Site U1539 (56°09.06′S, 115°08.05′W, 4110 m) is located directly beneath the modern SAF (located at ~56-58°S at this longitude), an atmospheric and oceanic boundary that separates polar waters dominated by opal export from subantarctic waters dominated by calcite export (Balch et al., 2016). South of the SAF, polar front zone waters (PFZ) have abundant surface nutrients, both Si and N; north of the SAF is the Subantarctic Zone (SAZ) and the "Great Calcite Belt" (GCB, approximately 40-60° S), replete with N but depleted in Si (Figure 1) (Sarmiento et al., 2004). The location of the SAF is set by the location of the southwesterly winds (SWWs) which respond to atmospheric temperature and pressure in the Southern Hemisphere; thus, the location of the SAF through geologic time represents shifts in hemispheric temperature gradients. The SAZ is also where Subantarctic Mode Water is formed; therefore, nutrient dynamics in this region can export different pre-formed nutrient contents to lower latitudes, an avenue that connects Southern Ocean behavior to global subtropical gyres (Sarmiento et al., 2004). The steep ocean temperature gradients of the SAF perpetuate gradients in nutrient content, productivity, and carbon sequestration, making the phytoplankton community at this site uniquely sensitive to frontal movements.

3 Methods

Sediment RGB data presented in this work was collected on Expedition 383 (Lamy et al., 2021). Discrete sediment samples were collected at a 0.5-cm resolution from off-splice sections of the cores U1539A-6H-1-W from 61.75 cm to 146.25 cm

and U1539A-6H-2-W from 0.25 to 12.25 cm, and from U1539D-11H-1-W from 34.75 to 135.25 cm. These will be referred to as the MIS 7/8 transition (43.215 to 44.185 CSF-A) and 17/18 transition (114.35 to 115.35 CSF-A). Subsampled RGB values were extracted from the shipboard digital core photos for the sampled sections; the full-record data shown is for the on-splice continuous dataset. Samples were freeze-dried and crushed by mortar and pestle. Weight percent carbonate values were measured on 15 - 60 mg of sediment using a UIC Carbon Coulometer Analyzer. The average difference between 19 sample replicates was 0.53 wt% $CaCO_3$. Two in-house standards had standard deviations of 1.00 wt% $CaCO_3$ (high density standard) and 2.33 wt% $CaCO_3$ (low density standard) throughout these runs. Bulk $\delta^{15}N$ and weight percent nitrogen were measured on a CEI NC2500 elemental analyzer coupled to a Thermo Scientific Delta-plus XP isotope ratio mass spectrometer, using tin pellets of 25-35 mg of sediment mixed with an equal mass of chromium oxide to aid combustion. The standard Acetanilide had a standard deviation of 0.38‰ $\delta^{15}N$ and 0.50% wt% N for these runs.

4 Results & Discussion

All three RGB colors strongly co-vary, indicating RGB values (measured on a 0-255 scale) are dominated by the lightness component (the degree of white versus black) rather than the hue (Figure 2). RGB can be converted to the *L*a*b** color scale to isolate the "lightness" component, *L** (shown in Figure 2). On the *L*a*b** color scale, *L** ranges from black = 0 to white = 100; positive *b** values are yellow hues

and negative b^* values are blue hues, and positive a^* values are red hues and negative a^* values are green hues.

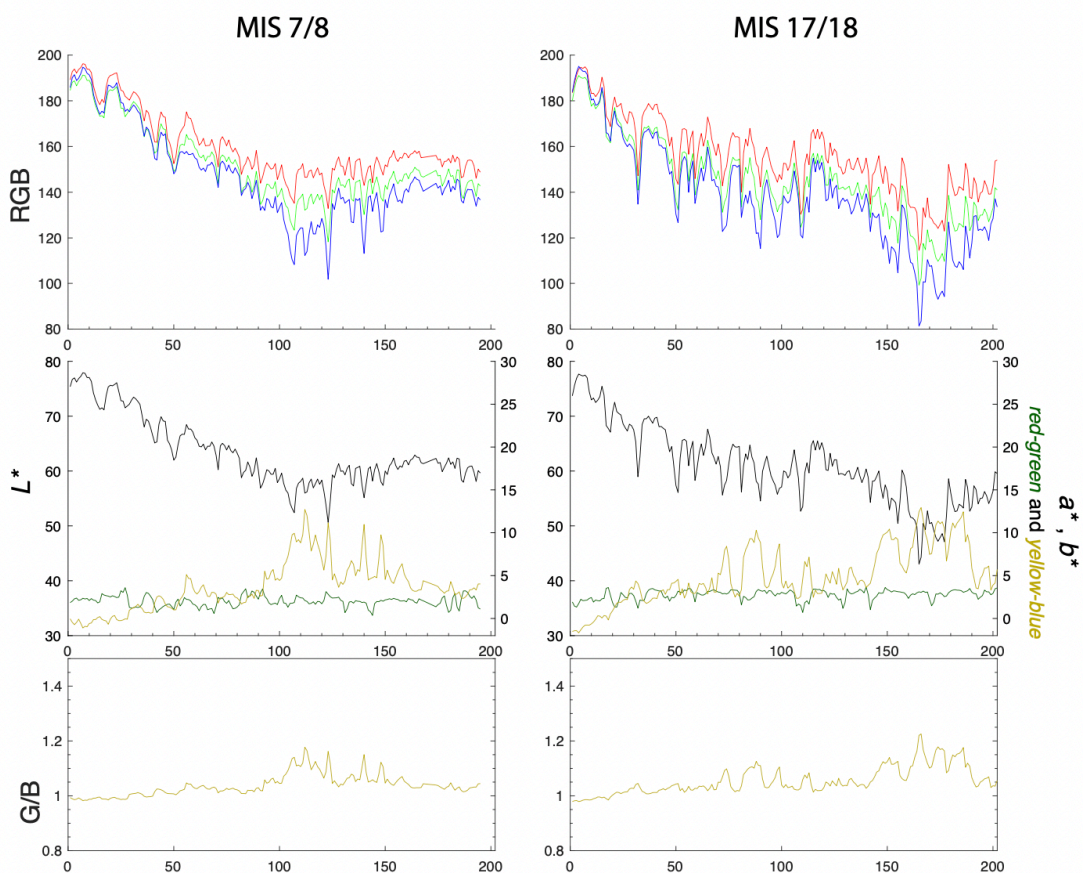

Figure 3.2: Subsampled RGB color values (0-255 scale) vs. $L^*a^*b^*$ values (0-100 scale) for the selected sections of the core representing MIS 7/8 and MIS 17/18. The x-axis here is number of data points.

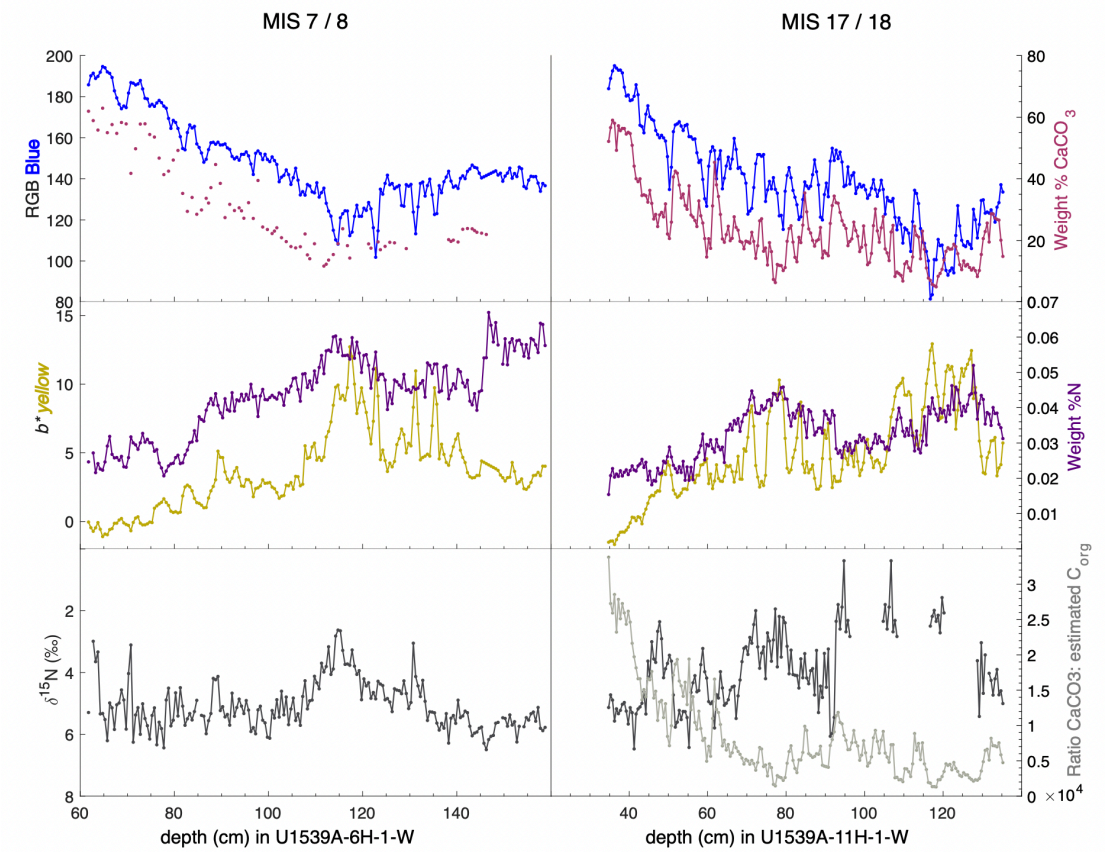

Figure 3.3: Sediment composition results for MIS 7/8 (left panels) and MIS 17/18 (right panels). Panels a-b, RGB Blue and weight percent calcium carbonate (%$CaCO_3$); panels c-d, *b** (yellow) and weight percent nitrogen (% N); panels e-f, bulk sediment $\delta^{15}N$ and the ratio between $CaCO_3$:C_{org} (only shown for MIS 17/18 due to the higher available resolution.

High resolution sampling of the MIS 17/18 transition finds the RGB color 'blue' (B) is positively correlated with wt% $CaCO_3$ (r^2=0.70) (Figure 3 and Figure 4); much of this correlation is due to the lightness (*L**) component (Tables 1 and 2). Conversely, wt% N, a measure of organic matter content, is negatively correlated with B and L* (r^2=-0.52 for B and r^2=-0.48 for L*, Tables 1 and 2); this is to be expected if the organic matter present is primarily "dark" in color, as is typical in marine sediments (Nederbragt et al., 2006). In our record, wt% N is also positively correlated with *b**, the blue-yellow color axis, which is mostly positive (yellow in

hue) in our record (r^2=0.51, Figure 3). Therefore, the color B appears to match the δD record best because its wavelengths contain the brightest changes due to the presence/absence of white coccoliths, and because some component of B is also related to changes in the blueness vs. yellowness of the sediment (*b**), which is related to the organic matter present.

A study of sediments from the Chilean margin suggested the ratio between RGB Green and RGB Blue (G/B) could be used as a proxy for biogenic opal, a measure of diatom productivity, although the relationship was site-specific; their G/B values were also related to the percent organic carbon present ($\%C_{org}$) (Li et al., 2022). The G/B calculation cancels out any co-varying lightness component, as well as canceling out the blue dimension of green, creating a value that is primarily yellow and is logarithmically related to *b**. Although that study was in a neritic setting, we likewise suggest yellow-hued marine sediments are primarily the result of diatom-sourced organic matter while bluer sediments (negative *b**) are related to a higher relative percent clay component (Figure 5, Li et al., 2022). There is very little green (negative values on the *a** color axis) present in our record (Figure 1). Negative *a** values in river sediments have been shown to be correlated to chlorophyll content, which is green in color; while positive *b** values (yellow) were correlated with the degradation of the chlorophyll-rich organic matter (Sanmartín et al., 2011). Chlorophyll compounds are unlikely to persist in deep ocean sediments; they break down into chlorins, which continue to relate to overlying primary productivity (Raja & Rosell-Melé, 2022) and are correlated to positive *b** (yellow) colors in some

marine sediments (e.g., Gorbarenko et al., 2019). At our site, the positive correlation between *b** (yellow) and weight% N may indicate the presence of chlorins, carotenoids (e.g., betacarotene, fucoxanthin, alloxanthin), or other organic compounds. The *a** record at U1539 is entirely positive, constituting red hues, and varies little; the small variability present shows a weak but possibly significant correlation to the other sediment content records (Tables 1 and 2), which could indicate unknown organic components, or inorganic components such as clays or mineral oxides (e.g., Kobayashi et al., 2016; Wei et al., 2014).

We create a simple logistic correlation between B and wt% $CaCO_3$ from MIS 17/18; overlying the MIS 7/8 data suggests it accurately captures the relationship (Figure 4). Although the measured data primarily display an exponential relationship, constraining the curve with a single data point at the highest possible of each value (255 Blue, as it would be for pure white; and 100% calcium carbonate) creates a logistic curve which has a better curve fit (adjusted r^2 value 0.81 vs. 0.77, Table 3). We then applied this correlation to the entire U1539 color record, creating a continuous, high-resolution record of southern hemisphere change (Figure 6).

We suggest sediment color changes at U1539 are primarily caused by shifts in the phytoplankton community as the SAF shifts north or south of the site, changing the ratio between coccolithophores, which export white coccoliths, and diatoms, which more efficiently export organic matter. At these latitudes, seasonal light availability, temperature and grazing pressure may all exert controls on total production, but iron (Fe) is likely to be the limiting nutrient for haptophytes if

nutrient limitation is reached (Balch et al., 2016). For diatoms, Fe limitation occurs south of the SAF while Si limitation occurs north of the SAF, and Si-Fe-colimitation may occur where these pressures overlap (Brzezinski et al., 2003; Nissen et al., 2018; Sarmiento et al., 2004; Smith et al., 2017). North of the SAF, the GCB phytoplankton community is numerically dominated by summer blooms of the calcifying haptophyte (coccolithophore) *Emiliania huxleyi* (Smith et al., 2017). The next most abundant is the nanoplankton *Fragilariopsis pseudonana*, a cosmopolitan cold-adapted pennate diatom, which briefly blooms in spring until Si-limitation, or Fe-Si-colimitation, is reached; *E. huxleyi* can then dominate in high-nutrient (N and P) but low-silicate waters throughout the summer (Smith et al., 2017). *F. pseudonana* frustules are unlikely to preserve in sediments due to its small size and light silicification (Cefarelli et al., 2010), but some of its organic matter may persist in the sediment record. A shift in seasonal nutrient supply could thus cause a relative shift between *E. huxleyi* and *F. pseudonana* export, explaining small variations in the $CaCO_3$:C_{org} ratio. Figure 3 shows an estimate of the $CaCO_3$:C_{org} ratio, where C_{org} is estimated as 10 times the nitrogen component (Honjo et al., 2000 found a C_{org}:N_{org} ratio of 7.3 in deep sediment trap particles at a similar Pacific SAZ site; this ratio likely varied over time and thus we use only a simple order-of-magnitude estimate). Larger changes in the $CaCO_3$:C_{org} ratio may be explained by large-scale expansions or contractions of the Southern Ocean fronts. In PFZ waters, larger and more diverse diatoms dominate as long as silicic acid supply remains high, though some haptophytes and flagellates are also found. *F. pseudonana* continues to be present along with other small diatoms

(nanoplankton) (e.g., *Fragilariopsis nana*, *Thalassionema nitzschioides, Pseudo-nitzschia* species, and *Thalassiosira* species), and larger diatoms (microplankton) are found where there is higher Fe supply (Froneman et al., 1995; Smith et al., 2017). A more detailed analysis of the coccoliths and diatom frustules present could illuminate the degree to which relative changes in the $CaCO_3$:C_{org} ratio reflect northward expansion of the SAF, as well as possible responses to Fe supply.

In the Subantarctic to Antarctic Pacific, $\delta^{15}N$ generally reflects nitrogen utilization (Rafter et al., 2019), which is closely coupled to nitrate availability in the modern ocean (Sigman et al., 2000); in the past, nitrogen utilization may have also been affected by dust-driven Fe fertilization (Martínez-García et al., 2014). At our site, the glacial periods (MISs 8 and 18) are lower in wt% $CaCO_3$, coupled with higher wt% N and lower $\delta^{15}N$ (Figure 3). The correlation between higher wt% N and lower $\delta^{15}N$ suggests glacial periods were associated with lower nitrate utilization, indicating higher nitrate availability, consistent with a northward shift in the SAF, northward expansion of PFZ waters, and more diatom production compared to coccolithophore production. The converse is true for the interglacial periods (MIS 7 and 17); we estimate the warmest interglacial periods over the last 1.4 Mya are 75-90% calcium carbonate by weight (Figure 6). Furthermore, the extremely low wt% N during the interglacial periods (<0.02%) may correspond to a lack of diatom export, suggesting intense Si limitation. This indicates the site was situated directly within the GCB, suggesting a southward contraction of the Antarctic fronts during past warm interglacials. However, the correlations between wt% N and $\delta^{15}N$ to sediment

color and wt% $CaCO_3$ are weaker and less consistent between the two measured intervals (Figure 5; Tables 1 and 2), and therefore the relationships are less predictive. Samples where wt% N and $\delta^{15}N$ display opposite trends to the overall correlation leave room for Fe fertilization have also influenced this site. Bulk $\delta^{15}N$ records may be subject to preservation biases or diagenesis; fossil-bound $\delta^{15}N$ records may preserve cleaner signals and are an important avenue for future studies to verify these findings (Robinson et al., 2012; Studer et al., 2015).

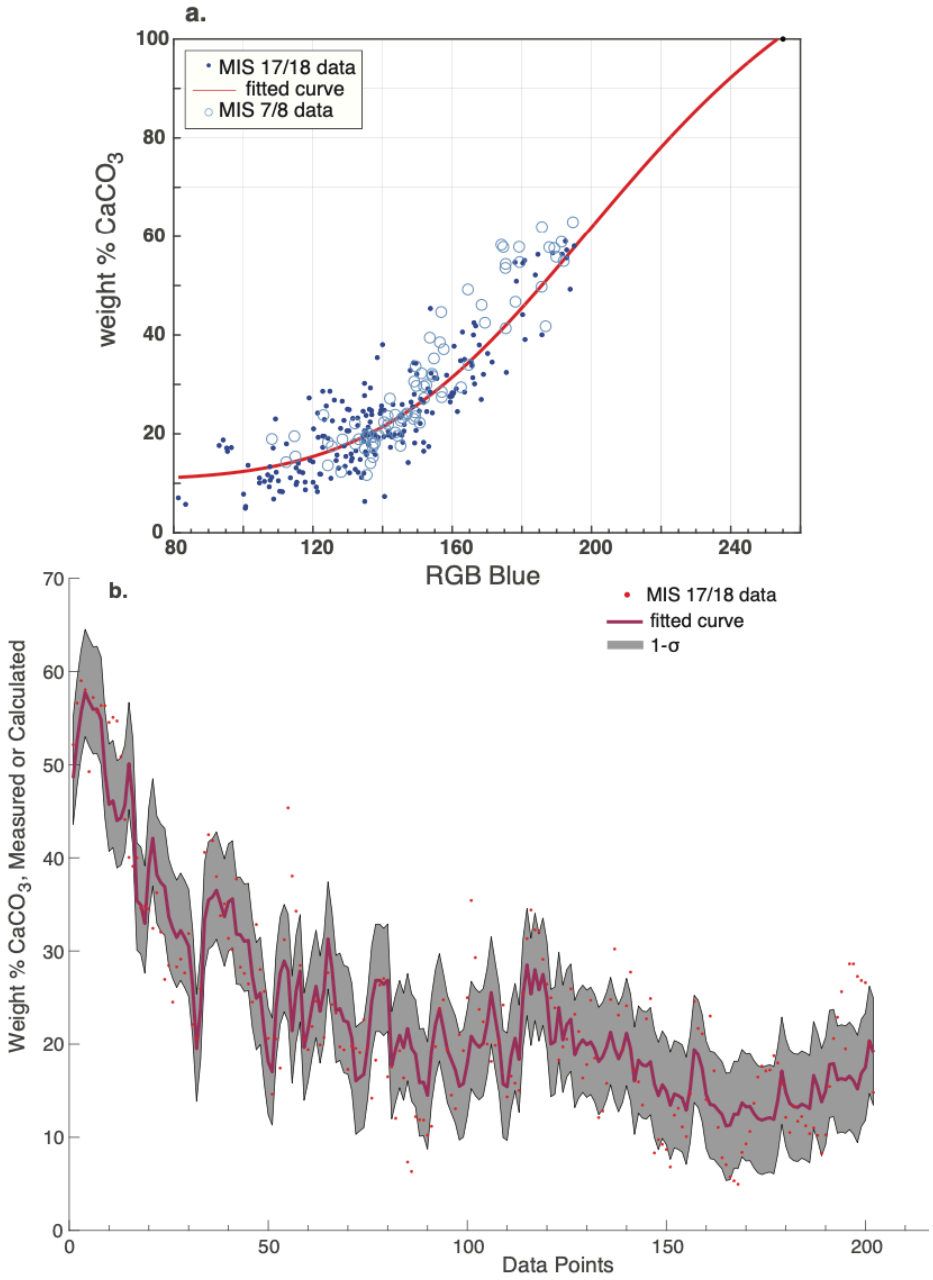

Figure 3.4: The Blue- $CaCO_3$ curve fit. (a) Constraining the Blue data with a single data point at the highest possible point of each value (255 Blue and 100% calcium carbonate) creates a logistic curve with a better fit than an exponential equation (curve fits given in Table 3). (b) The application of the Blue-derived curve fit for the MIS 17/18 interval is shown in dark pink with grey shading indicating the one standard deviation (1-σ) confidence interval; also plotted are the measured weight % $CaCO_3$ data (red dots).

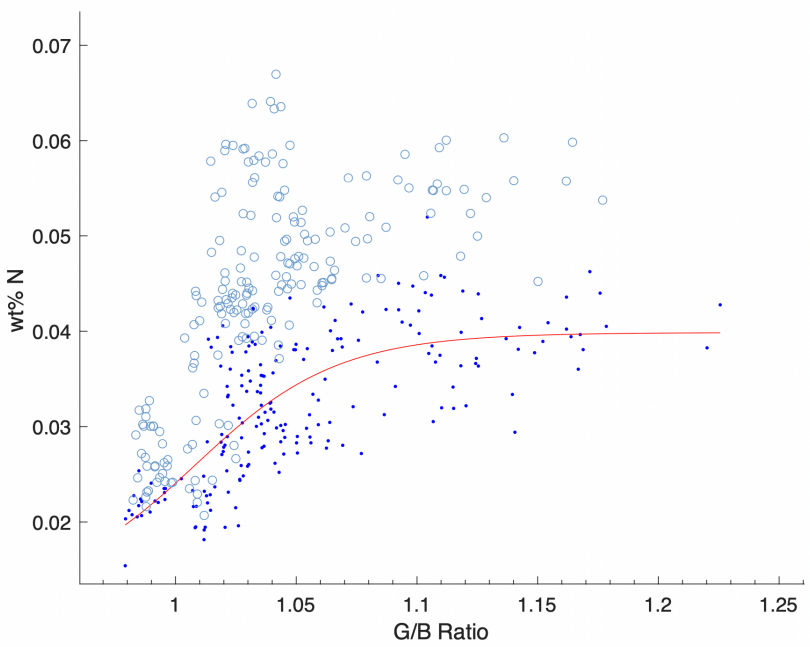

Figure 3.5: G/B Ratio and organic matter content (weight %N). Unlike the Blue-$CaCO_3$ reationship, the G/B Ratio and wt%N values do not show identical relationships in the two measured intervals, MIS 7/8 and MIS 17/18.

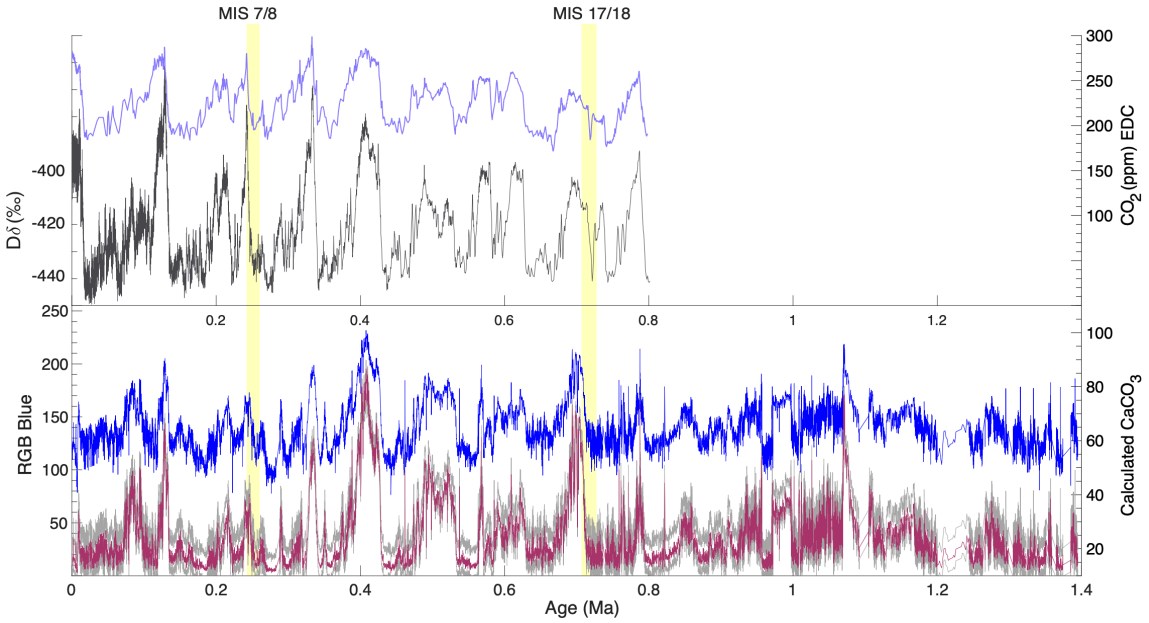

Figure 3.6: Southern Hemisphere climate records: EDC δD (Temperature) and CO_2 (ppm); U1539 Blue, and modeled weight % $CaCO_3$ (dark pink, with 1-σ confidence intervals in gray).

4 Implications & Future Work

This new record of calculated wt% $CaCO_3$ at U1539 (Figure 6) indicates significant northward movement of the SAF during glacial periods over the last ~800 ka. Expanded PFZ waters high in silicic acid, combined with higher iron supply during glacial periods, may have favored diatom production, and larger diatoms, over calcifiers over a large swath of the globe (Balch et al., 2016; Martínez-Garcia et al., 2009). Our single core location cannot determine whether the GCB merely shifted north or if it contracted in area; north-south transects of core sites across the wind fronts in each ocean basin would clarify the extent to which this site is representative of the circumpolar SAF. Future studies could also model how changes in the surface area of the GCB vs. the PFZ could be an important feedback in the global climate cycle. In the GCB, the high rates of calcification compared to organic matter synthesis inhibit oceanic CO_2 uptake from the atmosphere; in contrast, the PFZ is a net sink for atmospheric CO_2 (Balch et al., 2016; Nissen et al., 2018). Thus, alteration of the $CaCO_3$:C_{org} rain ratio across the entire subantarctic would affect both the magnitude and distribution of global carbon partitioning (Honjo et al., 2000), potentially amplifying the sequestration of CO_2 during the late Pleistocene glacial periods.

Before 800 ka, the calculated wt% $CaCO_3$ at U1539 (Figure 6) shows more subdued variability, indicating that glacial expansions in the SAF were reduced during the MPT. This suggests Southern Hemisphere temperature gradients were reduced during the MPT compared with the late Pleistocene; reduced Southern

Hemisphere temperature gradients could be driven by warmer Antarctic waters (without a change in equatorial temperatures). Warmer Antarctic waters would be expected if Antarctic ice sheets were land-based rather than marine-terminating. Thus, our record may lend support to the hypothesis that a dynamic but solely land-based East Antarctic Ice Sheet controlled Southern Hemisphere climate prior to the MPT, disconnecting global climate fluctuations from some modern marine feedback mechanisms (Raymo et al., 2006). This may be a partial explanation for why the global climate cycle was less sensitive to atmospheric CO_2 changes prior to the MPT (Hönisch et al., 2009).

In summary, sediment color changes at U1539 can be used to predict SAF changes and, by extension, Southern Hemisphere climate over long timescales, at a much higher temporal resolution and for 500 thousand years beyond current ice core records. This opens the opportunity not only for glacial-interglacial comparisons, but also suborbital millennial-scale changes to be examined. Future studies should aim to further examine the trends we describe to test hypotheses relating Southern Hemisphere climate to the global carbon cycle.

Acknowledgements

Chapter 3 contains unpublished material coauthored with A. C. Ravelo. The dissertation author was the primary author of this chapter.

Table 3.1: Pearson correlation coefficients (r values) for MIS 17/18 variables (n=202, except for $\delta^{15}N$ where n = 153). All coefficients shown are significant at Pearson's p-value < 0.005.

B	1						
*L**	0.9908	1					
*b**	-0.9004	-0.8342	1				
wt% $CaCO_3$	0.8387	0.8059	-0.8139	1			
wt% N	-0.7222	-0.6924	0.7119	-0.6907	1		
$\delta^{15}N$	0.5527	0.5135	-0.6029	0.5808	-0.3852	1	
*a**	-0.2430	-0.2117	0.2986	-0.2562	0.2809	*Not significant p > 0.1*	1
	B	*L**	*b**	wt% $CaCO_3$	wt% N	$\delta^{15}N$	*a**

Table 3.2: Spearman correlation coefficients (rho values) for MIS 17/18 variables (n=202, except for $\delta^{15}N$ where n = 153). All coefficients shown are significant at Spearman's p-value < 0.005; if not significant at this level, the range of p-values are given instead.

B							
*L**	0.9857						
*b**	-0.8996	-0.8254					
wt% $CaCO_3$	0.8008	0.7531	-0.8295				
wt% N	-0.6992	-0.6603	0.7081	-0.6771			
$\delta^{15}N$	0.5502	0.5128	-0.6061	0.5964	-0.4248		
*a**	*0.005 < p < 0.05*	*0.05 < p < 0.1*	0.2097	*0.005 < p < 0.05*	0.2518	*Not significant, p > 0.1*	
	B	*L**	*b**	wt% $CaCO_3$	wt% N	$\delta^{15}N$	*a**

Table 3.3: Comparing Blue-Calcium Carbonate equations. Equation parameters and adjusted r^2, root mean square error, and 95% confidence bounds given. The equation with the highest adjusted r^2 value is the best fit.

Equation wt% $CaCO_3$ =	a (95% confidence bounds)	b (95% confidence bounds)	c (95% confidence bounds)	d (95% confidence bounds)	Adjusted r^2	Root Mean Square Error
a*exp(b*Blue) All 11H data	1.805 (1.434, 2.177)	0.01784 (0.01656, 0.01912)	-	-	0.7741	5.65
d + [(a-d) / (1 + (Blue/c)^b)] All 11H data	8.961 (2.584, 15.34)	4.295 (0.6633, 7.927)	371.9 (-1513, 2257)	861.7 (-14910, 16640)	0.7735	5.66
d + [(a-d) / (1 + (Blue/c)^b)] All 11H data + 255,100	10.67 (7.609, 13.72)	5.645 (4.253, 7.038)	211.6 (188.1, 235.1)	132.3 (93.62, 170.9)	0.8113	5.65

REFERENCES

Abrantes, F., Gil, I., Lopes, C., & Castro, M. (2005). Quantitative diatom analyses—a faster cleaning procedure. *Deep Sea Research Part I: Oceanographic Research Papers*, *52*(1), 189–198. https://doi.org/10.1016/j.dsr.2004.05.012

Abrantes, Fatima. (1988). Diatom assemblages as upwelling indicators in surface sediments off Portugal. *Marine Geology*, *85*(1), 15–39. https://doi.org/10.1016/0025-3227(88)90082-5

Aguilar-Islas, A. M., Hurst, M. P., Buck, K. N., Sohst, B., Smith, G. J., Lohan, M. C., & Bruland, K. W. (2007). Micro- and macronutrients in the southeastern Bering Sea: Insight into iron-replete and iron-depleted regimes. *Progress in Oceanography*, *73*(2), 99–126. https://doi.org/10.1016/j.pocean.2006.12.002

Ai, X. E., Studer, A. S., Sigman, D. M., Martínez-García, A., Fripiat, F., Thöle, L. M., et al. (2020). Southern Ocean upwelling, Earth's obliquity, and glacial-interglacial atmospheric CO $_2$ change. *Science*, *370*(6522), 1348–1352. https://doi.org/10.1126/science.abd2115

Altabet, M. A., & Francois, R. (1994). Sedimentary nitrogen isotopic ratio as a recorder for surface ocean nitrate utilization. *Global Biogeochemical Cycles*, *8*(1), 103–116. https://doi.org/10.1029/93GB03396

Andersen, C., Koç, N., & Moros, M. (2004). A highly unstable Holocene climate in the subpolar North Atlantic: evidence from diatoms. *Quaternary Science Reviews*, *23*(20–22), 2155–2166. https://doi.org/10.1016/j.quascirev.2004.08.004

Anderson, R. F., Ali, S., Bradtmiller, L. I., Nielsen, S. H. H., Fleisher, M. Q., Anderson, B. E., & Burckle, L. H. (2009). Wind-Driven Upwelling in the Southern Ocean and the Deglacial Rise in Atmospheric CO $_2$. *Science*, *323*(5920), 1443–1448. https://doi.org/10.1126/science.1167441

Assmy, P., Smetacek, V., Montresor, M., Klaas, C., Henjes, J., Strass, V. H., et al. (2013). Thick-shelled, grazer-protected diatoms decouple ocean carbon and silicon cycles in the iron-limited Antarctic Circumpolar Current. *Proceedings of the National Academy of Sciences*, *110*(51), 20633–20638. https://doi.org/10.1073/pnas.1309345110

Balch, W. M., Bates, N. R., Lam, P. J., Twining, B. S., Rosengard, S. Z., Bowler, B. C., et al. (2016). Factors regulating the Great Calcite Belt in the Southern Ocean and its biogeochemical significance. *Global Biogeochemical Cycles*, *30*(8), 1124–1144. https://doi.org/10.1002/2016GB005414

Barron, J. A., Bukry, D., Dean, W. E., Addison, J. A., & Finney, B. (2009). Paleoceanography of the Gulf of Alaska during the past 15,000 years: Results from diatoms, silicoflagellates, and geochemistry. *Marine Micropaleontology*, *72*(3–4), 176–195. https://doi.org/10.1016/j.marmicro.2009.04.006

Batista, F. C., Ravelo, A. C., Crusius, J., Casso, M. A., & McCarthy, M. D. (2014). Compound specific amino acid δ 15 N in marine sediments: A new approach for studies of the marine nitrogen cycle. *Geochimica et Cosmochimica Acta*, *142*, 553–569. https://doi.org/10.1016/j.gca.2014.08.002

Bauska, T. K., Baggenstos, D., Brook, E. J., Mix, A. C., Marcott, S. A., Petrenko, V. V., et al. (2016). Carbon isotopes characterize rapid changes in atmospheric carbon

dioxide during the last deglaciation. *Proceedings of the National Academy of Sciences*, *113*(13), 3465–3470. https://doi.org/10.1073/pnas.1513868113

Bereiter, B., Eggleston, S., Schmitt, J., Nehrbass-Ahles, C., Stocker, T. F., Fischer, H., et al. (2015). Revision of the EPICA Dome C CO_2 record from 800 to 600 kyr before present. *Geophysical Research Letters*, *42*(2), 542–549. https://doi.org/10.1002/2014GL061957

Berends, C. J., Köhler, P., Lourens, L. J., & Van De Wal, R. S. W. (2021). On the Cause of the Mid-Pleistocene Transition. *Reviews of Geophysics*, *59*(2), e2020RG000727. https://doi.org/10.1029/2020RG000727

Brunelle, B. G., Sigman, D. M., Cook, M. S., Keigwin, L. D., Haug, G. H., Plessen, B., et al. (2007). Evidence from diatom-bound nitrogen isotopes for subarctic Pacific stratification during the last ice age and a link to North Pacific denitrification changes. *Paleoceanography*, *22*(1), 2005PA001205. https://doi.org/10.1029/2005PA001205

Brunelle, B. G., Sigman, D. M., Jaccard, S. L., Keigwin, L. D., Plessen, B., Schettler, G., et al. (2010). Glacial/interglacial changes in nutrient supply and stratification in the western subarctic North Pacific since the penultimate glacial maximum. *Quaternary Science Reviews*, *29*(19–20), 2579–2590. https://doi.org/10.1016/j.quascirev.2010.03.010

Brzezinski, M. A., Dickson, M.-L., Nelson, D. M., & Sambrotto, R. (2003). Ratios of Si, C and N uptake by microplankton in the Southern Ocean. *Deep Sea Research Part II: Topical Studies in Oceanography*, *50*(3–4), 619–633. https://doi.org/10.1016/S0967-0645(02)00587-8

Buesseler, K. O. (1998). The decoupling of production and particulate export in the surface ocean. *Global Biogeochemical Cycles*, *12*(2), 297–310. https://doi.org/10.1029/97GB03366

Butzin, M., Köhler, P., & Lohmann, G. (2017). Marine radiocarbon reservoir age simulations for the past 50,000 years: Marine Radiocarbon Simulations. *Geophysical Research Letters*, *44*(16), 8473–8480. https://doi.org/10.1002/2017GL074688

Caissie, B. E., Brigham-Grette, J., Lawrence, K. T., Herbert, T. D., & Cook, M. S. (2010). Last Glacial Maximum to Holocene sea surface conditions at Umnak Plateau, Bering Sea, as inferred from diatom, alkenone, and stable isotope records:

Postglacial Bering Sea Paleoclimate. *Paleoceanography*, *25*(1). https://doi.org/10.1029/2008PA001671

Carton, J. A., Chepurin, G. A., & Chen, L. (2018). SODA3: A New Ocean Climate Reanalysis. *Journal of Climate*, *31*(17), 6967–6983. https://doi.org/10.1175/JCLI-D-18-0149.1

Cefarelli, A. O., Ferrario, M. E., Almandoz, G. O., Atencio, A. G., Akselman, R., & Vernet, M. (2010). Diversity of the diatom genus Fragilariopsis in the Argentine Sea and Antarctic waters: morphology, distribution and abundance. *Polar Biology*, *33*(11), 1463–1484. https://doi.org/10.1007/s00300-010-0794-z

Chavez, F. P., Messié, M., & Pennington, J. T. (2011). Marine Primary Production in Relation to Climate Variability and Change. *Annual Review of Marine Science*, *3*(1), 227–260. https://doi.org/10.1146/annurev.marine.010908.163917

Chikaraishi, Y., Ogawa, N. O., Kashiyama, Y., Takano, Y., Suga, H., Tomitani, A., et al. (2009). Determination of aquatic food-web structure based on compound-specific nitrogen isotopic composition of amino acids. *Limnology and Oceanography: Methods*, *7*(11), 740–750. https://doi.org/10.4319/lom.2009.7.740

Chikaraishi, Y., Steffan, S. A., Ogawa, N. O., Ishikawa, N. F., Sasaki, Y., Tsuchiya, M., & Ohkouchi, N. (2014). High-resolution food webs based on nitrogen isotopic composition of amino acids. *Ecology and Evolution*, *4*(12), 2423–2449. https://doi.org/10.1002/ece3.1103

Choi, H., Yang, E. J., Kang, S.-H., Kim, D., & Shin, K.-H. (2023). Seasonal dynamics of sinking organic matter in the Pacific Arctic Ocean revealed by nitrogen isotope ratios of amino acids. *Marine Chemistry*, *253*, 104252. https://doi.org/10.1016/j.marchem.2023.104252

Clark, P. U., Shakun, J. D., Rosenthal, Y., Köhler, P., & Bartlein, P. J. (2024). Global and regional temperature change over the past 4.5 million years. *Science*, *383*(6685), 884–890. https://doi.org/10.1126/science.adi1908

Cook, M. S., Ravelo, A. C., Mix, A., Nesbitt, I. M., & Miller, N. V. (2016). Tracing subarctic Pacific water masses with benthic foraminiferal stable isotopes during the LGM and late Pleistocene. *Deep Sea Research Part II: Topical Studies in Oceanography*, *125–126*, 84–95. https://doi.org/10.1016/j.dsr2.2016.02.006

Costa, K. M., Hayes, C. T., Anderson, R. F., Pavia, F. J., Bausch, A., Deng, F., et al. (2020). ^{230} Th Normalization: New Insights on an Essential Tool for Quantifying Sedimentary Fluxes in the Modern and Quaternary Ocean. *Paleoceanography and Paleoclimatology*, *35*(2), e2019PA003820. https://doi.org/10.1029/2019PA003820

Dauwe, B., & Middelburg, J. J. (1998). Amino acids and hexosamines as indicators of organic matter degradation state inNorth Sea sediments. *Limnology and Oceanography*, *43*(5), 782–798. https://doi.org/10.4319/lo.1998.43.5.0782

Dauwe, B., Middelburg, J. J., Herman, P. M. J., & Heip, C. H. R. (1999). Linking diagenetic alteration of amino acids and bulk organic matter reactivity. *Limnology and Oceanography*, *44*(7), 1809–1814. https://doi.org/10.4319/lo.1999.44.7.1809

Davies, M. H., Mix, A. C., Stoner, J. S., Addison, J. A., Jaeger, J., Finney, B., & Wiest, J. (2011). The deglacial transition on the southeastern Alaska Margin: Meltwater input, sea level rise, marine productivity, and sedimentary anoxia: DEGLACIATION ON THE SE ALASKA MARGIN. *Paleoceanography*, *26*(2), n/a-n/a. https://doi.org/10.1029/2010PA002051

Décima, M. (2022). Zooplankton trophic structure and ecosystem productivity. *Marine Ecology Progress Series*, *692*, 23–42. https://doi.org/10.3354/meps14077

Décima, Moira, Landry, M. R., Bradley, C. J., & Fogel, M. L. (2017). Alanine δ^{15} N trophic fractionation in heterotrophic protists. *Limnology and Oceanography*, *62*(5), 2308–2322. https://doi.org/10.1002/lno.10567

DeLong, K., Blackburn, T., Caissie, B., Addison, J. A., Stroynowski, Z., Reimi Sipala, M., et al. (2024). Bolling-Allerod Productivity in the Subarctic Pacific Driven by Seasonal Upwelling. *Geophysical Research Letters*, *submited*.

Detlef, H., Sosdian, S. M., Belt, S. T., Smik, L., Lear, C. H., Kender, S., et al. (2020). Late quaternary sea-ice and sedimentary redox conditions in the eastern Bering Sea – Implications for ventilation of the mid-depth North Pacific and an Atlantic-Pacific seesaw mechanism. *Quaternary Science Reviews*, *248*, 106549. https://doi.org/10.1016/j.quascirev.2020.106549

Dickson, A., Keeling, C., Guenther, P., & Bullister, J. (2000). CO2, hydrographic and chemical data obtained during the R/V John V. Vicker cruise in the Pacific Ocean, August 4-October 21, 1992, CDIAC NDP-075.

Doherty, S. C., Maas, A. E., Steinberg, D. K., Popp, B. N., & Close, H. G. (2021). Distinguishing zooplankton fecal pellets as a component of the biological pump using compound-specific isotope analysis of amino acids. *Limnology and Oceanography*, *66*(7), 2827–2841. https://doi.org/10.1002/lno.11793

Dove, I. A., Bishop, I. W., Crosta, X., Riedinger, N., Kelly, R. P., & Robinson, R. S. (2023). *Chaetoceros resting spores record low diatom-bound nitrogen isotope values: Evidence from laboratory culture and marine sediment* (preprint). Paleobiogeoscience: Proxy use, Development & Validation. https://doi.org/10.5194/egusphere-2023-2564

Du, J., Haley, B. A., Mix, A. C., Walczak, M. H., & Praetorius, S. K. (2018). Flushing of the deep Pacific Ocean and the deglacial rise of atmospheric CO2 concentrations. *Nature Geoscience*, *11*(10), 749–755. https://doi.org/10.1038/s41561-018-0205-6

Du, J., Mix, A. C., Haley, B. A., Belanger, C. L., & Sharon. (2022). Volcanic trigger of ocean deoxygenation during Cordilleran ice sheet retreat. *Nature*, *611*(7934), 74–80. https://doi.org/10.1038/s41586-022-05267-y

Farmer, J. R., Hertzberg, J. E., Cardinal, D., Fietz, S., Hendry, K., Jaccard, S. L., et al. (2021). Assessment of C, N, and Si Isotopes as Tracers of Past Ocean Nutrient and Carbon Cycling. *Global Biogeochemical Cycles*, *35*(7). https://doi.org/10.1029/2020GB006775

Fleisher, M. Q., & Anderson, R. F. (2003). Assessing the collection efficiency of Ross Sea sediment traps using 230Th and 231Pa. *US Southern Ocean JGOFS Program (AESOPS): Part III*, *50*(3), 693–712. https://doi.org/10.1016/S0967-0645(02)00591-X

Flynn, R. F., Haraguchi, L., McQuaid, J., Burger, J. M., Mutseka Lunga, P., Stirnimann, L., et al. (2023). Nanoplankton: The dominant vector for carbon export across the Atlantic Southern Ocean in spring. *Science Advances*, *9*(48), eadi3059. https://doi.org/10.1126/sciadv.adi3059

Friedland, K. D., Record, N. R., Asch, R. G., Kristiansen, T., Saba, V. S., Drinkwater, K. F., et al. (2016). Seasonal phytoplankton blooms in the North Atlantic linked to the overwintering strategies of copepods. *Elementa: Science of the Anthropocene*, *4*, 000099. https://doi.org/10.12952/journal.elementa.000099

Froneman, P. W., McQuaid, C. D., & Perissinotto, R. (1995). Biogeographic structure of the microphytoplankton assemblages of the south Atlantic and Southern Ocean during austral summer. *Journal of Plankton Research*, *17*(9), 1791–1802. https://doi.org/10.1093/plankt/17.9.1791

Fujiwara, A., Hirawake, T., Suzuki, K., Eisner, L., Imai, I., Nishino, S., et al. (2016). Influence of timing of sea ice retreat on phytoplankton size during marginal ice zone bloom period on the Chukchi and Bering shelves. *Biogeosciences*, *13*(1), 115–131. https://doi.org/10.5194/bg-13-115-2016

Galbraith, E. D., Jaccard, S. L., Pedersen, T. F., Sigman, D. M., Haug, G. H., Cook, M., et al. (2007). Carbon dioxide release from the North Pacific abyss during the last deglaciation. *Nature*, *449*(7164), 890–893. https://doi.org/10.1038/nature06227

Gebhardt, H., Sarnthein, M., Grootes, P. M., Kiefer, T., Kuehn, H., Schmieder, F., & Röhl, U. (2008). Paleonutrient and productivity records from the subarctic North Pacific for Pleistocene glacial terminations I to V: Paleoproductivity North Pacific. *Paleoceanography*, *23*(4), n/a-n/a. https://doi.org/10.1029/2007PA001513

Georg, R. B., Reynolds, B. C., Frank, M., & Halliday, A. N. (2006). New sample preparation techniques for the determination of Si isotopic compositions using MC-ICPMS. *Chemical Geology*, *235*(1–2), 95–104. https://doi.org/10.1016/j.chemgeo.2006.06.006

Giesbrecht, K. E., Varela, D. E., De Souza, G. F., & Maden, C. (2022). Natural Variations in Dissolved Silicon Isotopes Across the Arctic Ocean From the Pacific to the Atlantic. *Global Biogeochemical Cycles*, *36*(5). https://doi.org/10.1029/2021GB007107

Golombek, N. Y., Kienast, M., Pilskaln, C. H., Algar, C., & Sherwood, O. (2024). Origin and alteration of sinking and resuspended organic matter on a benthic nepheloid layer influenced continental shelf. *Geochimica et Cosmochimica Acta*, *366*, 31–47. https://doi.org/10.1016/j.gca.2023.12.008

Gorbarenko, S. A., Malakhova, G. Y., Artemova, A. V., Bosin, A. A., Yanchenko, E. A., & Vasilenko, YuP. (2019). Millennial scale cycles in the Bering Sea during penultimate and last glacials; their similarities and differences. *Quaternary International*, *525*, 151–158. https://doi.org/10.1016/j.quaint.2019.07.016

Gouretski, V., & Koltermann, K. (2004). WOCE Global Hydrographic Climatology [Data set]. Berichte des BSH.

Gray, W. R., Rae, J. W. B., Wills, R. C. J., Shevenell, A. E., Taylor, B., Burke, A., et al. (2018). Deglacial upwelling, productivity and CO2 outgassing in the North Pacific Ocean. *Nature Geoscience*, *11*(5), 340–344. https://doi.org/10.1038/s41561-018-0108-6

Gray, W. R., Wills, R. C. J., Rae, J. W. B., Burke, A., Ivanovic, R. F., Roberts, W. H. G., et al. (2020). Wind-Driven Evolution of the North Pacific Subpolar Gyre Over the Last Deglaciation. *Geophysical Research Letters*, *47*(6), e2019GL086328. https://doi.org/10.1029/2019GL086328

Hartnett, H. E., Keil, R. G., Hedges, J. I., & Devol, A. H. (1998). Influence of oxygen exposure time on organic carbon preservation in continental margin sediments. *Nature*, *391*(6667), 572–575. https://doi.org/10.1038/35351

Hawkings, J. R., Hatton, J. E., Hendry, K. R., De Souza, G. F., Wadham, J. L., Ivanovic, R., et al. (2018). The silicon cycle impacted by past ice sheets. *Nature Communications*, *9*(1), 3210. https://doi.org/10.1038/s41467-018-05689-1

Heaton, Butzin, M., Bard, E., Bronk Ramsey, C., Hughen, K. A., Köhler, P., & Reimer, P. J. (2023). Marine radiocarbon calibration in polar regions: a simple approximate approach using marine20. *Radiocarbon*, *65*(4), 848–875. https://doi.org/10.1017/RDC.2023.42

Hönisch, B., Hemming, N. G., Archer, D., Siddall, M., & McManus, J. F. (2009). Atmospheric Carbon Dioxide Concentration Across the Mid-Pleistocene Transition. *Science*, *324*(5934), 1551–1554. https://doi.org/10.1126/science.1171477

Honjo, S., Francois, R., Manganini, S., Dymond, J., & Collier, R. (2000). Particle fluxes to the interior of the Southern Ocean in the Western Pacific sector along 170°W. *Deep Sea Research Part II: Topical Studies in Oceanography*, *47*(15–16), 3521–3548. https://doi.org/10.1016/S0967-0645(00)00077-1

Horn, M. G., Beucher, C. P., Robinson, R. S., & Brzezinski, M. A. (2011). Southern ocean nitrogen and silicon dynamics during the last deglaciation. *Earth and Planetary Science Letters*, *310*(3–4), 334–339. https://doi.org/10.1016/j.epsl.2011.08.016

Jouzel, J. (2004). 740,000-year Deuterium Record in an Ice Core from Dome C, Antarctica [Data set]. Environmental System Science Data Infrastructure for a Virtual Ecosystem; Carbon Dioxide Information Analysis Center (CDIAC), Oak

Ridge National Laboratory (ORNL), Oak Ridge, TN (United States). https://doi.org/10.3334/CDIAC/CLI.007

Keigwin, L. D. (1998). Glacial-age hydrography of the far northwest Pacific Ocean. *Paleoceanography*, *13*(4), 323–339. https://doi.org/10.1029/98PA00874

Kemp, A. E. S., Pike, J., Pearce, R. B., & Lange, C. B. (2000). The "Fall dump" — a new perspective on the role of a "shade flora" in the annual cycle of diatom production and export flux. *Deep Sea Research Part II: Topical Studies in Oceanography*, *47*(9–11), 2129–2154. https://doi.org/10.1016/S0967-0645(00)00019-9

Kender, S., Ravelo, A. C., Worne, S., Swann, G. E. A., Leng, M. J., Asahi, H., et al. (2018). Closure of the Bering Strait caused Mid-Pleistocene Transition cooling. *Nature Communications*, *9*(1), 5386. https://doi.org/10.1038/s41467-018-07828-0

Kender, S., Aturamu, A., Zalasiewicz, J., Kaminski, M. A., & Williams, M. (2019). Benthic foraminifera indicate Glacial North Pacific Intermediate Water and reduced primary productivity over Bowers Ridge, Bering Sea, since the Mid-Brunhes Transition. *Journal of Micropalaeontology*, *38*(2), 177–187. https://doi.org/10.5194/jm-38-177-2019

Kimmel, D. G., Eisner, L. B., Wilson, M. T., & Duffy-Anderson, J. T. (2018). Copepod dynamics across warm and cold periods in the eastern Bering Sea: Implications for walleye pollock (*Gadus chalcogrammus*) and the Oscillating Control Hypothesis. *Fisheries Oceanography*, *27*(2), 143–158. https://doi.org/10.1111/fog.12241

Knudson, K. P., & Ravelo, A. C. (2015). North Pacific Intermediate Water circulation enhanced by the closure of the Bering Strait. *Paleoceanography*, *30*(10), 1287–1304. https://doi.org/10.1002/2015PA002840

Kobayashi, D., Yamamoto, M., Irino, T., Nam, S.-I., Park, Y.-H., Harada, N., et al. (2016). Distribution of detrital minerals and sediment color in western Arctic Ocean and northern Bering Sea sediments: Changes in the provenance of western Arctic Ocean sediments since the last glacial period. *Polar Science*, *10*(4), 519–531. https://doi.org/10.1016/j.polar.2016.07.005

Krawczyk, D. W., Witkowski, A., Wroniecki, M., Waniek, J., Kurzydłowski, K. J., & Płociński, T. (2012). Reinterpretation of two diatom species from the West Greenland margin — Thalassiosira kushirensis and Thalassiosira antarctica var.

borealis — hydrological consequences. *Marine Micropaleontology*, *88–89*, 1–14. https://doi.org/10.1016/j.marmicro.2012.02.004

Kuehn, H., Lembke-Jene, L., Gersonde, R., Esper, O., Lamy, F., Arz, H., et al. (2014). Laminated sediments in the Bering Sea reveal atmospheric teleconnections to Greenland climate on millennial to decadal timescales during the last deglaciation. *Climate of the Past*, *10*(6), 2215–2236. https://doi.org/10.5194/cp-10-2215-2014

Lam, P. J., Robinson, L. F., Blusztajn, J., Li, C., Cook, M. S., McManus, J. F., & Keigwin, L. D. (2013). Transient stratification as the cause of the North Pacific productivity spike during deglaciation. *Nature Geoscience*, *6*(8), 622–626. https://doi.org/10.1038/ngeo1873

Lamy, F., Winckler, G., & Alvarez Zarikian, C. A. (2021). *Volume 383: Dynamics of the Pacific Antarctic Circumpolar Current (DYNAPACC)*. (Expedition 383 Scientists, Ed.) (Vol. 383). International Ocean Discovery Program. https://doi.org/10.14379/iodp.proc.383.2021

Landry, M. R., & Décima, M. R. (2017). Protistan microzooplankton and the trophic position of tuna: quantifying the trophic link between micro- and mesozooplankton in marine foodwebs. *ICES Journal of Marine Science*, *74*(7), 1885–1892. https://doi.org/10.1093/icesjms/fsx006

Li, C., Jian, Z., Jia, G., Dang, H., & Wang, J. (2019). Nitrogen Fixation Changes Regulated by Upper Water Structure in the South China Sea During the Last Two Glacial Cycles. *Global Biogeochemical Cycles*, *33*(8), 1010–1025. https://doi.org/10.1029/2019GB006262

Li, C., Clementi, V. J., Bova, S. C., Rosenthal, Y., Childress, L. B., Wright, J. D., et al. (2022). The Sediment Green-Blue Color Ratio as a Proxy for Biogenic Silica Productivity Along the Chilean Margin. *Geochemistry, Geophysics, Geosystems*, *23*(9), e2022GC010350. https://doi.org/10.1029/2022GC010350

Lisiecki, L. E., & Raymo, M. E. (2005). A Pliocene-Pleistocene stack of 57 globally distributed benthic δ^{18}O records. *Paleoceanography*, *20*(1), 2004PA001071. https://doi.org/10.1029/2004PA001071

Loveley, M. R., Marcantonio, F., Wisler, M. M., Hertzberg, J. E., Schmidt, M. W., & Lyle, M. (2017). Millennial-scale iron fertilization of the eastern equatorial Pacific

over the past 100,000 years. *Nature Geoscience*, *10*(10), 760–764. https://doi.org/10.1038/ngeo3024

Maier, E., Méheust, M., Abelmann, A., Gersonde, R., Chapligin, B., Ren, J., et al. (2015). Deglacial subarctic Pacific surface water hydrography and nutrient dynamics and links to North Atlantic climate variability and atmospheric CO_2: Subarctic Pacific Diatom δ 18O and δ 30Si. *Paleoceanography*, *30*(7), 949–968. https://doi.org/10.1002/2014PA002763

Maier, E., Zhang, X., Abelmann, A., Gersonde, R., Mulitza, S., Werner, M., et al. (2018). North Pacific freshwater events linked to changes in glacial ocean circulation. *Nature*, *559*(7713), 241–245. https://doi.org/10.1038/s41586-018-0276-y

Marchetti, A., Sherry, N. D., Kiyosawa, H., Tsuda, A., & Harrison, P. J. (2006). Phytoplankton processes during a mesoscale iron enrichment in the NE subarctic Pacific: Part I—Biomass and assemblage. *Deep Sea Research Part II: Topical Studies in Oceanography*, *53*(20–22), 2095–2113. https://doi.org/10.1016/j.dsr2.2006.05.038

Marcott, S. A., Bauska, T. K., Buizert, C., Steig, E. J., Rosen, J. L., Cuffey, K. M., et al. (2014). Centennial-scale changes in the global carbon cycle during the last deglaciation. *Nature*, *514*(7524), 616–619. https://doi.org/10.1038/nature13799

Martínez-García, A., Sigman, D. M., Ren, H., Anderson, R. F., Straub, M., Hodell, D. A., et al. (2014). Iron Fertilization of the Subantarctic Ocean During the Last Ice Age. *Science*, *343*(6177), 1347–1350. https://doi.org/10.1126/science.1246848

Martiny, A. C., Vrugt, J. A., & Lomas, M. W. (2014). Concentrations and ratios of particulate organic carbon, nitrogen, and phosphorus in the global ocean. *Scientific Data*, *1*(1), 140048. https://doi.org/10.1038/sdata.2014.48

Matsubayashi, J., Osada, Y., Tadokoro, K., Abe, Y., Yamaguchi, A., Shirai, K., et al. (2020). Tracking long-distance migration of marine fishes using compound-specific stable isotope analysis of amino acids. *Ecology Letters*, *23*(5), 881–890. https://doi.org/10.1111/ele.13496

Max, L., Lembke-Jene, L., Riethdorf, J.-R., Tiedemann, R., Nürnberg, D., Kühn, H., & Mackensen, A. (2014). Pulses of enhanced North Pacific Intermediate Water ventilation from the Okhotsk Sea and Bering Sea during the last deglaciation. *Climate of the Past*, *10*(2), 591–605. https://doi.org/10.5194/cp-10-591-2014

McCarthy, M. D., Benner, R., Lee, C., & Fogel, M. L. (2007). Amino acid nitrogen isotopic fractionation patterns as indicators of heterotrophy in plankton, particulate, and dissolved organic matter. *Geochimica et Cosmochimica Acta*, *71*(19), 4727–4744. https://doi.org/10.1016/j.gca.2007.06.061

McMahon, K. W., & McCarthy, M. D. (2016). Embracing variability in amino acid δ ^{15}N fractionation: mechanisms, implications, and applications for trophic ecology. *Ecosphere*, *7*(12), e01511. https://doi.org/10.1002/ecs2.1511

McMahon, K. W., McCarthy, M. D., Sherwood, O. A., Larsen, T., & Guilderson, T. P. (2015). Millennial-scale plankton regime shifts in the subtropical North Pacific Ocean. *Science*, *350*(6267), 1530–1533. https://doi.org/10.1126/science.aaa9942

McQuoid, M. R., & Nordberg, K. (2003). The diatom Paralia sulcata as an environmental indicator species in coastal sediments. *Estuarine, Coastal and Shelf Science*, *56*(2), 339–354. https://doi.org/10.1016/S0272-7714(02)00187-7

Meyerink, S., Ellwood, M. J., Maher, W. A., & Strzepek, R. (2017). Iron Availability Influences Silicon Isotope Fractionation in Two Southern Ocean Diatoms (Proboscia inermis and Eucampia antarctica) and a Coastal Diatom (Thalassiosira pseudonana). *Frontiers in Marine Science*, *4*, 217. https://doi.org/10.3389/fmars.2017.00217

Mino, Y., Sukigara, C., Honda, M. C., Kawakami, H., Matsumoto, K., Wakita, M., et al. (2016). Seasonal variations in the nitrogen isotopic composition of settling particles at station K2 in the western subarctic North Pacific. *Journal of Oceanography*, *72*(6), 819–836. https://doi.org/10.1007/s10872-016-0381-1

Mix, A. C., Harris, S. E., & Janecek, T. R. (1995). Estimating lithology from nonintrusive reflectance spectra: Leg 138. In *Estimating lithology from nonintrusive reflectance spectra: Leg 138* (Vol. 138). Ocean Drilling Program. https://doi.org/10.2973/odp.proc.sr.138.1995

Mix, Alan C., Pisias, N. G., Rugh, W., Wilson, J., Morey, A., & Hagelberg, T. (1995). Benthic foraminiferal stable isotope record from Site 849, 0-5 Ma: Local and global climate changes. *Proc. ODP, Scientific Results*, *138*, 371–412.

Mortlock, R. A., & Froelich, P. N. (1989). A simple method for the rapid determination of biogenic opal in pelagic marine sediments. *Deep Sea Research Part A. Oceanographic Research Papers*, *36*(9), 1415–1426. https://doi.org/10.1016/0198-0149(89)90092-7

Nederbragt, A. J., Dunbar, R. B., Osborn, A. T., Palmer, A., Thurow, J. W., & Wagner, T. (2006). Sediment colour analysis from digital images and correlation with sediment composition. *Geological Society, London, Special Publications*, *267*(1), 113–128. https://doi.org/10.1144/GSL.SP.2006.267.01.08

Nielsen, J. M., Popp, B. N., & Winder, M. (2015). Meta-analysis of amino acid stable nitrogen isotope ratios for estimating trophic position in marine organisms. *Oecologia*, *178*(3), 631–642. https://doi.org/10.1007/s00442-015-3305-7

Nissen, C., Vogt, M., Münnich, M., Gruber, N., & Haumann, F. A. (2018). Factors controlling coccolithophore biogeography in the Southern Ocean. *Biogeosciences*, *15*(22), 6997–7024. https://doi.org/10.5194/bg-15-6997-2018

Ohkouchi, N., Chikaraishi, Y., Close, H. G., Fry, B., Larsen, T., Madigan, D. J., et al. (2017). Advances in the application of amino acid nitrogen isotopic analysis in ecological and biogeochemical studies. *Organic Geochemistry*, *113*, 150–174. https://doi.org/10.1016/j.orggeochem.2017.07.009

Okazaki, Y., Timmermann, A., Menviel, L., Harada, N., Abe-Ouchi, A., Chikamoto, M. O., et al. (2010). Deepwater Formation in the North Pacific During the Last Glacial Termination. *Science*, *329*(5988), 200–204. https://doi.org/10.1126/science.1190612

Onodera, J., & Takahashi, K. (2009). Long-term diatom fluxes in response to oceanographic conditions at Stations AB and SA in the central subarctic Pacific and the Bering Sea, 1990–1998. *Deep Sea Research Part I: Oceanographic Research Papers*, *56*(2), 189–211. https://doi.org/10.1016/j.dsr.2008.08.006

Pichevin, Ganeshram, R. S., & Dumont, M. (2020). Deglacial Si remobilisation from the deep-ocean reveals biogeochemical and physical controls on glacial atmospheric CO2 levels. *Earth and Planetary Science Letters*, *543*, 116332. https://doi.org/10.1016/j.epsl.2020.116332

Pichevin, L. E., Ganeshram, R. S., Geibert, W., Thunell, R., & Hinton, R. (2014). Silica burial enhanced by iron limitation in oceanic upwelling margins. *Nature Geoscience*, *7*(7), 541–546. https://doi.org/10.1038/ngeo2181

Pike, J., Crosta, X., Maddison, E. J., Stickley, C. E., Denis, D., Barbara, L., & Renssen, H. (2009). Observations on the relationship between the Antarctic coastal diatoms Thalassiosira antarctica Comber and Porosira glacialis (Grunow) Jørgensen

and sea ice concentrations during the late Quaternary. *Marine Micropaleontology*, *73*(1–2), 14–25. https://doi.org/10.1016/j.marmicro.2009.06.005

Piquet, A. M.-T., Bolhuis, H., Meredith, M. P., & Buma, A. G. J. (2011). Shifts in coastal Antarctic marine microbial communities during and after melt water-related surface stratification: Melt water and Antarctic marine microorganisms. *FEMS Microbiology Ecology*, *76*(3), 413–427. https://doi.org/10.1111/j.1574-6941.2011.01062.x

Praetorius, S. K., Mix, A. C., Walczak, M. H., Wolhowe, M. D., Addison, J. A., & Prahl, F. G. (2015). North Pacific deglacial hypoxic events linked to abrupt ocean warming. *Nature*, *527*(7578), 362–366. https://doi.org/10.1038/nature15753

Praetorius, Summer K., Condron, A., Mix, A. C., Walczak, M. H., McKay, J. L., & Du, J. (2020). The role of Northeast Pacific meltwater events in deglacial climate change. *Science Advances*, *6*(9), eaay2915. https://doi.org/10.1126/sciadv.aay2915

von Quillfeldt, C. (2004). The Diatom Fragilariopsis Cylindrus And Its Potential As An Indicator Species For Cold Water Rather Than For Sea Ice. *VIE MILIEU*, *54*(2–3), 137–143.

Rafter, P. A., Bagnell, A., Marconi, D., & DeVries, T. (2019). Global trends in marine nitrate N isotopes from observations and a neural network-based climatology. *Biogeosciences*, *16*(13), 2617–2633. https://doi.org/10.5194/bg-16-2617-2019

Rafter, P. A., Gray, W. R., Hines, S. K. V., Burke, A., Costa, K. M., Gottschalk, J., et al. (2022). Global reorganization of deep-sea circulation and carbon storage after the last ice age. *Science Advances*, *8*(46), eabq5434. https://doi.org/10.1126/sciadv.abq5434

Ragueneau, O., Tréguer, P., Leynaert, A., Anderson, R. F., Brzezinski, M. A., DeMaster, D. J., et al. (2000). A review of the Si cycle in the modern ocean: recent progress and missing gaps in the application of biogenic opal as a paleoproductivity proxy. *Global and Planetary Change*, *26*(4), 317–365. https://doi.org/10.1016/S0921-8181(00)00052-7

Raja, M., & Rosell-Melé, A. (2022). Quantitative Link Between Sedimentary Chlorin and Sea-Surface Chlorophyll- *a*. *Journal of Geophysical Research: Biogeosciences*, *127*(5), e2021JG006514. https://doi.org/10.1029/2021JG006514

Ramirez, M. D., Besser, A. C., Newsome, S. D., & McMahon, K. W. (2021). Meta-analysis of primary producer amino acid δ^{15}N values and their influence on trophic position estimation. *Methods in Ecology and Evolution*, *12*(10), 1750–1767. https://doi.org/10.1111/2041-210X.13678

Reimer, P. J., Austin, W. E. N., Bard, E., Bayliss, A., Blackwell, P. G., Bronk Ramsey, C., et al. (2020). The IntCal20 Northern Hemisphere Radiocarbon Age Calibration Curve (0–55 cal kBP). *Radiocarbon*, *62*(4), 725–757. https://doi.org/10.1017/RDC.2020.41

Ren, H., Studer, A. S., Serno, S., Sigman, D. M., Winckler, G., Anderson, R. F., et al. (2015). Glacial-to-interglacial changes in nitrate supply and consumption in the subarctic North Pacific from microfossil-bound N isotopes at two trophic levels: δ^{15}N RECORD IN SUBARCTIC NORTH PACIFIC. *Paleoceanography*, *30*(9), 1217–1232. https://doi.org/10.1002/2014PA002765

Ren, J., Gersonde, R., Esper, O., & Sancetta, C. (2014). Diatom distributions in northern North Pacific surface sediments and their relationship to modern environmental variables. *Palaeogeography, Palaeoclimatology, Palaeoecology*, *402*, 81–103. https://doi.org/10.1016/j.palaeo.2014.03.008

Reuther, J., Shirar, S., Mason, O., Anderson, S. L., Coltrain, J. B., Freeburg, A., et al. (2021). MARINE RESERVOIR EFFECTS IN SEAL (PHOCIDAE) BONES IN THE NORTHERN BERING AND CHUKCHI SEAS, NORTHWESTERN ALASKA. *Radiocarbon*, *63*(1), 301–319. https://doi.org/10.1017/RDC.2020.127

Reynolds. (2009). Modeling the modern marine δ^{30}Si distribution: modeling the modern marine δ^{30}Si distribution. *Global Biogeochemical Cycles*, *23*(2), n/a-n/a. https://doi.org/10.1029/2008GB003266

Reynolds, Frank, & Halliday. (2006). Silicon isotope fractionation during nutrient utilization in the North Pacific. *Earth and Planetary Science Letters*, *244*(1–2), 431–443. https://doi.org/10.1016/j.epsl.2006.02.002

Robinson, R. S., Kienast, M., Luiza Albuquerque, A., Altabet, M., Contreras, S., De Pol Holz, R., et al. (2012). A review of nitrogen isotopic alteration in marine sediments. *Paleoceanography*, *27*(4), 2012PA002321. https://doi.org/10.1029/2012PA002321

Robinson, R. S., Smart, S. M., Cybulski, J. D., McMahon, K. W., Marcks, B., & Nowakowski, C. (2023). Insights from Fossil-Bound Nitrogen Isotopes in Diatoms,

Foraminifera, and Corals. *Annual Review of Marine Science*, *15*(1), 407–430. https://doi.org/10.1146/annurev-marine-032122-104001

de la Rocha, C. L., Brzezinski, M. A., & DeNiro, M. J. (1997). Fractionation of silicon isotopes by marine diatoms during biogenic silica formation. *Geochimica et Cosmochimica Acta*, *61*(23), 5051–5056. https://doi.org/10.1016/S0016-7037(97)00300-1

Roden, G. I. (1995). Aleutian Basin of the Bering Sea: Thermohaline, oxygen, nutrient, and current structure in July 1993. *Journal of Geophysical Research: Oceans*, *100*(C7), 13539–13554. https://doi.org/10.1029/95JC01291

Sancetta, C., & Robinson, S. W. (1983). Diatom Evidence on Wisconsin and Holocene Events in the Bering Sea. *Quaternary Research*, *20*(2), 232–245. https://doi.org/10.1016/0033-5894(83)90079-0

Sancetta, C., & Silvestri, S. (1986). Pliocene-Pleistocene evolution of the North Pacific Ocean-Atmosphere system, interpreted from fossil diatoms. *Paleoceanography*, *1*(2), 163–180. https://doi.org/10.1029/PA001i002p00163

Sanmartín, P., Devesa-Rey, R., Prieto, B., & Barral, M. T. (2011). Nondestructive assessment of phytopigments in riverbed sediments by the use of instrumental color measurements. *Journal of Soils and Sediments*, *11*(5), 841–851. https://doi.org/10.1007/s11368-011-0358-z

Sarmiento, J. L., Gruber, N., Brzezinski, M. A., & Dunne, J. P. (2004). High-latitude controls of thermocline nutrients and low latitude biological productivity. *Nature*, *427*(6969), 56–60. https://doi.org/10.1038/nature02127

Sarnthein, M., Gebhardt, H., Kiefer, T., Kucera, M., Cook, M., & Erlenkeuser, H. (2004). Mid Holocene origin of the sea-surface salinity low in the subarctic North Pacific. *Quaternary Science Reviews*, *23*(20–22), 2089–2099. https://doi.org/10.1016/j.quascirev.2004.08.008

Sarnthein, M., Schneider, B., & Grootes, P. M. (2013). Peak glacial 14C ventilation ages suggest major draw-down of carbon into the abyssal ocean. *Climate of the Past*, *9*(6), 2595–2614. https://doi.org/10.5194/cp-9-2595-2013

Schlung, S. A., Christina Ravelo, A., Aiello, I. W., Andreasen, D. H., Cook, M. S., Drake, M., et al. (2013). Millennial-scale climate change and intermediate water

circulation in the Bering Sea from 90 ka: A high-resolution record from IODP Site U1340: Bering Sea Climate Change Since 90 KA. *Paleoceanography*, *28*(1), 54–67. https://doi.org/10.1029/2012PA002365

Schrader, H., & Gersonde, R. (1978). Diatoms and silicoflagellates. *Utrecht Micropaleontol Bull*, *17*, 129–176.

Serno, S., Winckler, G., Anderson, R. F., Hayes, C. T., McGee, D., Machalett, B., et al. (2014). Eolian dust input to the Subarctic North Pacific. *Earth and Planetary Science Letters*, *387*, 252–263. https://doi.org/10.1016/j.epsl.2013.11.008

Serno, S., Winckler, G., Anderson, R. F., Maier, E., Ren, H., Gersonde, R., & Haug, G. H. (2015). Comparing dust flux records from the Subarctic North Pacific and Greenland: Implications for atmospheric transport to Greenland and for the application of dust as a chronostratigraphic tool. *Paleoceanography*, *30*(6), 583–600. https://doi.org/10.1002/2014PA002748

Shen, Y., Guilderson, T. P., Sherwood, O. A., Castro, C. G., Chavez, F. P., & McCarthy, M. D. (2021). Amino acid δ13C and δ15N patterns from sediment trap time series and deep-sea corals: Implications for biogeochemical and ecological reconstructions in paleoarchives. *Geochimica et Cosmochimica Acta*, *297*, 288–307. https://doi.org/10.1016/j.gca.2020.12.012

Sherwood, O. A., Guilderson, T. P., Batista, F. C., Schiff, J. T., & McCarthy, M. D. (2014). Increasing subtropical North Pacific Ocean nitrogen fixation since the Little Ice Age. *Nature*, *505*(7481), 78–81. https://doi.org/10.1038/nature12784

Sigman, Altabet, M. A., McCorkle, D. C., Francois, R., & Fischer, G. (2000). The δ^{15} N of nitrate in the Southern Ocean: Nitrogen cycling and circulation in the ocean interior. *Journal of Geophysical Research: Oceans*, *105*(C8), 19599–19614. https://doi.org/10.1029/2000JC000265

Sigman, Daniel M., Fripiat, F., Studer, A. S., Kemeny, P. C., Martínez-García, A., Hain, M. P., et al. (2021). The Southern Ocean during the ice ages: A review of the Antarctic surface isolation hypothesis, with comparison to the North Pacific. *Quaternary Science Reviews*, *254*, 106732. https://doi.org/10.1016/j.quascirev.2020.106732

Sigman, D.M., & Casciotti, K. L. (2001). Nitrogen Isotopes in the Ocean. In *Encyclopedia of Ocean Sciences* (pp. 1884–1894). Elsevier. https://doi.org/10.1006/rwos.2001.0172

Silfer, J. A., Engel, M. H., Macko, S. A., & Jumeau, E. J. (1991). Stable carbon isotope analysis of amino acid enantiomers by conventional isotope ratio mass spectrometry and combined gas chromatography/isotope ratio mass spectrometry. *Analytical Chemistry*, *63*(4), 370–374. https://doi.org/10.1021/ac00004a014

Smart, S. M., Fawcett, S. E., Ren, H., Schiebel, R., Tompkins, E. M., Martínez-García, A., et al. (2020). The Nitrogen Isotopic Composition of Tissue and Shell-Bound Organic Matter of Planktic Foraminifera in Southern Ocean Surface Waters. *Geochemistry, Geophysics, Geosystems*, *21*(2), e2019GC008440. https://doi.org/10.1029/2019GC008440

Smith, H. E. K., Poulton, A. J., Garley, R., Hopkins, J., Lubelczyk, L. C., Drapeau, D. T., et al. (2017). The influence of environmental variability on the biogeography of coccolithophores and diatoms in the Great Calcite Belt. *Biogeosciences*, *14*(21), 4905–4925. https://doi.org/10.5194/bg-14-4905-2017

Stroynowski, Z., Ravelo, A. C., & Andreasen, D. (2015). A Pliocene to recent history of the Bering Sea at Site U1340A, IODP Expedition 323: Bering Sea History at IODP Site U1340A. *Paleoceanography*, *30*(12), 1641–1656. https://doi.org/10.1002/2015PA002866

Stroynowski, Z., Abrantes, F., & Bruno, E. (2017). The response of the Bering Sea Gateway during the Mid-Pleistocene Transition. *Palaeogeography, Palaeoclimatology, Palaeoecology*, *485*, 974–985. https://doi.org/10.1016/j.palaeo.2017.08.023

Studer, A. S., Ellis, K. K., Oleynik, S., Sigman, D. M., & Haug, G. H. (2013). Size-specific opal-bound nitrogen isotope measurements in North Pacific sediments. *Geochimica et Cosmochimica Acta*, *120*, 179–194. https://doi.org/10.1016/j.gca.2013.06.041

Studer, A. S., Sigman, D. M., Martínez-García, A., Benz, V., Winckler, G., Kuhn, G., et al. (2015). Antarctic Zone nutrient conditions during the last two glacial cycles. *Paleoceanography*, *30*(7), 845–862. https://doi.org/10.1002/2014PA002745

Stuiver, M., & Reimer, P. J. (1993). Extended ^{14}C Data Base and Revised CALIB 3.0 ^{14}C Age Calibration Program. *Radiocarbon*, *35*(1), 215–230. https://doi.org/10.1017/S0033822200013904

Sverdrup, H. U. (1953). On Conditions for the Vernal Blooming of Phytoplankton. *ICES Journal of Marine Science*, *18*(3), 287–295. https://doi.org/10.1093/icesjms/18.3.287

Takahashi, T., Sutherland, S. C., Wanninkhof, R., Sweeney, C., Feely, R. A., Chipman, D. W., et al. (2009). Climatological mean and decadal change in surface ocean pCO2, and net sea–air CO2 flux over the global oceans. *Deep Sea Research Part II: Topical Studies in Oceanography*, *56*(8–10), 554–577. https://doi.org/10.1016/j.dsr2.2008.12.009

Toggweiler, J. R. (2009). Shifting Westerlies. *Science*, *323*(5920), 1434–1435. https://doi.org/10.1126/science.1169823

Tréguer, P., Bowler, C., Moriceau, B., Dutkiewicz, S., Gehlen, M., Aumont, O., et al. (2018). Influence of diatom diversity on the ocean biological carbon pump. *Nature Geoscience*, *11*(1), 27–37. https://doi.org/10.1038/s41561-017-0028-x

Walczak, M. H., Mix, A. C., Cowan, E. A., Fallon, S., Fifield, L. K., Alder, J. R., et al. (2020). Phasing of millennial-scale climate variability in the Pacific and Atlantic Oceans. *Science*, *370*(6517), 716–720. https://doi.org/10.1126/science.aba7096

Wei, J. H., Finkelstein, D. B., Brigham-Grette, J., Castañeda, I. S., & Nowaczyk, N. (2014). Sediment colour reflectance spectroscopy as a proxy for wet/dry cycles at Lake El'gygytgyn, Far East Russia, during Marine Isotope Stages 8 to 12. *Sedimentology*, *61*(6), 1793–1811. https://doi.org/10.1111/sed.12116

Wilkens, R. H., Niklis, N., & Frazer, M. (2009). Data report: digital core images as data: an example from IODP Expedition 303. In *Proceedings of the IODP, 303/306*. Integrated Ocean Drilling Program. https://doi.org/10.2204/iodp.proc.303306.2006

Wojtal, P. K., Doherty, S. C., Shea, C. H., Popp, B. N., Benitez-Nelson, C. R., Buesseler, K. O., et al. (2023). Deconvolving mechanisms of particle flux attenuation using nitrogen isotope analyses of amino acids. *Limnology and Oceanography*, *68*(9), 1965–1981. https://doi.org/10.1002/lno.12398

Worne, S., Stroynowski, Z., Kender, S., & Swann, G. E. A. (2021). Sea-ice response to climate change in the Bering Sea during the Mid-Pleistocene Transition. *Quaternary Science Reviews*, *259*, 106918. https://doi.org/10.1016/j.quascirev.2021.106918

Yoshida, K., Nakamura, S., Nishioka, J., Hooker, S. B., & Suzuki, K. (2020). Community Composition and Photosynthetic Physiology of Phytoplankton in the Western Subarctic Pacific Near the Kuril Islands With Special Reference to Iron Availability. *Journal of Geophysical Research: Biogeosciences*, *125*(3), e2019JG005525. https://doi.org/10.1029/2019JG005525

Yoshida, K., Nishioka, J., Yasuda, I., & Suzuki, K. (2023). Different responses of phytoplankton to Fe manipulation in Fe-limited waters with contrasting surface mixed layer depths in the western subarctic Pacific. *Journal of Oceanography*, *79*(5), 483–497. https://doi.org/10.1007/s10872-023-00692-7

Yoshikawa, C., Makabe, A., Matsui, Y., Nunoura, T., & Ohkouchi, N. (2018). Nitrate Isotope Distribution in the Subarctic and Subtropical North Pacific. *Geochemistry, Geophysics, Geosystems*, *19*(7), 2212–2224. https://doi.org/10.1029/2018GC007528

Yoshikawa, C., Ogawa, N. O., Chikaraishi, Y., Makabe, A., Matsui, Y., Sasai, Y., et al. (2022). Nitrogen Isotopes of Sinking Particles Reveal the Seasonal Transition of the Nitrogen Source for Phytoplankton. *Geophysical Research Letters*, *49*(17), e2022GL098670. https://doi.org/10.1029/2022GL098670

You, Y. (2003). The pathway and circulation of North Pacific Intermediate Water: The pathway and circulation of NPIW. *Geophysical Research Letters*, *30*(24). https://doi.org/10.1029/2003GL018561

Yu, J., Broecker, W. S., Elderfield, H., Jin, Z., McManus, J., & Zhang, F. (2010). Loss of Carbon from the Deep Sea Since the Last Glacial Maximum. *Science*, *330*(6007), 1084–1087. https://doi.org/10.1126/science.1193221

Zachos, J., Pagani, M., Sloan, L., Thomas, E., & Billups, K. (2001). Trends, Rhythms, and Aberrations in Global Climate 65 Ma to Present. *Science*, *292*(5517), 686–693. https://doi.org/10.1126/science.1059412

Zhu, J., Chen, M., Hu, W., Zheng, M., & Qiu, Y. (2021). Biogeochemical cycling of nutrient in the western Bering Sea as revealed by nitrogen isotopic composition of nitrate and suspended particles. *Deep Sea Research Part I: Oceanographic Research Papers*, *174*, 103551. https://doi.org/10.1016/j.dsr.2021.103551